



U.S. DEPARTMENT OF
ENERGY

PNNL-22277
PL06-136-PD05

FY08 Annual Report: Amorphous Semiconductors for Gamma Radiation Detection (ASGRAD)

B. R. Johnson
B. J. Riley
J. V. Crum
J. V. Ryan
S. K. Sundaram
J. McCloy
A. Rockett, UIUC

February 2009



Pacific Northwest
NATIONAL LABORATORY

*Proudly Operated by **Battelle** Since 1965*

DISCLAIMER

This report was prepared as an account of work sponsored by an agency of the United States Government. Neither the United States Government nor any agency thereof, nor Battelle Memorial Institute, nor any of their employees, makes **any warranty, express or implied, or assumes any legal liability or responsibility for the accuracy, completeness, or usefulness of any information, apparatus, product, or process disclosed, or represents that its use would not infringe privately owned rights.** Reference herein to any specific commercial product, process, or service by trade name, trademark, manufacturer, or otherwise does not necessarily constitute or imply its endorsement, recommendation, or favoring by the United States Government or any agency thereof, or Battelle Memorial Institute. The views and opinions of authors expressed herein do not necessarily state or reflect those of the United States Government or any agency thereof.

PACIFIC NORTHWEST NATIONAL LABORATORY

operated by

BATTELLE

for the

UNITED STATES DEPARTMENT OF ENERGY

under Contract DE-ACO5-76RL01830

This work was conducted in part at the Environmental Molecular Sciences Laboratory (EMSL), which is operated by the Office of Biological and Environmental Research of the U.S. Department of Energy (DOE) at Pacific Northwest National Laboratory (PNNL).

Printed in the United States of America

Available to DOE and DOE contractors from the
Office of Scientific and Technical Information,
P.O. Box 62, Oak Ridge, TN 37831-0062;
ph: (865) 576-8401
fax: (865) 576 5728
email: reports@adonis.osti.gov

Available to the public from the National Technical Information Service,
U.S. Department of Commerce, 5285 Port Royal Rd., Springfield, VA 22161
ph: (800) 553-6847
fax: (703) 605-6900
email: orders@nits.fedworld.gov
online ordering: <http://www.ntis.gov/ordering.htm>

FY08 Annual Report: Amorphous Semiconductors for Gamma Radiation Detection (ASGRAD)

B. R. Johnson
B. J. Riley
J. V. Crum
J. V. Ryan
S. K. Sundaram
J. McCloy
A. Rockett, UIUC

February, 2009

Work performed for the Office of Defense Nuclear Nonproliferation (NA-20)
Office of Nonproliferation Research and Development (NA-22) under
Project Number PL06-136-PD05

Prepared for the U.S. Department of Energy
under Contract DE-AC05-76RL01830

Pacific Northwest National Laboratory
Richland, Washington 99354

Summary

High Z, high resistivity, amorphous semiconductors were designed for use as solid-state detectors at near ambient temperatures; their principles of operation are analogous to single-crystal semiconducting detectors. Compared to single crystals, amorphous semiconductors have the advantages of rapid, cost-effective, bulk-fabrication; near-net-shape fabrication of complicated geometries; compositional flexibility; and greater electronic property control. The main disadvantage is reduced-charge carrier mobility. This project developed amorphous semiconductor materials for gamma detection applications that leverage material advantages while mitigating the limitations of this class of materials. This development effort focused on materials synthesis, characterization of physical properties, characterization of electrical properties, radiation detector design, as well as detector signal collection and processing.

During the third year of this project, several important milestones were accomplished. These include:

- 1) We were able to collect pulse-height spectra with an amorphous semiconductor-based radiation detector. This was done using both an alpha source and a gamma source.
- 2) We identified an anomalous conduction phenomenon in certain amorphous semiconductors. When cooled to approximately 250K, they displayed enhanced conductivity by several orders of magnitude. This increase is thought to be due to increased charge carrier mobility rather than an increase in charge carrier population. This is significant for radiation detection applications because it indicates there could be a temperature regime where amorphous semiconductors could have significantly enhanced performance.
- 3) We developed the capability to perform automated, high-precision, electronic property (conductivity, resistivity, Hall mobility) measurements of highly resistive materials as a function of temperature, source voltage, and source current.
- 4) Three refereed journal papers were published. A fourth paper has been submitted
- 5) We mentored an undergraduate student and contributed towards their educational and professional development as they assisted in making and testing specimens.
- 6) The collaborative working relationship was developed with Prof. Angus Rockett at the University of Illinois at Urbana-Champaign (UIUC). They performed key materials characterization experiments to evaluate the electrical performance of different metallization schemes.

The development of Schottky barrier contacts for the higher conductivity amorphous semiconductors was identified as one of the most significant goals to achieve in FY 2008. Initial results looked quite promising, but the results were not reproducible. Significant effort and attention was directed towards this effort by both PNNL and UIUC, but a suitable rectifying contact material and a reproducible deposition process has not been found. Additional details about the status of this task are addressed in the body of this report.

The project was scoped and budgeted to focus on materials synthesis and characterization. The materials and processing challenges associated with developing high-performance contacts on novel semiconducting materials was beyond the scope of this project. That said, the strategy was to leverage traditional semiconductor technologies as a best-effort approach. The concept was to use lower resistivity materials with better charge carrier mobility properties and operate them under reverse bias to create a low-noise, high-resistivity condition that can be switched to a low-resistivity, high conductivity condition

under exposure to radiation events, and then off again. The key to creating effective Schottky barrier contacts lies in finding a metal with a work function that is suitably matched to the semiconductor. Professor Rockett's research group at the University of IL has been using Kelvin probe force microscopy using an AFM to measure and evaluate the work function of various contact metals and amorphous Cd-Ge-As. They were able to make modest progress on this effort, and their results are presented in the appendix to this report.

Abbreviations and Acronyms

AST	Arsenic-selenium-telluride; $\text{As}_4\text{Se}_{60-x}\text{Te}_x$
BSE	Back-scattered electron
CVD	Chemical vapor deposition
CGA	Cadmium-germanium-di-arsenide; CdGe_xAs_2
EDS	Energy dispersive spectroscopy
EMSL	Environmental Molecular Sciences Laboratory
IR	Infrared
IV	Current - voltage
KPFM	Kelvin probe force microscopy
NIST	National Institute for Standards and Technology
NOMSL	Non-oxide Materials Synthesis Laboratory
PNNL	Pacific Northwest National Laboratory
PPMS	Physical property measurement system
SEM	Scanning electron microscopy
SOW	Statement of work
UHV	Ultra-high vacuum
UIUC	University of Illinois at Urbana-Champaign
UV-VIS-NIR	Ultraviolet visible near infrared
XRD	X-ray diffraction
Z	Atomic number

Contents

1.0	Introduction.....	1.1
2.0	Materials Synthesis	2.1
2.1	Synthesis Method.....	2.1
2.2	New Chemistries.....	2.2
2.3	Progress on Identifying the New Metastable Phase	2.4
2.4	Processing Summary	2.5
3.0	Electrical Property Characterization	3.7
3.1	Current-voltage curves.....	3.7
3.2	Hall mobility	3.8
4.0	Radiation Response Testing.....	4.8
4.1	DC Ionization Tests	4.9
4.2	Pulse Testing.....	4.12
4.3	Summary.....	4.14
5.0	Collaboration with the University of Illinois at Urbana-Champaign (UIUC).....	5.1
5.1	Conclusions of the materials characterization at UIUC	5.1
5.2	Schottky contacts	5.1
6.0	Outcomes and Future Direction	6.1
6.1	Major Project Outcomes	6.1
6.2	Future Direction.....	6.1
7.0	References.....	7.1
8.0	Appendix A.....	8.2

Figures

Figure 1. Top: double containment schematic; Bottom: double containment ampoule with copper.	2.2
Figure 2. Plot of density and conductivity as a function of Te concentration for $As_{40}Se_{(60-x)}Te_x$ [7,8].....	2.3
Figure 3. Microscopic analysis of metastable phases formed in Cd-Ge-As during quenching. Polarized reflected light microscopy (A) revealed two distinct crystal morphologies (polycrystals and needles) in an amorphous matrix. Examination by XRD detected $CdGeAs_2$ and a new, unidentified phase(s). Electron backscattered diffraction (B) determined the polycrystals (colored) were $CdGeAs_2$, and confirmed the matrix was amorphous, but diffraction patterns from needles were unidentifiable. Compositional differences (Z_{ave} contrast) were accentuated using SEM BSE (C), and stoichiometry was determined by quantitative EDS mapping (D, polycrystals = $CdGeAs_2$, needles = $Cd_3Ge_2As_4$). Lattice parameters, space group, and structure factor calculations for the new phase are in progress.	2.4
Figure 4. Electrical conductivity as a function of temperature for chalcogenide amorphous semiconductors. Note the greatly increased conductivity at $\sim -20^\circ C$	3.8
Figure 5. Current-voltage curve for $CdGe_{0.85}As_2$ from 0-100 V at $-40^\circ C$	4.9
Figure 6. Current vs. time for $As_{40}Se_{48}Te_{12}$ as a function of exposure to a sealed source at room temperature and a bias of 500V.	4.10
Figure 7. Variation in DC ionization current as a function of applied field.	4.11
Figure 8. Detector gain as a function of applied field for amorphous As_2Se_3 for exposure to a sealed alpha source.	4.12
Figure 9. Pulse measured by As-Se-Te detector from an ^{241}Am source. The data was collected using a digital oscilloscope with the detectr biased at 700V.	4.13
Figure 10. Pulse height spectrum from an ^{241}Am alpha source as collected by an amorphous semiconductor.....	4.13
Figure 11. A test pattern and contact arrays of Mg metal deposited on Sample ASGRAD 41c. Current - voltage measurements were made from Mg contact to Mg contact, from Mg contact to an ohmic contact (used for Hall effect) on the back side of the wafer, and from Mg contact to a probe placed directly on an exposed area of the CGA.....	5.2
Figure 12. Left, a linear scale plot and right a logarithmic plot of the current/voltage curves for sample 41c measured between two sets of Mg contacts in the light and in the dark. A large difference in conductivity is observed.	5.2

Tables

Table 2.1. Matrix of Iodine-doped Arsenic Trisulfide Compositions Synthesized and Tested. Table	2.3
Table 2.2. Summary of ampoules produced in FY08	2.5

1.0 Introduction

The guiding motivation of this project was to develop new, innovative materials to enable detection of gamma radiation. The two principal techniques used to detect and obtain energy resolution information from gamma radiation are based on either scintillators or semiconductors. This project chose to focus on the second – the direct conversion of gamma photons into an electrical signal using semiconductors. Traditional semiconductor-based detectors rely on single crystals as the active detecting medium because they have a well-ordered electronic structure that facilitates rapid charge carrier transport. However, there are significant processing problems associated with the growth of large ($\sim 1\text{cm}^3$), defect-free, single crystals from multi-component materials (e.g., Cd-Zn-Te (CZT) crystals). These challenges limit the size and availability of the crystals for applications. A significant amount of research and development is still required to improve the performance and production yield of single crystal CZT.

In light of this need, we have proposed the development of amorphous semiconductors as a potential alternative or interim solution for room-temperature gamma radiation detection. Compared to single crystals, amorphous semiconductors have the potential advantages of rapid, cost-effective, bulk-fabrication; near-net-shape fabrication of complicated geometries; compositional flexibility, and greater compositional and electronic property control. The main disadvantage of an amorphous semiconductor is reduced-charge carrier mobility due to the disordered structure. In this project, we are focusing our efforts to mitigate the technical problems with amorphous semiconductors to develop an optimized material for radiation detection.

The materials selected for this study were based on the following criteria: semiconducting, moderate-to-high atomic number, moderate band-gap, high-resistivity, and glass forming. This lead us to two families of amorphous semiconductors – the chalcogenides (compounds based on S, Se, or Te) and the chalcopyrites (a class name given to a family of component compounds that have a tetragonal unit cell) Within the chalcopyrite family of semiconductors, CdGeAs₂ is the best-known glass-former. Single crystal CdGeAs₂ has very excellent charge carrier mobility ($\sim 10^4\text{cm}^2/(\text{Vs})$ at room temperature) [1,2], and has one of the highest reported non-linear optical coefficients. It is also iso-structural with another multi-component single crystal chalcopyrite semiconductor, AgGaSe₂, which has demonstrated radiation detection capability [3]. In the amorphous form, CdGeAs₂ has a large reported compositional range (Ge = 0.2 - 1.3) and also has reported substitutional ability (e.g. replace Ge with other elements such as Si or Sb) [4-6]. These properties make it a very good candidate for investigating the potential application of amorphous semiconductors for radiation detection applications. Unfortunately, its band gap ($\sim 0.9 - 1.0$ eV) and its resistivity ($10^7 - 10^9$ Ohm-cm) are somewhat lower than optimal. However, because it is a known multi-component, glass-forming semiconductor, it lies within the targeted region of the periodic table, and it has very large compositional flexibility, it is a good material to demonstrate compositional control of gamma radiation detection properties. Additionally, the fact that it is iso-structural with other higher Z chalcopyrites such as AgGaSe₂ (that has been reported to respond in crystal form to gamma radiation) may allow us to blend these compounds together in an amorphous state to create an ideal amorphous gamma radiation detection material.

The chalcogenide family of amorphous semiconductors from the As-Se-Te system was chosen not only because of their electrical properties, but because they are excellent glass formers, they are exceptionally resistive ($\geq 10^{12}$ ohm•cm), and they are sensitive to optical photons (photo-induced property changes). It was suspected that their photosensitivity might be an indication of being sensitive to ionizing radiation as well (gamma photons).

The major successes in FY06 were processing based: we developed the ability to synthesize crack-free, amorphous ingots of Cd-Ge-As glass with very high purity and homogeneity. Two different process methods were developed, and various physical, chemical, and electrical analyses were completed to establish the homogeneity and chemical purity of the material. Initial testing and evaluation these material established they had suitable properties for radiation detection applications.

In FY07, we were able to move beyond transforming raw elements to new materials, into actually making and testing devices made from these new materials. The major successes in FY07 are as follows:

- We demonstrated the ability to measure a DC ionization response to alpha radiation in three different amorphous semiconductors: $\text{CdGe}_{0.85}\text{As}_2$, $\text{As}_{40}\text{Se}_{60}$, and $\text{As}_{40}\text{Se}_{48}\text{Te}_{12}$.
- We demonstrated the ability to control and reduce the density of defect states in the band gap of Cd-Ge-As glasses by controlling composition as well as processing conditions.
- We demonstrated the ability to reduce the density of defect states by doping the material with hydrogen, a commonly used approach when working with amorphous silicon.
- We were able to build Schottky barrier contacts on Cd-Ge-As glass and demonstrated diode performance and enhanced photosensitivity. The barrier contacts reduced the leakage currents by approximately 5 orders of magnitude. This enabled the ability to measure a photoconductive response in the material: the illuminated conductivity was about 2 orders of magnitude greater than in the dark.

In FY08, our major accomplishments included the following:

- We continued to refine and improve our materials processing technologies for synthesizing bulk amorphous semiconductors using the double-containment quench method.
- We conducted high precision electrical characterization experiments on our specimens and discovered an anomalous temperature region of increased conductivity for As-Se, and As-Se-Te amorphous semiconductors.
- We designed and built more sophisticated test devices and fabricated more sophisticated test specimens to include such features as guard rings and pixilated contacts for enhanced radiation detector performance. We performed basic electrical characterization of our test specimens to determine their performance parameters (bias voltage, time constant, etc.) for radiation testing, and then perform radiation tests on them such as DC ionization tests.
- We continued to collaborate with UIUC to develop Schottky barrier contacts and build FET structures on Cd-Ge-As. Initial electrical testing results were promising; the devices showed a high degree of photosensitivity, but the results were not reproducible with other specimens.
- We conducted successful pulse testing with As-Se, and As-Se-Te amorphous specimens and were able to collect individual pulses as well as pulse height spectrum that showed response to irradiation with alpha sources.

The results from this project have increased our understanding of chalcopyrite and chalcogenide amorphous semiconductors. We have shared this increased knowledge with the technical community via published journal articles. This information will contribute to the eventual design of suitable devices and identify suitable applications for using amorphous semiconductor-based radiation detectors.

2.0 Materials Synthesis

One of the key milestones of success in the project was the ability to form bulk, crack-free amorphous semiconductor ingots. Crystallization is a natural process that occurs as a liquid cools to a solid, and the formation of crystals is driven by changes in free energy of the system: the crystallized state has lower free energy than a disordered solid state. Since changes in free energy favor crystallization, special processing techniques are required to solidify a liquid into a disordered solid state without crystals. In essence, the goal is to rapidly cool the liquid to “freeze” in the disordered liquid structure before the system is able to order and form crystals. We were able to develop a couple of different methods to accomplish this, depending on the crystallization kinetics of the specific material being processed.

2.1 Synthesis Method

One approach to fabricating amorphous, crack-free ampoules was to use a double-containment system. Two concentric, evacuated ampoules are used; the inner is filled with the elements of choice, and the gap between the inner and outer is filled with a high thermal conductivity material (e.g. Cu). The approach has several advantages. The increased thermal mass of the system reduces the heat loss during transfer of the ampoule from the furnace to the quench bath. It is possible for the onset of nucleation to occur quite rapidly, so it is important to make the temperature change from furnace to quench bath as steep as possible. For the quench process, the Cu filler provides high thermal conductivity and rapid, uniform cooling throughout the ingot. Additionally, the Cu powder sinters during thermal processing, and provides an additional constraint on the ingot that inhibits volumetric expansion upon crystallization (useful if the amorphous phase is more dense than the crystalline). A cartoon of the design is shown in Figure 1. This technique was required to quench the CGA materials into an amorphous solid state.

Another, more direct approach to form an amorphous solid is to use a single-wall ampoule and to quickly remove the ampoule from the furnace while the liquid is molten and rapidly cool it. Some materials, with a slow crystallization rate, such as silicate glasses, can be slowly cooled in air and the material will still form an amorphous solid. Other materials need to be rapidly cooled by immersing them in a liquid to quench them. The arsenic-selenium-tellurium (AST) materials had slow enough crystallization kinetics that they could be quenched into a disordered solid by cooling or quenching them in air.

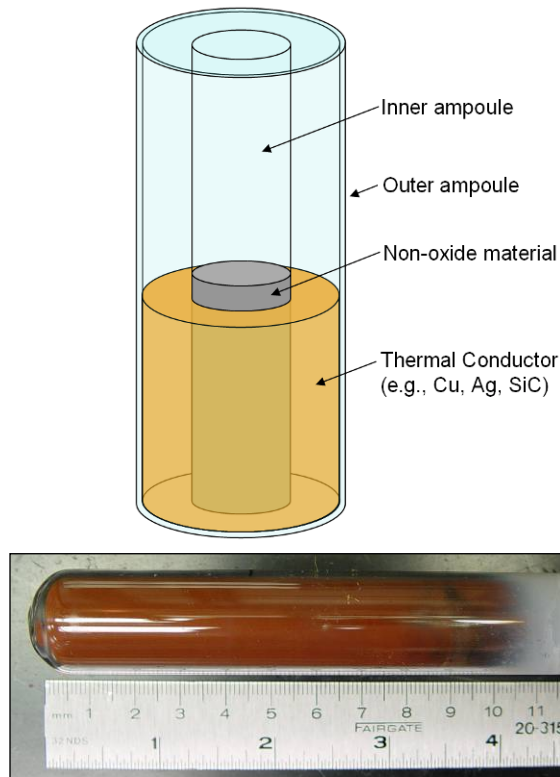


Figure 1. Top: double containment schematic; Bottom: double containment ampoule with copper.

2.2 New Chemistries

The Cd-Ge-As chemical system was the primary material family studied during the course of this project. In addition to CGA glass, other amorphous semiconductors were made from the chalcogenide family. There are three primary reasons for choosing this material system. First, chalcogenide glasses are known photosensitive materials, and have many properties that can be manipulated via exposure to sub-band-gap illumination. We project that this sensitivity to optical photons may also extend out to higher photon energies such as gamma or x-rays. Second, amorphous chalcogenide semiconductors also have physical properties that match the previously stated boundary conditions for a good gamma detector (moderate to high Z , moderate band gap, and high resistivity). And thirdly, from a processing point of view, chalcogenide glasses are good glass formers, and can be easily quenched into a disordered solid state. Three compounds in particular were chosen, As_2Se_3 , iodine doped As_2Se_3 , and $\text{As}_{40}\text{Se}_{48}\text{Te}_{12}$. Arsenic trisulfide was studied as a base-line chalcogenide material, because there has been extensive optical and electrical characterization of this material, and because it also has a well-known photoelectrical properties (e.g. it is used in photo copiers). Tellurium addition to arsenic trisulfide was chosen so as to simultaneously optimize density and resistivity Figure 2. The specific composition of the ternary compound was selected based an extensive survey of publish properties [7-9].

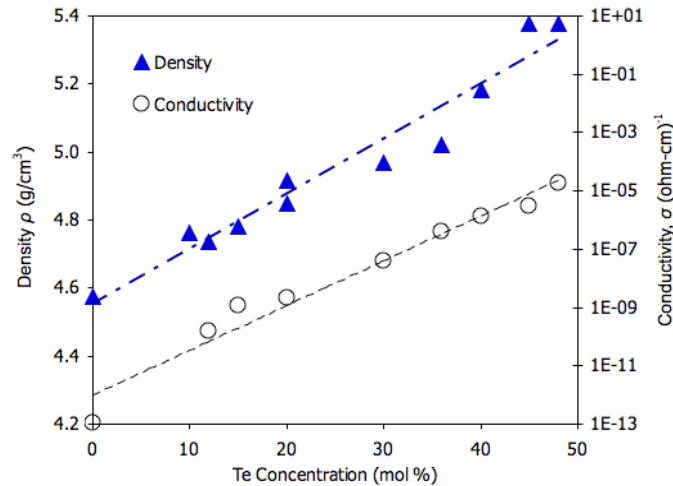


Figure 2. Plot of density and conductivity as a function of Te concentration for $\text{As}_{40}\text{Se}_{(60-X)}\text{Te}_X$ [7,8].

Doping As_2Se_3 with iodine was motivated by literature reports that stated the addition of iodine improved electrical conductivity forty-fold. Arsenic trisulfide showed a measurable response to ionizing radiation in FY07, but its high resistivity makes it a difficult material to work with, electrically. Hence, the thought was that if the material could be doped with iodine to reduce its resistivity, then it could be tailored into a more useful radiation detector. In addition to doping with iodine, the glasses were also doped with hydrogen. This was done during making the ampoule by evacuating it and back-filling it with an Ar- H_2 blended gas. Hydrogen addition was used based on the improvement it made to the optical absorption coefficient spectra for CGA glass.

This task was accomplished using the help of an undergraduate student from Clemson University. A matrix of 5 different compositions were synthesized, and their electrical properties were characterized, Table 2..

Table 2.1. Matrix of Iodine-doped Arsenic Trisulfide Compositions Synthesized and Tested.

Composition	mol % Iodine	
	Intended	Actual
As_2Se_3 w/o H_2	0	0
As_2Se_3 + H_2	0	0
As_2Se_3 + 0.5 mol% I + H_2	0.50	0.45
As_2Se_3 + 1 mol% I + H_2	1.00	0.86
As_2Se_3 + 5 mol% I + H_2	5.00	4.67

It was possible to produce amorphous As_2Se_3 doped with hydrogen and up to 5 mol% iodine. The effect of H_2 addition was a decreased density, change in optical absorption (blue-shifted), and broadening of the XRD spectra. The effect of iodine addition was mostly observed by changes in optical absorption spectra at IR wavelengths. At 5 mol% I, not only was there an IR shifted absorption edge but a variety of other additional absorption bands. Electrically, iodine addition increased the conductivity of the material up to 2 orders of magnitude. A preliminary report written by the summer student is included in Appendix A.

2.3 Progress on Identifying the New Metastable Phase

In FY07, we reported the discovery of a new, metastable Cd-Ge-As compound whose crystal structure had not been reported in the literature. This new compound can be made during double containment synthesis of CGA glass with a composition of $\text{CdGe}_{1.0}\text{As}_{2.0}$. A collage of various micrographs showing the new phase is shown in Figure 3.

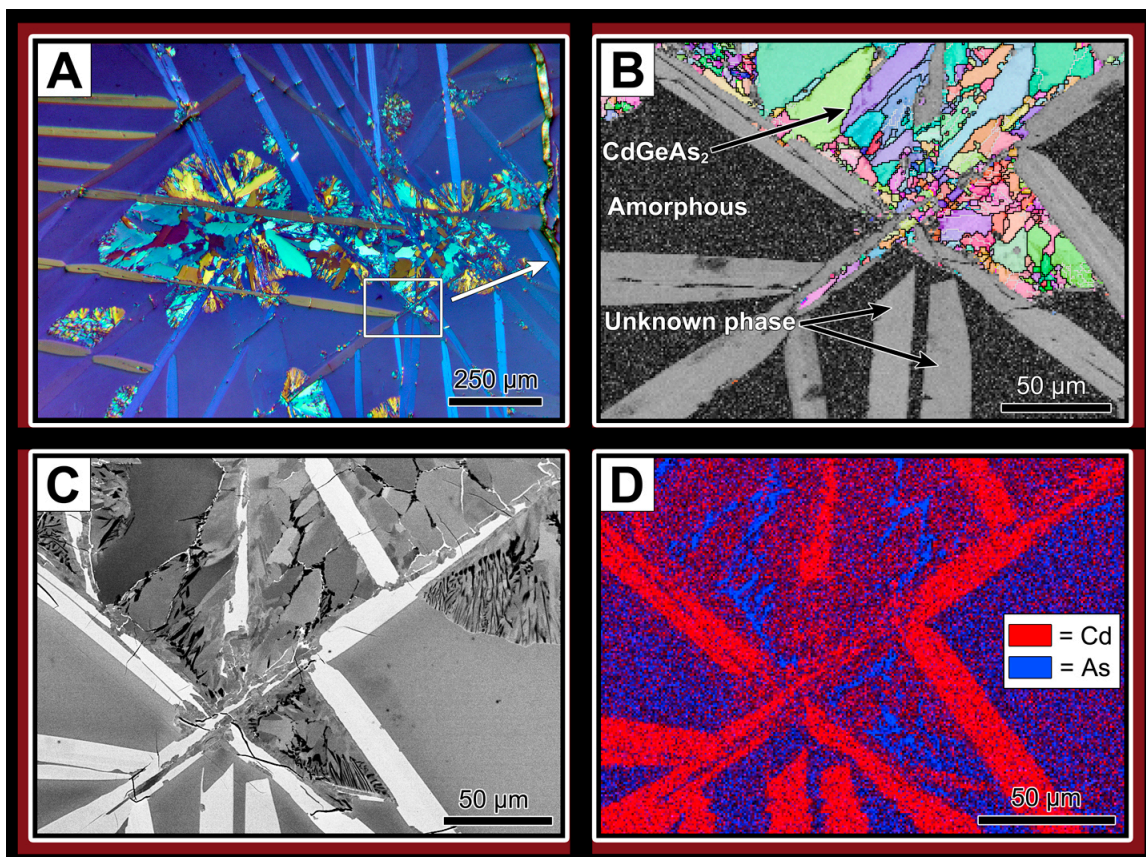


Figure 3. Microscopic analysis of metastable phases formed in Cd-Ge-As during quenching. Polarized reflected light microscopy (A) revealed two distinct crystal morphologies (polycrystals and needles) in an amorphous matrix. Examination by XRD detected CdGeAs_2 and a new, unidentified phase(s). Electron backscattered diffraction (B) determined the polycrystals (colored) were CdGeAs_2 , and confirmed the matrix was amorphous, but diffraction patterns from needles were unidentifiable. Compositional differences (Z_{ave} contrast) were accentuated using SEM BSE (C), and stoichiometry was determined by quantitative EDS mapping (D, polycrystals = CdGeAs_2 , needles = $\text{Cd}_3\text{Ge}_2\text{As}_4$). Lattice parameters, space group, and structure factor calculations for the new phase are in progress¹.

Reitveldt analysis (a method of determining the crystal structure of a material using powder XRD data) of the unknown metastable phase was attempted by UIUC. However, it was not possible to use this approach, because the technique requires that the exact chemical composition and the unit cell for the crystal structure to be known as the starting point for the analysis. Consequently, we were able to obtain the assistance of a crystallographer at PNNL who was able to fracture a glass ceramic CGA sample

¹ Winner of Best Poster Competition at the Materials Science & Technology (MS&T2007), Detroit, MI, October, 2007.

containing the metastable compound, isolate a piece containing only a couple of small crystals, and perform single crystal x-ray diffraction analysis on it.

2.4 Processing Summary

During FY08, synthesis efforts focused on making CGA glasses with hydrogen doping via the double-containment method and water quenching. Compositions with Ge contents of 0.45, 0.65, and 0.85 were able to be made fairly easily. Multiple attempts were made to synthesize CGA glass with Ge = 1.0, however the ingots typically cracked upon quenching, and often contained the needle-like crystals of the metastable phase. The liquid Ga quench method was somewhat more effective at making crack-free, crystal-free ingots of this composition, but the focus was on using the double-containment method based on the improved optical absorption properties associated with this synthesis method, so liquid Ga quenching was not pursued.

Chalcogenide glasses, due to their stronger glass-forming tendencies, were synthesized using single-walled ampoules and water quenching. A variety of different compositions were made containing Te and iodine.

The list of specimens synthesized during FY 2008 is shown in Table 2.2.

Table 2.2. Summary of ampoules produced in FY08

ID	Composition
ASGRAD-60	$(\text{Cd}_{0.885}\text{Zn}_{0.115})-(\text{Ge}_{0.225}\text{Si}_{0.225})-\text{As}_{2.00}$
ASGRAD-61	$\text{Cd}_{1.00}\text{Ge}_{1.00}\text{As}_{2.00}$
ASGRAD-62	$\text{Cd}_{1.00}\text{Ge}_{1.00}\text{As}_{2.00}$
ASGRAD-63	$\text{Cd}_{1.00}\text{Ge}_{0.85}\text{As}_{2.00}$
ASGRAD-64	$\text{Cd}_{1.00}\text{Ge}_{0.85}\text{As}_{2.00}$
ASGRAD-65	$\text{Cd}_{1.00}\text{Ge}_{1.00}\text{As}_{2.00}$
ASGRAD-66	$\text{As}_{40}\text{Se}_{60}$
ASGRAD-67	$\text{As}_{40}\text{Se}_{48}\text{Te}_{12}$
ASGRAD-68	$\text{As}_{40}\text{Se}_{48}\text{Te}_{12}$
ASGRAD-69	$\text{Cd}_{1.00}\text{Ge}_{1.00}\text{As}_{2.00}$
ASGRAD-70	$\text{As}_{40}\text{Se}_{60}$
ASGRAD-71	$\text{Cd}_{0.885}\text{Zn}_{0.115}\text{Ge}_{0.225}\text{As}_{2.00}$
ASGRAD-72	$\text{Cd}_{0.885}\text{Zn}_{0.115}\text{Ge}_{0.225}\text{Si}_{0.225}\text{As}_{2.00}$
ASGRAD-73	$\text{Cd}_{1.00}\text{Ge}_{0.45}\text{As}_{2.00}$
ASGRAD-74	$\text{Cd}_{1.00}\text{Ge}_{0.65}\text{As}_{2.00}$
ASGRAD-75	$\text{As}_{40}\text{Se}_{60}$
ASGRAD-76	$\text{Cd}_{1.00}\text{Ge}_{0.45}\text{As}_{2.00}$
ASGRAD-77	$\text{Cd}_{1.00}\text{Ge}_{1.00}\text{As}_{2.00}$
ASGRAD-78	$\text{As}_{40}\text{Se}_{60}$
ASGRAD-79	$\text{As}_2\text{Se}_3 + 0.5 \text{ mol\% I} + \text{H}_2$
ASGRAD-80	$\text{Cd}_{1.00}\text{Ge}_{0.85}\text{As}_{2.00}$

ID	Composition
ASGRAD-81	$\text{As}_2\text{Se}_3 + 1.0 \text{ mol}\% \text{ I} + \text{H}_2$
ASGRAD-82	$\text{Cd}_{0.885}\text{Zn}_{0.115}\text{Ge}_{0.225}\text{Si}_{0.225}\text{As}_{2.00}$
ASGRAD-83	$\text{As}_2\text{Se}_3 + 5.0 \text{ mol}\% \text{ I} + \text{H}_2$
ASGRAD-84	$\text{As}_2\text{Se}_3 + \text{H}_2$

3.0 Electrical Property Characterization

Semiconductor based radiation detectors require high resistivity to minimize noise and allow the detection of small signals from a single gamma event, yet they also need reasonably high charge carrier mobility so that pulses of charge carriers can be collected from discrete gamma events without overlapping each other. Thus, we characterized the electrical properties of the amorphous semiconductors we synthesized in order to evaluate them, and determine which would be the most suitable for developing into a radiation detector.

3.1 Current-voltage curves

Measuring the relationship between current and voltage as a function of temperature is one of the more basic and essential semiconductor characterization tests. The data obtained provides information about the conductivity of the material, and the activation energy for conduction. This test was done by creating a linear array of four contacts on the specimen, and by using a high-precision source meter (Keithley 6430) to create a constant flow of current between the outer two contacts, and measuring the voltage drop across the two inner contacts. The temperature would then be changed, and the system allowed to equilibrate and the voltage drop for a constant current flow would be measured again. Though a common test, working with high resistivity materials ($> 10^9$ ohm-cm) requires the use of high precision equipment in order to measure and generate the extremely small, trace currents (pA) and voltage signals involved. Another complicating factor is that the slow mobilities characteristic of amorphous semiconductors resulted in long transients when the source current or temperature was changed.

One of the more important observations from our electrical characterization studies was the increase in electrical conductivity as the specimen temperature was decreased to approximately -20°C . The expected response is a continuous decrease in electrical conduction with a reduction in temperature. A rigorous physics-based explanation for this anomalous increase in conductivity has not yet been developed. However, this behavior is very intriguing, and noteworthy. Other researchers have reported similar phenomena in other chalcogenide systems. [10,11]

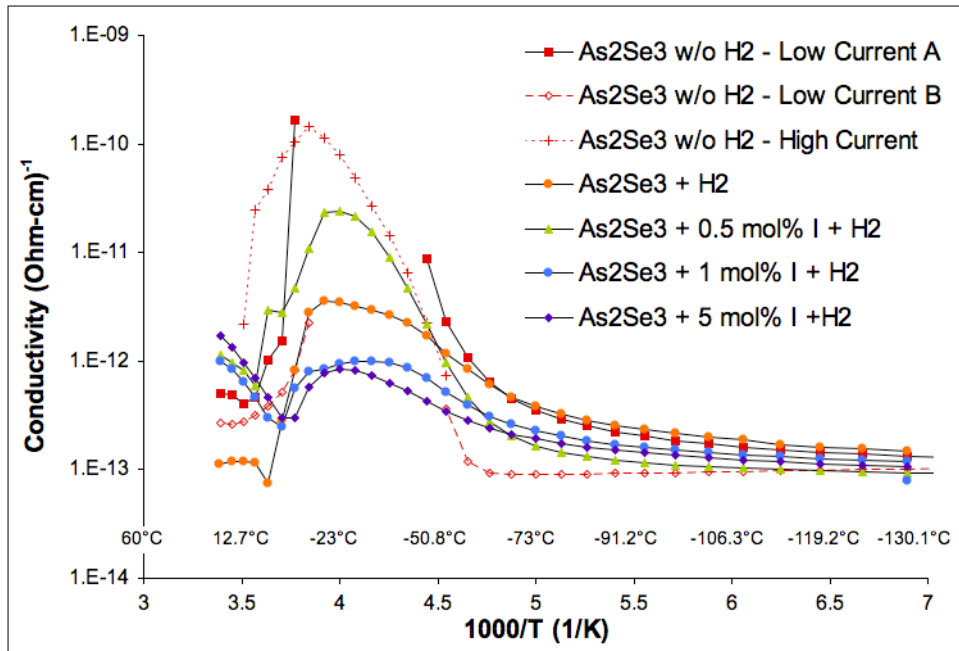


Figure 4. Electrical conductivity as a function of temperature for chalcogenide amorphous semiconductors. Note the greatly increased conductivity at $\sim -20^\circ\text{C}$.

3.2 Hall mobility

Hall mobility is a technique used to measure the mobility of charge carriers. An array of four contacts is applied to the specimen in a diamond pattern. The specimen is placed in a magnetic field with the line of flux passing perpendicular to the plane of the sample. A fixed current is sourced to flow between two of the contacts (e.g. left to right) while the voltage is measured across the other two contacts (e.g. top to bottom). As the charge carriers flow across the sample, the applied magnetic field causes them to deflect, creating an induced voltage that can be measured. This is called the Hall effect. The test is done in a variety of permutations (e.g. sourcing current left to right, right to left, magnetic field pointing up, magnetic field pointing down, etc.). The result of the data analysis is that the Hall mobility of the charge carriers in the sample can be determined. This is one way to determine the mobility of the charge carriers.

4.0 Radiation Response Testing

Alpha particles provide a convenient way to characterize the performance of a detector for several different reasons. First, they provide a 100% probability of interaction; second, each particle deposits 100% of its energy, enabling an accurate calculation of total flux; third, the location where the energy was deposited can be known, thus enabling computation of charge transport properties; and fourth, the influence of the radiation can be easily controlled or turned “on and off” using a simple shutter. Because of these experimental testing advantages, sealed alpha sources were chosen as a starting point for materials characterization.

4.1 DC Ionization Tests

The first set of experiments performed involved measuring the current voltage characteristics of a specimen with and without exposure to an alpha source. Several different experiments were done with three different materials, one was a Cd-Ge-As glass, and the other two were As-Se-Te glasses. Figure 5 shows the current-voltage curve for CdGe_{0.85}As₂ sample at -40°C over 0-100V. The change in current vs. voltage curve with and without exposure to the sealed source was pronounced – an increase of 36.4 nA.

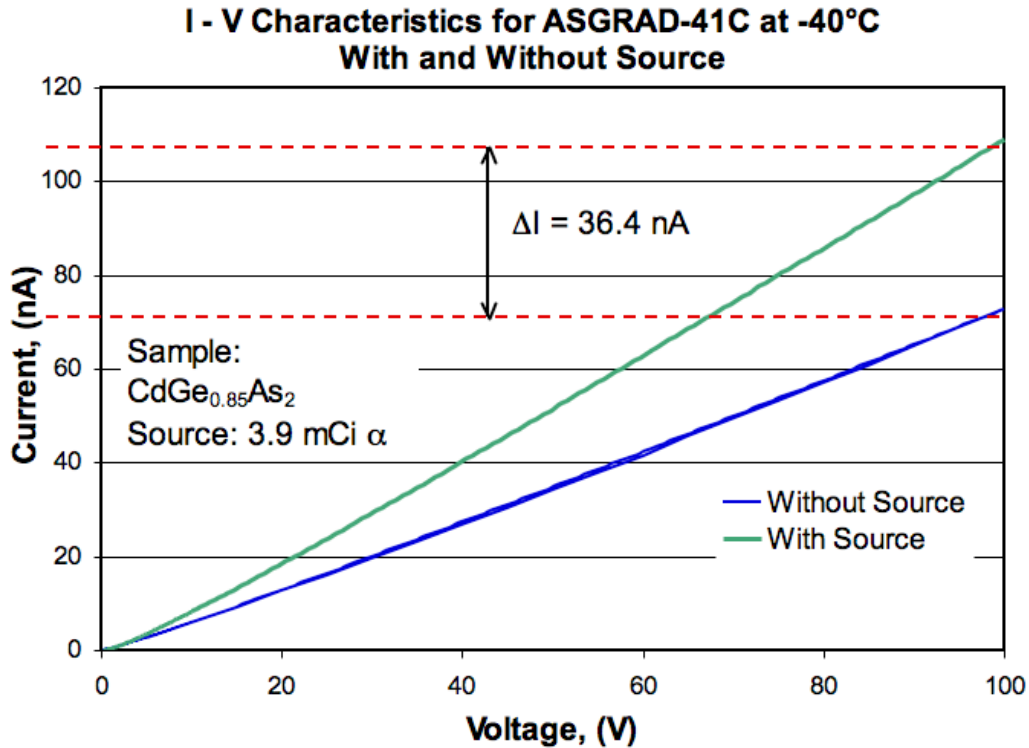


Figure 5. Current-voltage curve for CdGe_{0.85}As₂ from 0-100 V at -40°C

The next set of experiments involved measuring the transient response for exposure to alpha radiation. Direct current ionization tests were done on two different chalcogenide amorphous semiconductors at room temperature. The specimens were slowly biased up to a high voltage ($\geq 500\text{V}$), and a sealed alpha source (secured to a pivoting platform above the sample) was rotated over the top of and alternately away from the specimen. When the sealed source was over the specimen, there was a rapid increase in the measured current, almost instantaneously, that essentially reached a plateau value. After waiting for a couple of minutes, the sealed source was rotated away from the specimen, and the current again almost instantaneously decreased back to its base-line value. This test was repeated several times, thus forming a square wave function. A plot of the data for As₄₀Se₄₈Te₁₂ is shown in Figure 6. The data shows that the high bias applied to the sample was able to fill most if not all of the trap states such that when exposed to ionizing radiation, the sample became significantly more conductive, as the increase in ionization induced electron hole pairs traversed across the sample. When the ionizing radiation was removed, the population of electron hole pairs was reduced, and the conductivity rapidly returned to its base line value. The three cycles show practically no drift in the base line current level or any evidence of hysteresis. Evidence of incomplete trap state filling would have resulted in a waveform that was not square, but rather with a

curved rise time and a curved decay. The ability to fully populate trap states is an important step in improving charge carrier mobility.

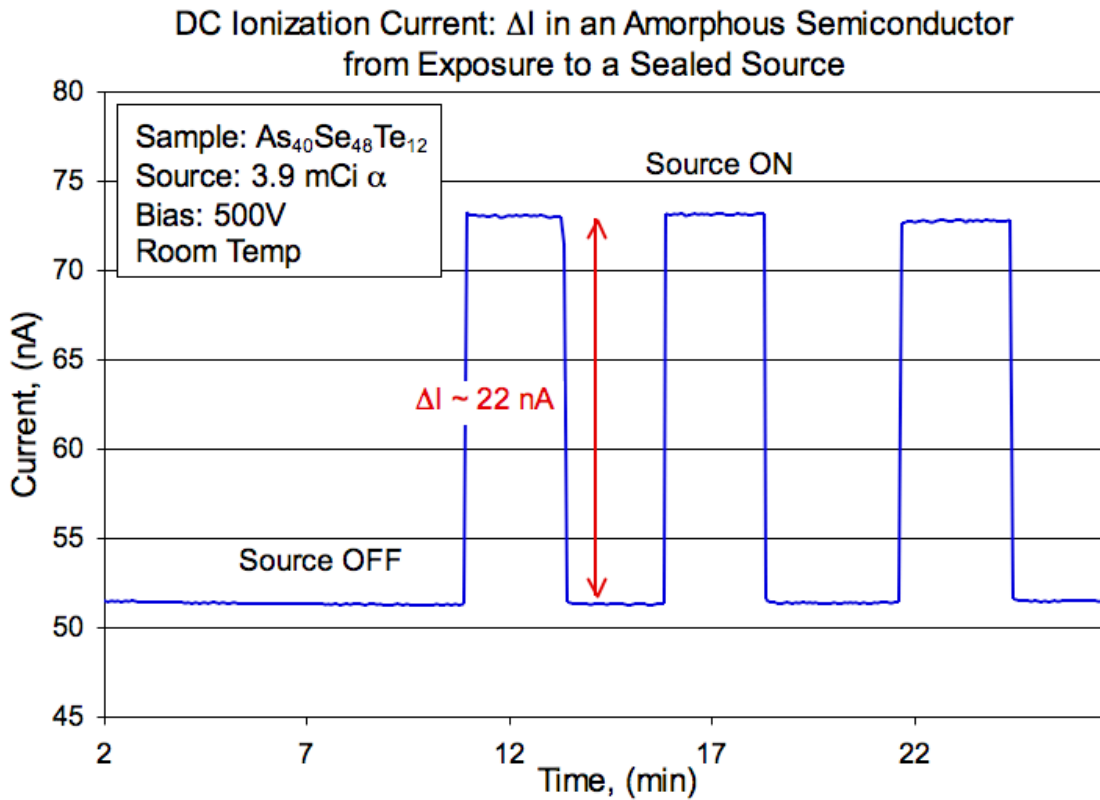


Figure 6. Current vs. time for $As_{40}Se_{48}Te_{12}$ as a function of exposure to a sealed source at room temperature and a bias of 500V.

Additional experiments were done to evaluate the variation in DC ionization current as a function of applied field. These tests were done with an amorphous specimen of As_2Se_3 . The results in Figure 7 show that as the field increased, the DC ionization current also increased. This response holds promise that improved performance with this material may be possible by using higher biases.

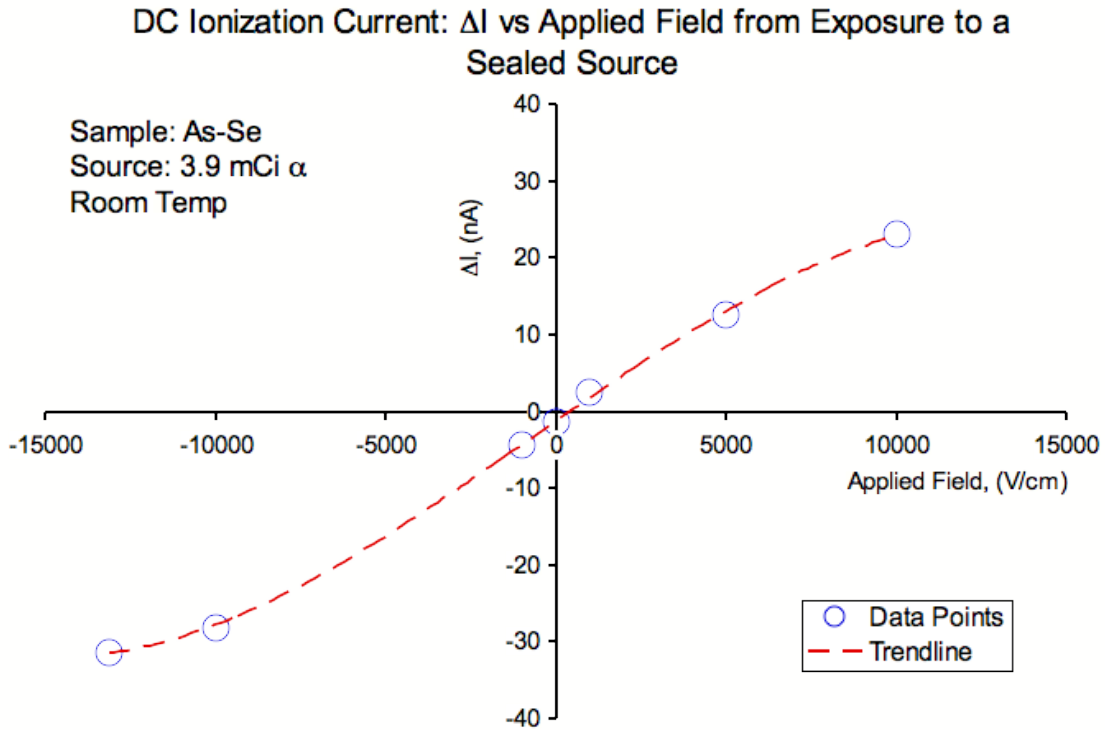


Figure 7. Variation in DC ionization current as a function of applied field.

Because the specimen was exposed to alpha radiation from a source with known activity and the sample testing geometry was known, the amount of energy deposited into the specimen could be calculated by taking into account various attenuation factors. The energy coming out of the sample could be directly computed from the measured DC ionization current (ΔI due to exposure to the source) and the applied bias voltage. A ratio of the energy output divided by the energy deposited was then computed, and the results are shown in Figure 8. This data clearly demonstrates that a signal gain or amplification can be achieved in this material. Thus, critical charge carrier losses due to trapping phenomena can be compensated for by applying a high enough gain (~ 7000 V/cm), thereby improving charge carrier collection performance. Additionally, by applying an even higher bias voltage, the material can be used as a solid state photomultiplier, and can be tuned to create a gain in signal strength greater than the energy deposited by the incident radiation. As such, these materials maybe suitable for use in applications as photodiodes coupled to scintillator detectors. These same results were reproduced with $\text{As}_{40}\text{Se}_{60}$ glass for different configurations of contacts and electrodes.

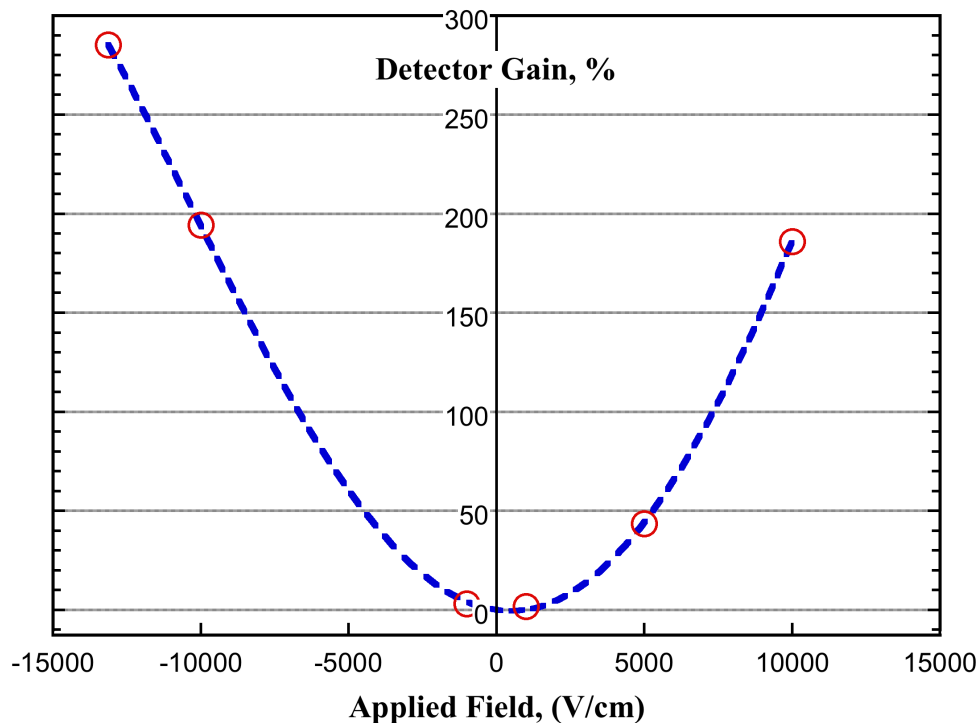


Figure 8. Detector gain as a function of applied field for amorphous As_2Se_3 for exposure to a sealed alpha source.

4.2 Pulse Testing

In addition to performing DC ionization experiments, pulse height testing was also done with selected specimens. Individual pulses (Figure 9), as well as time-lapse pulse height spectra were collected (Figure 10). Note that due to limitations in the amplifier electronics (the upper limit of the time constant was too short), the full pulse shape was truncated. Consequently, the amplifier did not collect the full height of the individual pulses as shown in Fig 1, but only a portion of the leading edge. Updated amplifiers should be able to collect the full pulse, thus producing a superior pulse height spectrum. In both instances, very distinct pulses were measured and characterized. This was one of the most significant achievements of the project.

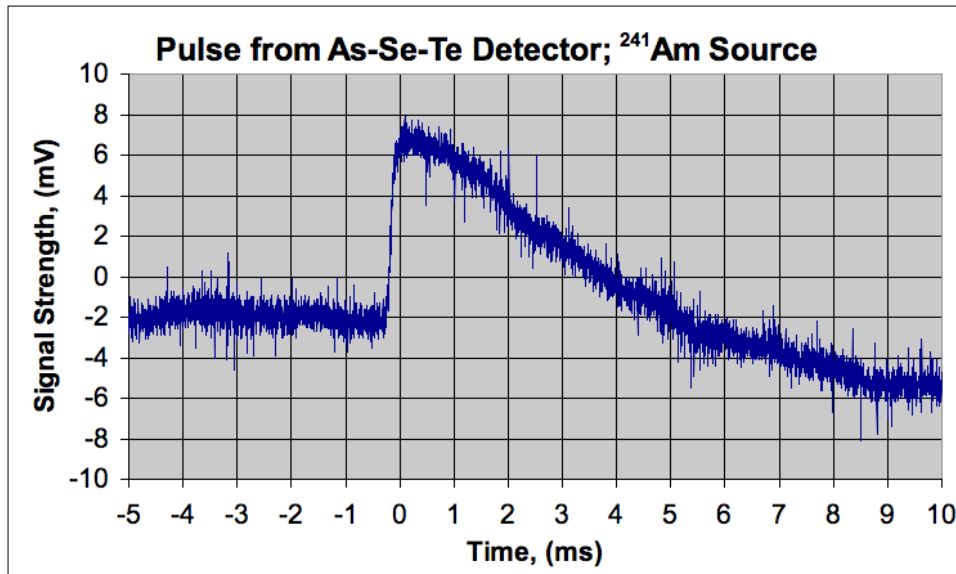


Figure 9. Pulse measured by As-Se-Te detector from an ²⁴¹Am source. The data was collected using a digital oscilloscope with the detector biased at 700V.

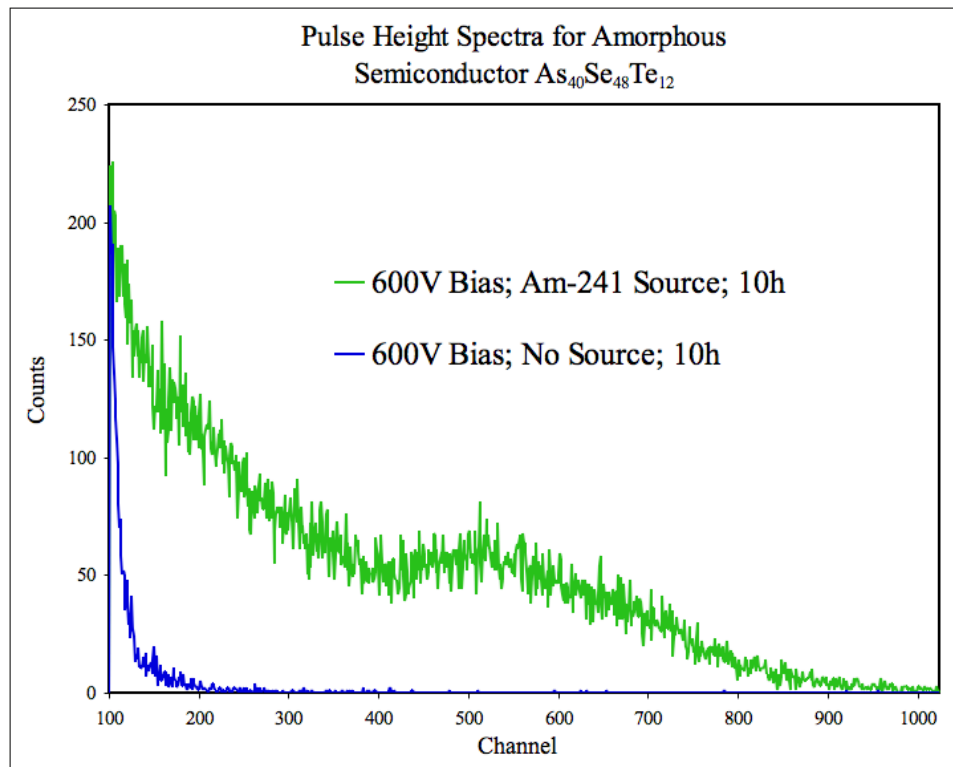


Figure 10. Pulse height spectrum from an ²⁴¹Am alpha source as collected by an amorphous semiconductor.

4.3 Summary

Overall, we have demonstrated that measuring DC ionization conductivity is a viable experimental method of screening of glasses for their potential application as gamma detectors. By cooling Cd-Ge-As glass, we were able to demonstrate measurable radiation sensitivity by comparing I-V curves collected with and without exposure to alpha radiation. The room temperature transient response to radiation was studied by measuring the DC ionization current with $\text{As}_{40}\text{Se}_{48}\text{Te}_{12}$. The sharp step changes between source on and off conditions indicates that the high bias may be sufficient to fill trap states such that ionized electron hole pairs are able to move across the material with higher mobility. The effect of varying applied field on DC ionization current measurements was studied using $\text{As}_{40}\text{S}_{60}$. The data demonstrates that not only is it possible to compensate for charge trapping losses, but that actual signal gain can be attained by operating at high biases. Actual direct pulses, and pulse height spectra were collected for $\text{As}_{40}\text{Se}_{48}\text{Te}_{12}$, which was one of the more significant results from the project. Thus, in spite of the short-range order and trapping issues, these amorphous semiconductors show a measurable response upon exposure to ionizing radiation, and consequently show promise for application as radiation detector materials for either direct detection of radiation or as photodiodes coupled to scintillators.

5.0 Collaboration with the University of Illinois at Urbana-Champaign (UIUC)

Collaboration with the University of Illinois at Urbana-Champaign (UIUC) focused on contact development (materials selection, deposition strategy, photo-lithography, etc.). Modest gains were made. The results of performing Kelvin Probe Force Microscopy (KPFM) to characterize the work function of CGA specimens are presented as a journal article in the appendix.

5.1 Conclusions of the materials characterization at UIUC

Based on materials analyses described previously, we conclude that the material is a typical amorphous semiconductor with a mobility gap in the range of 0.6-0.9 eV, a very broad band edge with a relatively low density of states near the mobility gap. The XRD data shows that the material has a wide range of interatomic distances. Although the structural and chemical properties are very uniform, the electrical and optical properties are not. The mobility gap and resistivity vary from sample to sample based on processing and composition variations. Difficulties in obtaining good quality electrical contacts have also introduced an additional complication. This may indicate variability in the nature of the material on the microscale sufficient to result in large variations in optical and electronic properties.

Amorphous hydrogenated Si (a-Si:H) is a typical amorphous semiconductor. The hydrogen reduces the density of states near the middle of the gap, making it much more straightforward to dope and making it a better semiconductor. Both a-Si:H and CGA glass are tetrahedrally bonded amorphous semiconductors. Thus, using a-Si:H as a model, a specimen of CGA glass was prepared with a hydrogen atmosphere in the process ampoule. The results show that when compared to a specimen of the same composition and under identical conditions, that a reduction in defect density and improved optical properties was obtained.

In general the conductivity of the CGA samples tested to date has been too high for room temperature radiation detection – cooling to -40°C was required to sufficiently reduce the leakage current. Several approaches to improving the situation are possible. One could investigate other processing and compositional changes that could have a greater impact on reducing the density of mid-gap states, similar to the hydrogen experiment described above. An additional approach would be to make diode-like (Schottky) contacts to the material. The depletion regions associated with these contacts can reduce local conductivity and provide a field to collect photocarriers generated by gamma rays.

5.2 Schottky contacts

We have begun investigation of the possibility of reducing the sample conductivity through contact junctions. We previously described how high work function metals such as Ti, Au, and Ag typically produce ohmic contacts to the CGA samples. Therefore the best potential for a high barrier Schottky contact would be to use a low work function metal. Typical examples used in organic electronic devices are Mg or Ca.

We have deposited and patterned Mg contacts on CGA samples as shown in Figure 11. The contacts were then studied by current/voltage measurements from Mg to Mg, from Mg to a Ag ohmic contact used for Hall effect measurements on the opposite side of the wafer, and from Mg to a probe resting directly on the CGA.

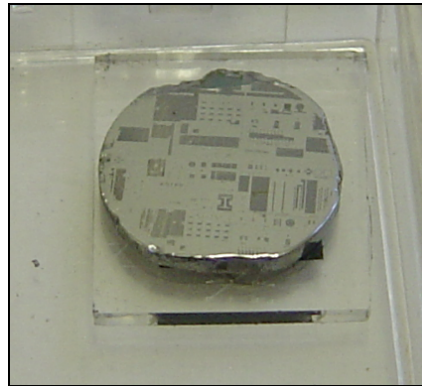


Figure 11. A test pattern and contact arrays of Mg metal deposited on Sample ASGRAD 41c. Current - voltage measurements were made from Mg contact to Mg contact, from Mg contact to an ohmic contact (used for Hall effect) on the back side of the wafer, and from Mg contact to a probe placed directly on an exposed area of the CGA.

The most dramatic results in measurements so far are a large photoconductive response between adjacent Schottky barrier contacts (Mg to Mg) when the sample is exposed to white light. An example of this behavior is shown in Figure 12. Upon exposure to white light, the current increased by over 2 orders of magnitude!

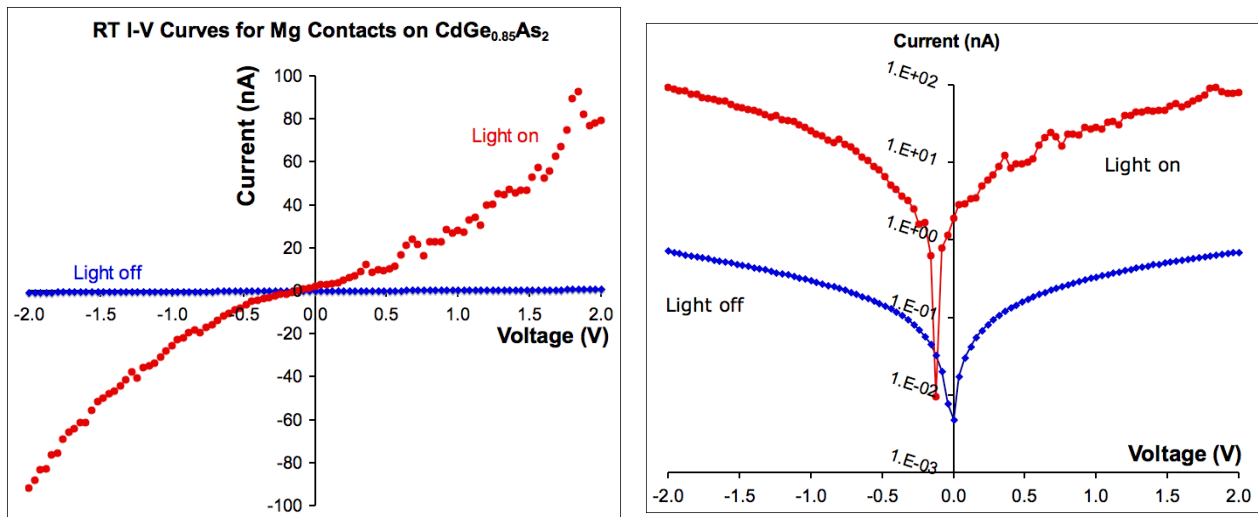


Figure 12. Left, a linear scale plot and right a logarithmic plot of the current/voltage curves for sample 41c measured between two sets of Mg contacts in the light and in the dark. A large difference in conductivity is observed.

Because transient photoconductivity is precisely the expected result of a gamma-ray detection event, this result is very exciting as a possible gamma ray detector.

The major problem with the Schottky contact study to date is the large variation in device behavior from contact to contact and the relative delicacy of the Mg contacts. The latter is easily solved by over-coating the Mg with another protective metal such as Al and/or Au. The former is more troublesome. However, if these issues can be resolved, it should be possible to build a high-performance radiation detection device.

The strategy for follow up on the preliminary measurements is to obtain new double-polished CGA samples and to deposit Mg or Ca contacts in small patterns on both sides of the sample. Measurements will be conducted both across the sample surface from contact to contact and through the thickness of the CGA. If a reproducible contact pair showing good photoconductivity through the thickness of the sample can be obtained, these will be tested for x-ray and gamma ray sensitivity.

Measurements will be conducted as a function of temperature to determine how the behavior of the contacts changes as the temperature is reduced. This will also supply information about the Schottky barrier height.

6.0 Outcomes and Future Direction

Based on the progress made during the course of this project, several potential directions for future research in amorphous semiconductor radiation detector research are discussed.

6.1 Major Project Outcomes

Four major outcomes resulted from this project:

1. Materials processing techniques were developed for synthesizing bulk amorphous semiconductors from Cd-Ge-As, As-Se-I, and As-Se-Te glass were developed. These efforts lead to innovative quenching technologies. A new metastable phase in the Cd-Ge-As family was discovered and reported.
2. Electrical characterization of two amorphous semiconductors indicated an anomalous high conductivity regime at moderately cool temperatures (-20°C). Funds were not available to fully explore this anomaly. Two tentative explanations were offered: 1) The increased conductivity was due to a semiconductor-to-metal transition, or 2) The increased conductivity was due to increased charge carrier mobility due to freezing out of vibrational phonon modes typically responsible for scattering charge carriers at room temperature. The many potential applications that could be developed from materials with these properties warrant additional funded investigation.
3. A protocol, testing apparatus, signal processing equipment, and procedure for conducting DC ionization experiments was developed. Several different amorphous semiconductors (Cd-Ge-As and As-Se/As-Se-Te) were tested with this method and demonstrated measurable, repeatable radiation response using sealed alpha sources.
4. The transient response of two different amorphous semiconductors to radiation at RT was demonstrated using sealed alpha sources. Individual pulses as well as pulse height spectra were collected.

6.2 Future Direction

Four main areas of research for continued development of amorphous semiconductor radiation detectors are suggested:

1. Development of Schottky contacts for amorphous semiconductors. This includes the following key steps:
 - a. Identify the correct metal (or sequence of metals e.g. Mg-Al-Au) to use to create a charge-depleted interface,
 - b. Determine the appropriate surface treatment to clean and prepare the semiconductor
 - c. Develop a suitable photolithographic and metallization process to create the contact
2. Sustained electrical characterization of the anomalous high conductivity regime found in As-Se, and As-Se-Te amorphous semiconductors to develop a physics-based explanation for the phenomena and rule out experimental artifacts.

3. Development of a thermoelectrically cooled amorphous semiconductor testing apparatus to take advantage of the improved conductivity (charge carrier mobility) at modestly cool temperatures.
4. Continued DC ionization and transient pulse testing of the advanced amorphous semiconductors developed as a consequence of improved Schottky contacts, and testing of thermoelectrically cooled detectors.

7.0 References

- (1) Rud, V.; Rud, Y.; Poluushina, I.; Ushakova, T.; Iida, S., "Observation of Record Electron Hall Mobility in CdGeAs₂ Single Crystals," *Jpn. J. Appl. Phys.*, **39** [Suppl. 39-1] 266-267 (2000).
- (2) Rud, V. Y.; Rud, Y. V.; Pandey, R.; Ohmer, M. C., "Evidence of high electron mobility in CdGeAs₂ single crystals"; pp. 439 in *Infrared Applications of Semiconductors III. Symposium (Materials Research Society Symposium Proceedings Vol.607)*, Edited by Mater. Res. Soc, Boston, MA, USA, 2000.
- (3) Roy, U. N.; Groza, M.; Cui, Y.; Burger, A.; Bell, Z. W.; Carpenterl, D. A., "Crystal growth, characterization and fabrication of AgGaSe₂ crystals as a novel, material for room-temperature radiation detectors"; pp. 177 in *Proceedings of SPIE - The International Society for Optical Engineering, Vol. 5540*. Edited by International Society for Optical Engineering, Bellingham, WA 98227-0010, United States, Denver, CO, United States, 2004.
- (4) Hruby, A.; Stourac, L., "Semiconducting glasses based on CdAs₂," *Materials Research Bulletin*, **4** [10] 745-756 (1969).
- (5) Risbud, S. H., "Processing and properties of some II-IV-V₂ amorphous and crystalline semiconductors," *Applied Physics A: Materials Science & Processing*, **62** [6] 519-523 (1996).
- (6) Stourac, L., "Thermal conductivity of semiconducting amorphous CdGeAs₂," *Czech. J. Phys.*, **V19** [5] 681-684 (1969).
- (7) Kokorina, V. F., *Glasses for infrared optics*. CRC Press, Boca Raton, FL, 1996.
- (8) Vengel, T. N.; Kolomiets, B. T., "Vitreous Semiconductors, some properties of materials in the As₂Se₃ - As₂Te₃ System II," *Soviet Physics Technical Physics*, **2** 2314-2319 (1957).
- (9) Mahadevan, S.; Giridhar, A.; Rao, K. J., "Study of electron transport in As-Se-Te glasses," *J. Phys. C: Solid State Phys.*, **10** 4499-4510 (1977).
- (10) Qamhieh, N.; Willekens, J.; Brinza, M.; Adriaenssens, G. J., "Anomalous DC dark conductivity behaviour in a-Se films," *J. Phys.: Condens. Matter*, **15** L631-L635 (2003).
- (11) Kushwaha, N.; Shukla, R. K.; Kumar, S.; Kumar, A., "Anomalous behaviour in dark conductivity and photoconductivity in a-Se₈₅Te_{15-x}Pb_x thin films at low temperatures," *Materials Letters*, **60** 3260-3264 (2006).

8.0 Appendix A

Journal articles that were generated as a result of NNSA funding for this project:

- (1) Johnson, B. R.; Riley, B. J.; Sundaram, S. K.; Crum, J. V.; Henager, C.; Zhang, Y.; Shuthanandan, V.; Seifert, C. E.; Ginhoven, R. M. V.; Chamberlin, C.; Rockett, A.; Hebert, D.; Aquino, A., "Synthesis and Characterization of Bulk Vitreous Cadmium Germanium Arsenide," *Journal of the American Ceramic Society*, **92** [6] 1236-1243 (2009).
- (2) (1) Johnson, B. R.; Crum, J. V.; Sundaram, S. K.; Ginhoven, R. M. V.; Seifert, C. E.; Riley, B. J.; Ryan, J. V., "DC Ionization Conductivity of Amorphous Semiconductors for Radiation Detection Applications," *Transactions in Nuclear Science*, **56** [3] 863-868 (2009).
- (3) (1) Riley, B. J.; Johnson, B. R.; Crum, J. V.; Thompson, M. R., "Tricadmium Digermanium Tetraarsenie: A New Crystalline Phase Made with a Double-Containment Ampoule Method," *Journal of the American Ceramic Society*, **95** [7] 2161-2168 (2012).
- (4) Damon N. Hebert, Allen J. Hall, Angel R. Aquino, Angus A. Rockett Richard T. Haasch Bradley R. Johnson, Brian J. Riley, "Kelvin probe force microscopy of metal contacts on amorphous cadmium germanium arsenide", *Journal of the American Ceramic Society*, submitted, Nov 2012

Synthesis and Characterization of Bulk, Vitreous Cadmium Germanium Arsenide

Bradley R. Johnson,[†] Brian J. Riley, Shanmugavelayutham K. Sundaram, Jarrod V. Crum, Charles H. Henager Jr., Yanwen Zhang, Vaithiyalingam Shutthanandan, Carolyn E. Seifert, Renee M. Van Ginhoven, and Clyde E. Chamberlin

Pacific Northwest National Laboratory, Richland, Washington 99354

Angus A. Rockett, Damon N. Hebert, and Angel R. Aquino

University of Illinois at Urbana-Champaign, Urbana, Illinois 61801

Cadmium germanium diarsenide glasses were synthesized in bulk form ($\sim 2.4 \text{ cm}^3$) using procedures adapted from the literature. Several issues involved in the fabrication and quenching of amorphous CdGe_xAs_2 ($x = 0.45, 0.65, 0.85, \text{ and } 1.00$, where x is the molar ratio of Ge to 1 mol of Cd) are described. An innovative processing route is presented to enable fabrication of high-purity, vitreous, crack-free ingots with sizes up to 10 mm diameter, and 30–40 mm long. Specimens from selected ingots were characterized using thermal analysis, optical microscopy, scanning electron microscopy, energy dispersive spectroscopy, particle-induced X-ray emission, Rutherford backscattering, secondary ion mass spectrometry, X-ray diffraction, density, and optical spectroscopy. Variations in properties as a function of processing conditions and composition are described. Results show that the density of defect states in the middle of the band gap and near the band edges can be decreased three ways: through suitable control of the processing conditions, by doping the material with hydrogen, and by increasing the concentration of Ge in the glass.

I. Introduction

AMORPHOUS semiconductors are the key function material in several important technological areas such as xerography,¹ photovoltaics,² medical imaging plates,³ and TV vidicon tubes.⁴ For many applications, thin films are optimal and can be easily fabricated. However for some uses, such as radiation detection, bulk materials are required. Single crystal materials (e.g., Si, Ge, and CdZnTe) are typically preferred for these applications, but there is a need for cost-effective semiconductors that can be operated without cryogenic cooling and that have sufficient bulk volume to efficiently interact with and detect γ radiation.^{5,6} Bulk amorphous semiconductors may be able to contribute to this need, if one can be found with suitable electrical properties.

Cadmium germanium diarsenide (CGA or CdGeAs_2) belongs to the II–IV–V₂ family of chalcopyrite semiconductors. It has attracted recent attention for its optical properties because of its extraordinarily high nonlinear optical coefficient for second harmonic generation (236 pm/V).^{7–9} However, it is also a semicon-

ductor with very high room temperature mobility ($10^4 \text{ cm}^2 \cdot (\text{V} \cdot \text{s})^{-1}$).¹⁰ Additionally, it is one of the few chalcopyrite semiconductors that can be synthesized as an amorphous material in bulk form. A program of research was initiated to fabricate this material and evaluate its suitability for radiation detection applications. This paper is focused on synthesizing bulk amorphous CGA compounds, while another has been written describing the radiation response properties of these materials.¹¹

Glass formation within the CdGe_xAs_2 system has been reported for $x = 0.02$ – 1.3 .^{12–18} The basic glass forming network unit for this amorphous compound has been attributed to CdAs_2 and glass formation has been shown with the addition of a number of different ternary elements (Si, Ti, In, Al, Sb, Mg, and Ga) as well as Ge.^{13,15,19} Additionally, substitution of Zn for Cd and Si for Ge has been demonstrated.¹⁶

The broad compositional flexibility in regard to glass formation would seem to indicate that this material is a good glass former. Reports in the literature indicate it is possible to air quench bulk samples of CdGeAs_2 up to 10 mm in diameter into a vitreous state.¹⁷ However, our experience has been contrary. We have found that this is actually a fragile glass-forming system and that it is very difficult to water quench even modest volumes (10 mm diameter, 30–40 mm tall) of the molten liquid into a bulk vitreous ingot without fracturing it. Although quenching molten compounds into a vitreous state is difficult enough for fragile glass formers, accomplishing this without fracturing the material because of excessive thermal stresses is even more challenging.¹⁷ Consequently, it was necessary to develop new processing techniques in order to produce bulk, crack-free, vitreous specimens. The major modification (from typical anoxic material processing procedures that involve evacuated fused quartz ampoules) was the development of a double containment (DC) ampoule method as described below.

II. Experimental Procedures

(1) Synthesis

Thermal analysis experiments were used to study the elemental reactions involved with forming CGA compounds and also to measure important glass properties. Reported literature information was used as a starting point to guide experiments.¹⁴ Batching reactions of the constituent elements were studied to identify key thermodynamic events. These experiments were conducted using a Seiko TGA/DTA320 (Northridge, CA), which is a combination of thermogravimetric analyzer (TGA) and differential thermal analyzer (DTA). Hermetically sealed aluminum pans were used to minimize material loss because of volatilization. A total sample mass between 20 and 30 mg was used, at a heating rate of $10^\circ\text{C}/\text{min}$ up to 620°C , and with a $150 \text{ cm}^3/\text{min}$ purge flow of ultra high purity Ar gas. Glass

B. Dunn—contributing editor

Manuscript No. 24976. Received July 12, 2008; approved January 27, 2009.

The Environmental Molecular Synthesis Laboratory, a national scientific user facility sponsored by the Department of Energy at PNNL, and the Materials Research Laboratory, also a national scientific user facility sponsored by the Department of Energy at the University of Illinois at Urbana-Champaign. This work was supported by the U.S. Department of Energy, Office of Nonproliferation Research and Development (NA-22). Pacific Northwest National Laboratory (PNNL) is operated by Battelle for the Department of Energy under contract DE-AC06-76RLO 1830.

[†]Author to whom correspondence should be addressed. e-mail: bradley.johnson@pnl.gov

using liquid Ga (70°–150°C) as a quenchant. In their work, quenching in warm liquid Ga was supposed to provide some annealing of the sample during the quench and reduce thermal shock. Although expensive, liquid Ga was an appealing quenchant because of its low melting point (29.76°C), very high boiling point (2204°C), and low vapor pressure.²³ DC ampoules were typically quenched in a water bath at room temperature. After quenching, the ingots were annealed at $\sim 50^\circ\text{C} < T_g$ for that composition (as determined by DTA/TGA/DSC) for ~ 8 h to aid in reducing thermally induced stress in the glasses. After cooling, the ingots were cast into an acrylic (Buehler VariKleer[®], Lake Bluff, IL) to reduce fracture during sawing. They were then sectioned into thin wafers 1–3 mm thick, polished, and analyzed.

(2) Characterization

Specimens were sectioned from the ingots and characterized using a variety of techniques to determine processing-property as well as composition-property relationships. Optical microscopy was performed with a Leitz Orthoplan optical microscope using reflected cross-polarized light, a $1/4 \lambda$ calcite wave plate, and a rotating stage. This enabled the rapid detection of crystalline phases as the variations in birefringence and crystallographic orientation caused the different grains to go in and out of extinction at different angles as the stage was rotated. X-ray diffraction experiments were conducted with a Scintag PAD V diffractometer using $\text{CuK}\alpha$ radiation ($\lambda = 0.15406$ nm, 45 kV, and 40 mA) and equipped with a Peltier-cooled Si(Li) solid-state detector in a θ - 2θ geometry. Samples were analyzed in a step-scan approach, typically from 10° up to $110^\circ 2\theta$ with a step size of $0.04^\circ 2\theta$ and a dwell time of 6 s/step. Each sample was mounted on a holder that rotated in the x - y plane to minimize preferred orientation effects. Samples were analyzed to detect and identify the presence of any crystalline phase(s) and for radial distribution function analysis. A JEOL 5900 (Joel Ltd., Peabody, MA) scanning electron microscope with a Robinson Series 8.6 backscattered electron (BSE) detector and EDAX Genesis energy dispersive spectrometry (EDS) system were used to analyze selected specimens for homogeneity and phase separation. Density measurements were accomplished using a Micromeritics AccuPyc 1330 (Norcross, GA) helium pycnometer.

Composition determination, uniformity, and trace element contamination experiments were performed using particle-induced X-ray emission (PIXE) spectroscopy and Rutherford backscattering spectroscopy (RBS) on the linear accelerator at the Environmental Molecular Sciences Laboratory (EMSL, Richland, WA). PIXE measurements were carried out with a 2.5 MeV H^+ beam, and the X-rays emitted during the de-excitation process were analyzed using a Li-drifted Si detector positioned at an exit angle of 39° . The system was calibrated using a standard from the National Institute for Standards and Technology. The GUPIX computer code, developed at the University of Guelph, Canada, was used to fit the experimental data. Background subtraction to remove bremsstrahlung effects was performed and the areas under each peak were converted into concentrations using experimental parameters such as energy, incident and exit angles, charge, solid angle of the detector, absorber thickness, and detector response functions. The experimental parameters were then calibrated against the known concentrations of the standard. Following calibrations, PIXE measurements were collected on CdGe_xAs_2 samples.

Rutherford backscattering experiments were performed with 2.0-MeV He^+ ions at a scattering angle of 165° . The SIMNRA simulations code was used to fit the RBS data. These experiments were performed to determine absolute concentrations of the major constituent elements. Instead of detecting characteristic X-rays, the incident ions that are subsequently scattered from target atom nuclei are detected and measured. This provides information on the mass and depth of the target atoms.

Additional compositional analyses were conducted using secondary ion mass spectroscopy (SIMS). These measurements

were performed with a Cameca IMS-5f instrument using an O_2 ion beam. This analysis condition is highly sensitive to electropositive species and to a broad range of transition and other metals. The results were used to corroborate compositional data obtained by PIXE and RBS.

Current-voltage curves as a function of temperature were measured with a Hall effect testing device consisting of a MMR Technologies analysis head and H-50 van der Pauw controller. The sample temperature was controlled by a heater and a CTI Cryogenics refrigerator with a base temperature of -259°C . The sample was mounted on the refrigerator and reheated with the heater power controlled by a Lake-shore 330 autotuning temperature controller to a set point temperature. A magnetic field of 1 T (Varian Associates electromagnet) could be applied to the sample for Hall effect. Data was taken and analyzed using a custom Labview program. Ohmic contacts were made by evaporating high work-function metals such as Ti, Au, or Pd onto polished CGA disks. Four contacts were applied in a Van der Pauw geometry. Indium-coated wires were attached to the contacts using indium solder. Voltages applied to the samples depended upon the current to be driven and this current was minimized based on signal-to-noise requirements as this produced the most reliable results. Typical currents were of the order of 1 nA for most measurements. The conductivity of the sample was calculated from the I - V data based on the geometry of the test.

The optical bandgap of these materials were characterized using a Varian Cary 5 G UV-Vis-NIR spectrophotometer with a spectral range of 175–3300 nm and an out-of-plane double Littrow Monochromator. Infrared (FTIR) spectroscopy and UV-Vis-NIR spectroscopy were performed on all samples using a Thermo 6700 FTIR and a Varian Cary 500 spectrometer, respectively. Polished windows of each composition were mounted and transmission measurements were collected from 2.5 to 25 μm and 300 to 2500 nm on the Thermo and Varian instruments, respectively.

III. Results and Discussion

Thermal analysis studies of the batch reactions between the three elements detected three significant endotherms: the melting point of Cd (observed at 325°C) and two additional endotherms at 573° and 592°C . Neither of these corresponded to an obvious phase transition for one of the elemental constituents. However, the As–Cd phase diagram²⁴ showed several phase transitions associated with the As_2Cd_3 α , α' and β phases, with one at 578°C . Furthermore the CdAs_2 – As_2Cd_3 eutectic is given as melting at 610°C . We hypothesize that the endotherms at 573° and 592°C represent phase transitions in a Ge-poor As–Cd compound or in the ternary CdGe_xAs_2 , itself. A distinct, primary, exothermic reaction to form CdGe_xAs_2 was not obvious in the DTA data but may have been obscured by the rise in the data beginning at the 573°C endotherm and continuing on to the end of the experiment. The use of hermetically sealed-Al pans limited the experiments to 620°C . Even at that temperature, reactions between the molten Cd, As and/or Ge with the Al pan were noted based on *ex situ* observations of chemical attack on the pan. Therefore, the observed rising slope in the DTA data above 573°C probably also included a significant component of reaction with the Al pan.

Subsequent thermal analysis experiments of quenched CGA glasses of various compositions were able to detect both the glass transition temperature and the crystallization temperatures. The results from all of the tests are shown in Table I. The data from the batch reaction and the glass measurement experiments were used to develop the heating rate profile used to process, quench, and anneal the CGA specimens. The results were similar to the values of a more extensive study by Hong, *et al.*¹⁴ Variations between the data sets may be attributed to differences in sample volume (smaller with Hong and colleagues) and purity (e.g., final ampoule sealing pressure was higher with

Table I. Glass Transition (T_g) and Crystallization (T_c) Temperatures for Various Cadmium Germanium Diarsenide Glasses

Name	Quench method	Composition	T_g (°C)	T_c (°C)	$\rho_{\text{pycn.}}$ (g/cm ³)
G 0.45	DC	CdGe _{0.45} As ₂	353	440	5.8094
G 0.65	LG	CdGe _{0.65} As ₂	372.2	463.9	5.7774
G 0.85	DC	CdGe _{0.85} As ₂	373.7	448.5	5.7405
G 1.00	LG	CdGe _{1.00} As ₂	390	448	5.7171

Hong's vs. This study: 10^{-3} vs 10^{-5} Pa, or 10^{-5} vs 10^{-7} torr, respectively).

Anecdotally, greater success was experienced in obtaining crack-free, crystal-free CdGe_xAs₂ ingots for $x = 0.45$ and 0.85 than for the other compositions. In contrast, a greater percentage of ingots for compositions with $x = 0.65$ and 1.0 failed due to either cracking or crystallization or both. This was in contrast to the findings of Hong *et al.*,¹⁴ where they computed a maximum in glass formation tendency between $x = 0.3$ and 0.6 based on thermal analysis data. Additional thermal analysis experiments at finer compositional intervals are needed to better characterize these variations in glass formability. In addition to thermal glass formability criteria (based on differences between the crystallization and glass transition temperatures) variations in residual oxygen content have also been reported to affect glass formability. Hruby *et al.*²⁷ stated that when they took the effort to remove oxygen and water contamination from their starting materials and ampoule walls it was much more difficult to form bulk As–Te glasses. Because these Cd–Ge–As glasses were processed at significantly lower oxygen and moisture contamination levels than reported previously, it is possible that a similar effect is at work. To our knowledge, the influence of trace oxygen content on glass formability in Cd–Ge–As glass has not yet been rigorously examined.

Initial experiments synthesizing bulk CGA glasses were not successful because of failed and cracked ampoules. The source of the cracking was attributed to Cd attack of the fused quartz wall. Pyrolytic graphite coatings (described previously) were attempted as a means to address this problem, but yielded mixed results. They were effective in eliminating the problem of ampoule failures because of Cd attack of the fused quartz, but they introduced several additional problems. We observed that the CGA melts had a tendency to wet and adhere to the walls of the pyrolytically coated ampoules. This reduced ingot yield, because a film of the CGA glass remained along the ampoule wall rather than pool and collect as a bulk ingot. Additionally, the pyrolytic coatings themselves were not sufficiently adherent to the ampoule wall, but became incorporated into the melt. SEM examination of polished cross sections from ingots made in pyrolytically coated ampoules showed evidence of carbon contamination in the ingot. Electrical characterization tests performed by measuring the conductivity as a function of temperature showed that an ingot synthesized in a pyrolytically coated ampoule was over an order of magnitude more conductive than the ingot made in a bare ampoule and its conductivity also had significantly lower temperature dependence. Consequently, pyrolytic coatings had to be abandoned. As a result, the specific element loading sequence described previously was developed, and proved to be an effective means to address the problem of Cd reacting with fused silica.

Development of an effective quenching process to form bulk, amorphous, crack-free ingots proved to be challenging. Optical microscopy (Fig. 1) and XRD (see later discussion) were the primary analytical techniques used to evaluate different quenching methods. Polished cross-sectioned specimens were imaged using cross-polarized reflected light microscopy (Figs. 1(A) and (B)). Air quenching, though reported in the literature to be effective,¹⁷ yielded only polycrystalline ingots. Water quenching was somewhat more effective, but it was only able to produce ingots that were partially amorphous around the perimeter (Fig. 1(B)) or cracked. However, by using the DC ampoule

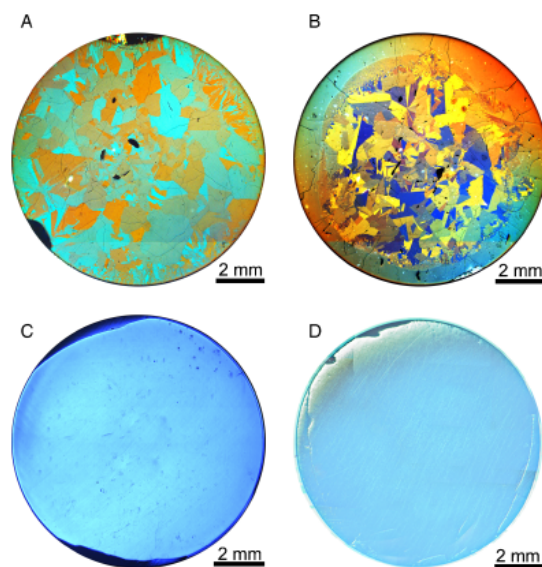


Fig. 1. Polarized reflected optical micrographs of polished cross-sections of CdGe_xAs₂ ingots. A large-grained, poly-crystalline microstructure resulted from air quenching specimens with $x = 1.0$ (A). Water quenching the same composition yielded a microstructure with an amorphous rim and a smaller-grained polycrystalline interior (B). By reducing x (0.45–0.85), and using the DC method, amorphous and crack-free ingots were obtained, (C). Similar results were also achieved by quenching in liquid Ga for values of x up to 1.0 (D).

method, and reducing the Ge content, it was possible to form crack-free, amorphous ingots (Fig. 1(C)). The improvement in glass formability by reducing Ge content was anticipated, based on reports by Hong and colleagues.^{14,28} Quenching in liquid Ga was also effective, and an example of a Ge = 1.0 ingot is shown in Fig. 1(D).

Extensive materials characterization was necessary in order to validate that the processing methodology was not introducing contamination or producing artifacts that would obscure or interfere with analyzing performance data. Stoichiometric control of the batching and synthesis of CGA glass was validated using RBS and PIXE in a complimentary fashion. The absolute elemental concentration of Cd was measured with RBS (Fig. 2). Unfortunately, overlap of the data for As and Ge interfered with precise measurement of their individual concentrations. Consequently, PIXE was used to identify the elemental ratio of As:Ge while normalizing to the RBS measurement for Cd. This method was used to provide accurate compositional measurements (Fig. 2). Specimen homogeneity was evaluated by translating the specimen and making measurements at ~ 1.2 – 1.5 mm intervals across the diameter of the disk. Different slices taken from the same ingot were also analyzed to establish homogeneity along the axis of the ingot. The experimental results are shown in Table II and indicate that stoichiometry was maintained within ± 1 at.%. The extra, unlabeled peaks in the PIXE plot were attributed to pulse pile-up and escape peak artifacts, based on complementary analysis of these specimens by SIMS.

SIMS was chosen for the purpose of corroborating the RBS and PIXE results as well as to analyze specimens for trace elemental contamination. Four different specimens were examined. There was no evidence of any transition metals. Transition metal contaminants have been shown to have a measurable effect on electrical transport properties in CGA glass.^{29,30} Consequently, this type of contamination could seriously interfere with electrical characterization experiments, and prevent unambiguous correlations between processing, composition, and property relationships. This data combined with the results

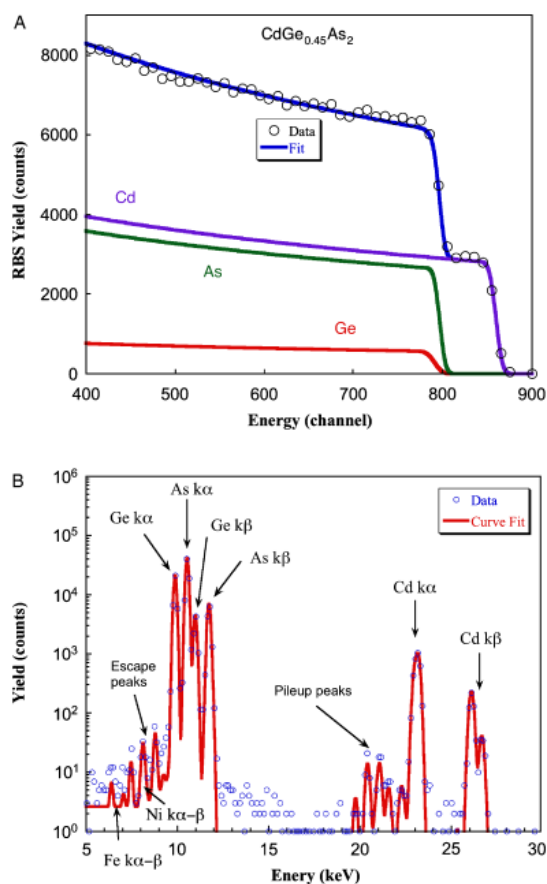


Fig. 2. Graph of RBS (A) and PIXE (B) data for a $\text{CdGe}_{0.45}\text{As}_2$ glass specimen.

from RBS and PIXE substantiated that the synthesis process was able to accurately achieve the specified stoichiometry and that the process was clean, and essentially free of trace contamination down to ppm levels.

X-ray diffraction results of a CGA glass with 0.85 Ge content are shown in Fig. 3(A), and are typical of all compositions. Short range order in the CGA glasses was evaluated by calculating the atomic pair distribution function (PDF) from the amorphous XRD spectra.^{31–34} For PDF calculations, XRD spectra were collected from 5° – 144° 2θ at a step interval of 0.05° with a dwell time of 3 s/step, and summing up the results of three scans. The spectra were collected using the same diffractometer described previously. Atomic PDF calculations were performed using the computer program “PDFgetX2”³⁴. The

Table II. Summary of Line Scan Compositional Data Computed from Combined RBS and PIXE Analysis for CdGe_xAs_2 Glass (Measurement Accuracy, $\pm 0.5\%$)

Spot	Cd (at.%)	Ge (at.%)	As (at.%)
0	25.6	24.7	49.6
1	25.9	24.6	49.5
2	25.9	24.6	49.5
3	26.0	24.6	49.4
4	25.9	24.6	49.4
5	25.9	24.7	49.3
6	25.7	24.8	49.5
Average:	25.9	24.7	49.5

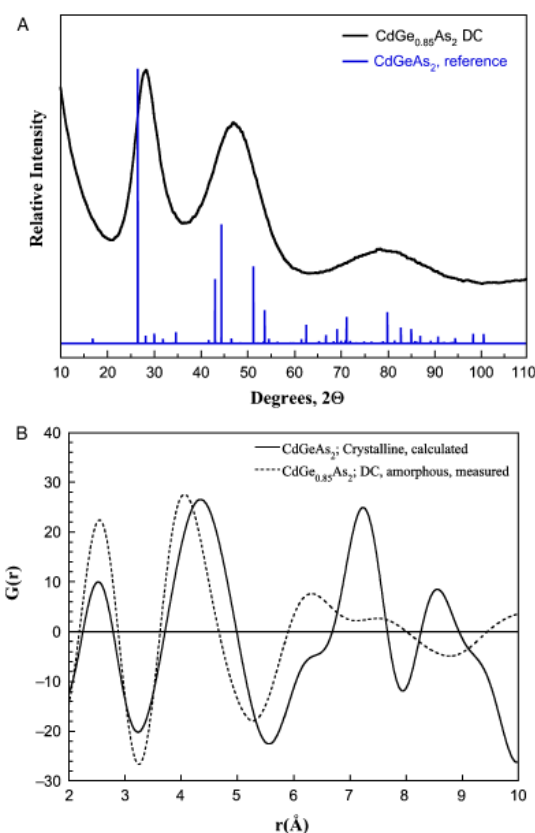


Fig. 3. X-ray diffraction spectra of $\text{CdGe}_{0.85}\text{As}_2$ glass verifying their amorphous structure (A) and simulated pair-distribution function for a CdGe_xAs_2 glass for $x = 0.85$ (B).

results are shown in Fig. 3(B). Detailed measurements of the PDF nearest neighbor (NN) peak heights for four CGA glasses, and the crystalline reference are shown in Table III. The PDF plots for all of the CGA glasses were very similar with the individual peaks being located within $\pm 0.1 \text{ \AA}$ of each other. The trend is that the NN distances increased slightly from 0.45 to 0.65 Ge for four measurable NN peaks. However, at 0.85 Ge, the NN distances decreased below the value for 0.45 Ge for the first 3 NN peaks but increased steadily at the fourth NN peak. Overall, the PDF's show that the amorphous CGA glasses have a high degree of short range order out to the third NN. In comparison to the computed PDF plot for the crystalline reference, the $G(r)$ plot for the amorphous CGA was shifted to the right, had shorter NN distances, broader peaks, and lost coherency after the third NN at 6.3 \AA .

The PDF computed from the crystal structure model of CdGeAs_2 consisted of four prominent peaks with a shoulder on the third one. Peak assignments were based on measurements

Table III. Summary of Atomic Pair Distribution Data for CdGe_xAs_2

Ge:Cd ratio	First NN	Second NN	Third NN	Fourth NN
0.45	2.56	4.09	6.34	7.45
0.65	2.57	4.10	6.40	7.49
0.85	2.55	4.06	6.32	7.51
1.0	2.56	4.10	6.36	7.46
CdGeAs_2 reference	2.53	4.35	6.32 [†] /7.23	8.54

[†]Shoulder on the third prominent peak. NN, nearest neighbor.

made of the crystal structure model of CdGeAs_2 (as published by Marenkin³⁵) using the computer program "CrystalMaker" ©. The first peak was located at 2.52 Å and was attributed to the convolution of the As–Ge and As–Cd bonds at 2.425 and 2.633 Å, respectively.^{14,28} The second peak was at 4.35 Å and was assigned to As–As second NN at distances of 4.219 and 4.459 Å. Atom pair distances between Cd–As and Ge–As exist at 6.33 and 6.35 Å, thus the shoulder in the crystalline PDF at 6.32 Å was assigned to these atom pairs. The third prominent peak in the crystalline PDF was located at 7.23 Å and was assigned to As–As atom pairs, since several As–As atom pair distances were measured at 7.14, 7.43, and 7.91 Å. The fourth peak was located at 8.64 Å and most likely corresponds to several different atom pairs (Cd–Cd, Ge–Ge, and As–As) that all occur at 8.402 Å in the crystal model.

The first peak of $G(r)$ for the CGA glasses was located at 2.56 Å and was at a slightly farther distance than in the crystal PDF. The farther NN distance in the CGA glass is probably due to the fact that most of the glasses have a lower Ge content than the crystal, thus causing a slight peak shift toward the longer As–Cd bond distance of 2.633 Å. The second NN peak was located at approximately 4.09 Å for the amorphous $G(r)$, and its position was 5.6% shorter than the second NN distance for the crystalline specimen. These peaks were assigned to As–As second NN distances as was the same for the perfect crystal. The higher relative intensity of this peak is consistent with the fact that these compounds contain at least 50% As. Additional corroborating data are needed to make a definitive assignment of specific atom pairs to the PDF peaks in the amorphous CGA glasses beyond the second NN. For example, it is not clear whether the third peak in the amorphous PDF at 6.35 Å corresponds to the shoulder in the crystalline PDF at the same location (e.g., Cd–As and Ge–As atom pairs), or to the prominent third peak due to As–As atom pairs located almost an angstrom farther away, or possibly the convolution of other possible atom pairs. Because the glasses contain at least 50% As, and since the amorphous PDF peak at 4.09 Å was shifted to the right, the third peak in the amorphous PDF may be due to As–As atom pairs, but a peak shift of approximately 0.88 Å seems unusually large. The fourth peak for the amorphous specimens occurred from 7.4–7.5 Å, and was very diffuse. Again, definitive assignment of this peak was not possible. Several As–As atom pair distances in the single crystal structure at 7.14, 7.43, and 7.91 Å, so this peak may be due to a convolution of those atom pairs.

The macroscopic bulk densities (g/cm^3) of the samples were measured using He pycnometry and were found to vary as a function of Ge content, processing method, and structure (i.e., crystal vs. amorphous); see Fig. 4. The density for crystalline

compounds decreases going from 5.86 g/cm^3 for CdAs_2 to 5.62 g/cm^3 for CdGeAs_2 (a pseudo trend-line was drawn as a guide to the eye).^{12,35,36} A similar variation in density with Ge content was observed for the amorphous specimens fabricated in this study, however, the amorphous compounds were approximately 2% more dense than their crystalline counterpart at $x = 1.0$. This was consistent with data reported elsewhere.^{12,14} The shift in NN distances to shorter values as observed in the amorphous PDF (Fig. 3(B)) also illustrates this relationship. The variation in density with phase was important to note while interpreting failed experiments, so as to make appropriate processing adjustments. Density variations with processing method indicated that the DC-quenched specimens were slightly denser than the LG-quenched specimens. Because the amorphous phase was denser than the crystalline phase, the higher density may have been due to the additional constraint imposed by the annular Cu ring in the DC ampoule, or it may be an indication that the DC quench method was slightly faster than the LG method. Although the macroscopic bulk density decreases with increasing Ge content, it is important to point out that the atomic density (atoms/cm^3) increases with Ge content. This is explained by the change in average atomic mass and in covalent or atomic radius of the atoms as the alloy changes composition.

The electronic structure of crystalline semiconductors is modeled as having a distinct conduction and valence band edge with a well-defined band gap. Amorphous semiconductors typically exhibit bands of extended states with band edges similar to those of the crystalline materials combined with increasingly localized states below the band edge whose density decays exponentially with energy away from the band edge. The exponentially decaying density of states is referred to as a band tail. Finally, there are isolated states in the energy gap (properly the mobility gap), which give rise to a typically constant density of states. The optical absorption coefficient of the material reflects the product of the density of states in the valence and conduction bands. Therefore, the absorption coefficient typically shows a quadratic decrease near the energy separating the two sets of extended states, an exponentially decaying behavior resulting from the band tails, and a constant absorption for energies where only isolated defect states occur.

Optical absorption spectroscopy and ellipsometry were used to characterize the transition from the band edge toward the middle of the mobility gap. At energies higher than the band edge, the material is relatively opaque, and the optical absorption coefficient becomes very large. Therefore a simple transmission/reflection model will not work. Ellipsometry, however, provides a measure of the absorption coefficient out to much lower transmission values. Toward the middle of the mobility gap, the material is more transparent and optical transmission measurements suffice. The greater the density of defect states in the material, the more gradual the transition will be from the mobility edge to the mobility gap, and the higher the absorption coefficient will be in the gap region. Consequently, improved electrical conduction properties depend on minimizing the density of defect states. Ideally the material should be characterized by (1) a steep slope of the absorption coefficient curve at the mobility edge and (2) minimizing the low-energy absorption coefficient. The effects of composition and processing conditions on the density of defect states was thus evaluated.

Optical absorption coefficient measurement results for a variety of CGA glasses and processing methods are shown in Fig. 5 and combined optical absorption and ellipsometry results are given in Fig. 6. The effect of composition on the density of defect states was evaluated for both the DC and the LG quench methods. The variation for both processing methods was similar, increasing the Ge content resulted in a reduced optical absorption coefficient (Figs. 5(A) and (B)). There was about a 50% reduction in the absorption coefficient upon changing the Ge content from $x = 0.45$ –0.85 Ge for the DC process, whereas for the LG process, there was over a factor of 4 reduction in the absorption coefficient for changing the Ge content from 0.65 to 1.0.

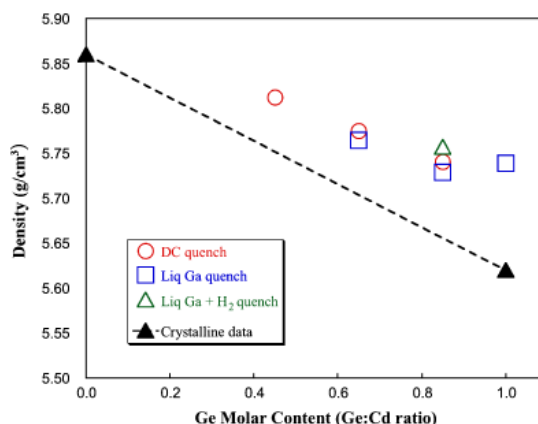


Fig. 4. Variation in bulk density with composition (x), phase, and process method for CdGe_xAs_2 glasses.

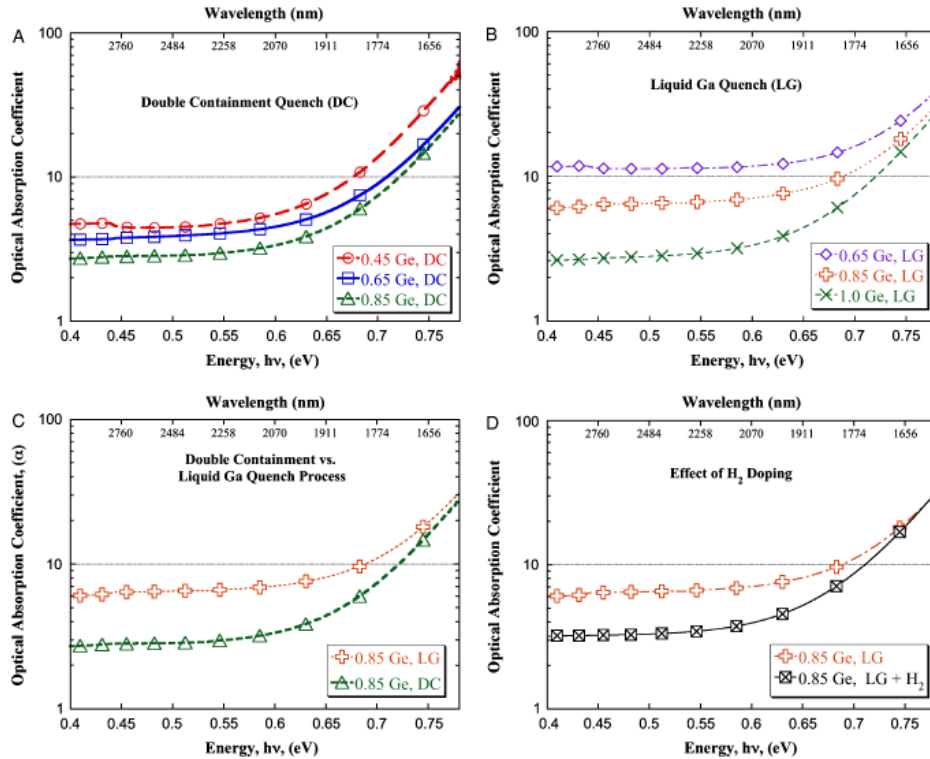


Fig. 5. Absorption coefficient data for CGA glasses showing effects of composition (A) and (B), processing method (C) and hydrogen doping (D).

The effect of processing method (DC vs LG) on the density of defect states was also evaluated. Two different Ge compositions were selected (0.65 and 0.85 Ge), and ingots were made from each composition using both of the processing methods. Optical absorption coefficients were measured as a function of energy for samples taken from each ingot, and the results for 0.85 Ge are shown in Fig. 5(C). For both compositions the results were the same; the DC quench process yielded a lower optical absorption coefficient curve than the LG quench process. For a composition of 0.65 Ge, the DC process resulted in approximately a threefold reduction in the absorption coefficient from

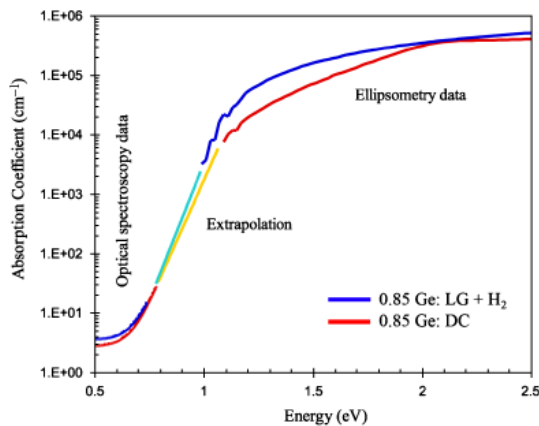


Fig. 6. Combined ellipsometry, optical transmission and reflection data. For the thick samples studied here there is a range of absorption coefficients that are too low for ellipsometry and too high for absorption measurements.

the maximum value measurable to the constant value far below the absorption edge. For the 0.85 Ge composition, the absorption coefficient data were lower by over a factor of two in the gap compared with the highest measurable value. The results were similar for samples thinned as much as the mechanical properties of the material would permit.

Reducing the density of defect states in amorphous semiconductors is a common concern. Amorphous silicon (a-Si) is one of the most prevalent amorphous semiconductors and is widely used in photovoltaic applications. One strategy used to reduce the density of defect states in a-Si is to dope it with hydrogen during thin film deposition. The hydrogen acts to passivate dangling bonds. Because CGA glass is a tetrahedrally bonded material just like a-Si, hydrogen doping (as described in the experimental section) was evaluated to determine if it could have a similar positive effect on reducing the density of defect sites. A comparison was made between two different specimens, both having the same composition (0.85 Ge) and both processed in the same method (LG), but one was doped with hydrogen. The optical absorption coefficient measurement results are shown in Fig. 5(D). Hydrogen doping was able to reduce the absorption coefficient values in the midgap energy range by almost a factor of two.

The results of the optical absorption data indicates that it is possible to reduce the density of defect states in CGA glass both near the mobility edge as well as in the middle of the mobility gap. This can be achieved by controlling composition, processing conditions, and by doping the material with hydrogen.

Hall conductivity measurements as a function of temperature were made on several different CGA glasses. In general, the Hall conductivity trends paralleled those of the absorption coefficient data: specimens with lower optical absorption coefficients had lower Hall conductivity values. Increasing Ge content resulted in lower conductivity and DC-quenched specimens had lower conductivity values than LG-quenched specimens with the same

Ge content. Room temperature conductivity values for DC quenched CGA ranged from $9.1 \times 10^{-7} \Omega/\text{cm}$ for 0.45 Ge to $1.1 \times 10^{-7} \Omega/\text{cm}$ for 0.85 Ge. However, hydrogen doping did not appear to have a significant effect on the electrical transport properties, as there was very little difference in conductivity values for doped and undoped LG-quenched CGA glasses of the same composition.

In summary, with increasing Ge content, the following trends were observed: optical absorption coefficients decreased; Hall conductivity decreased; bulk density decreased; atomic density increased; and NN distances increased. Hence it appears that increasing Ge content modifies CGA glasses by creating a more open structure, making electrical conduction more difficult (assuming a hopping conduction mode) and subsequently decreasing the density of states at the edges and middle of the conduction band.

IV. Conclusions

Two different methods for synthesizing bulk, crack-free ingots of CGA glass were developed. The use of pyrolytic coatings lining the process ampoules was dismissed due to problems associated with reduced ingot yield, contamination of the melt by the coating, and degradation of the resulting electrical properties. Stoichiometry control, homogeneity, and minimal trace elemental contamination of the synthesized ingots validated the ability of both processes to yield good quality, high-purity amorphous materials. PDF analysis of CGA glasses showed that they retained NN atomic coherency out to the third NN. The PDF peaks were broader and located at shorter distances than in the crystal, but tended to increase in distance with Ge content. Composition-property and processing-property relationships were demonstrated using optical absorption spectroscopy and Hall conductivity. The results indicate that the density of defect states in the material near the band edges and in the middle of the mobility gap can be reduced three different ways: (1) by increasing the Ge concentration, (2) using the DC quench process, and (3) by doping with hydrogen. The variation in properties with composition was attributed to the effect of Ge on the short-range order in the material. Thus, we have been able to demonstrate broad control of semiconductor properties for Cd-Ge-As glasses by manipulating composition and processing parameters, and have been able to achieve an increase in room temperature resistivity over an order of magnitude greater than previously reported.

Acknowledgments

The authors would like to acknowledge the contributions of Xiangyun Qiu for his consultation on how to performing PDF analysis. We would also like to acknowledge Randall Scheele and Anne Kozeliski from PNNL for their assistance in collecting the thermal analysis data. Additionally, the following Department of Energy sponsored facilities are acknowledged, as portions of this research were performed in them: The Environmental Molecular Synthesis Laboratory, located at PNNL, and the Materials Research Laboratory, located at the University of Illinois at Urbana-Champaign.

References

1. J. Mort, *The Anatomy of Xerography*. McFarland, London, 1989.
2. A. Luque and S. Hegedus, *Handbook of Photovoltaic Science and Engineering*. John Wiley and Sons Ltd., Chichester, West Sussex, England, 2003.
3. M. Hoheisel and L. Batz, "Requirements on Amorphous Semiconductors for Medical X-Ray Detectors," *J. Non-Cryst. Solids*, **266–269** [Part B] 1152–7 (2000).
4. S. Kasap, J. Rowlands, K. Tanioka, and A. Nathan, "Applications of Disordered Semiconductors in Modern Electronics: Selected Examples"; pp. 149–77 in *Charge Transport in Disordered Solids with Applications in Electronics*, Edited by B. Sergei, John Wiley and Sons Ltd., Hoboken, NJ, 2006.
5. G. F. Knoll, *Radiation Detection and Measurement*, 3rd edition, Wiley, New York, 2000.
6. A. Owens and A. Peacock, "Compound Semiconductor Radiation Detectors," *Nucl. Instrum. Methods Phys. Res. Sect. A*, **531** [1–2] 18–37 (2004).
7. P. G. Schunemann, K. L. Schepler, and P. A. Budni, "Nonlinear Frequency Conversion Performance of AgGaSe₂, ZnGeP₂, and CdGeAs₂," *MRS Bull.*, **23** [7] 45–9 (1998).
8. E. Tanaka and K. Kato, "Second-Harmonic and Sum-Frequency Generation in CdGeAs₂," p. 475. *Infrared Applications of Semiconductors II. Symposium*, December 1–4, Boston, MA, 1997.
9. P. Zapol, R. Pandey, M. Seel, J. M. Reio, and M. C. Ohmer, "Density Functional Study of the Structure, Thermodynamics and Electronic Properties of CdGeAs₂," *J. Phys. Condens. Matter*, **11** [23] 4517–26 (1999).
10. V. Rud, Y. Rud, I. Poluushina, T. Ushakova, and S. Iida, "Observation of Record Electron Hall Mobility in CdGeAs₂ Single Crystals," *Jpn. J. Appl. Phys.*, **39** [Suppl. 39–1] 266–7 (2000).
11. B. R. Johnson, J. V. Crum, S. K. Sundaram, R. M. V. Ginhoven, C. Seifert, B. J. Riley, and J. V. Ryan, "DC Ionization Conductivity of Amorphous Semiconductors for Radiation Detection Applications," *IEEE Trans. Nucl. Sci.*, (2009), in press.
12. L. Cervinka, R. Hosemann, and W. Vogel, "Relations Between the Structure of Crystalline and Amorphous CdGe_xAs_{2-x}," *J. Non-Cryst. Solids*, **3** [3] 294–304 (1970).
13. L. Cervinka, A. Hruby, M. Matyas, T. Simecek, J. Skacha, L. Stourac, J. Tauc, V. Vorlicek, and P. Höschl, "The Structure and Electronic Properties of Semiconducting Glasses Based on CdAs₂," *J. Non-Cryst. Solids*, **4**, 258–71 (1970).
14. K. S. Hong, Y. Berta, and R. F. Speyer, "Glass-Crystal Transition in II–IV–V₂ Semiconducting Compounds," *J. Am. Ceram. Soc.*, **73** [5] 1351–59 (1990).
15. A. Hruby and L. Stourac, "Semiconducting Glasses Based on CdAs₂," *Mater. Res. Bull.*, **4** [10] 745–56 (1969).
16. S. H. Risbud, "Processing and Properties of Some II–IV–V₂ Amorphous and Crystalline Semiconductors," *Appl. Phys. A Mater. Sci. Process.*, **62** [6] 519–23 (1996).
17. S. Sharma, K. S. Hong, and R. F. Speyer, "Glass Formation in Chalcopyrite Structured Semiconducting Compounds," *J. Mater. Sci. Lett.*, **8** [8] 950–4 (1989).
18. S. Sharma and R. F. Speyer, "Optimization of Quench Rate in the Fabrication of Bulk Chalcopyrite Glasses in Fused Silica Tubes," *J. Mater. Sci. Lett.*, **8** [3] 287–90 (1989).
19. A. Hruby, "The Nature of Glass-Forming Tendency in Cd–As System," *Czech. J. Phys.*, **26**, 593–8 (1976).
20. A. Giridhar and S. Mahadevan, "DC Electrical Conductivity of Some Cd–Ge–As Glasses," *Bull. Mater. Sci.*, **12** [2] 107–15 (1989).
21. W. Kern and D. A. Puotinen, "Cleaning Solutions Based on Hydrogen Peroxide for Use in Silicon Semiconductors," *RCA Rev.*, **31**, 186–206 (1970).
22. B. J. Riley, B. R. Johnson, S. K. Sundaram, M. H. Engelhard, R. E. Williford, and J. D. Olmstead, "Pressure–Temperature Dependence of Nanowire Formation in the Arsenic–Sulfur System," *Phys. Chem. Glass*, **47** [6] 675–80 (2006).
23. D. R. Lide, *CRC Handbook of Chemistry and Physics, Internet Version 2007*, 87th edition, Taylor and Francis, Boca Raton, FL, 2007.
24. T. B. Massalski, J. L. Murray, L. H. Bennett, and H. Baker, *Binary Alloy Phase Diagrams*, Vol. 1. American Society for Metals, Metals Park, OH, 1986.
25. M. J. Harrison, A. P. Graebner, W. J. McNeil, and D. S. McGregor, "Carbon Coating of Fused Silica Ampoules," *J. Cryst. Growth*, **290** [2] 597–601 (2006).
26. B. R. Johnson, M. J. Schweiger, and S. K. Sundaram, "Chalcogenide Nanowires by Evaporation–Condensation," *J. Non-Cryst. Solids*, **351**, 1410–6 (2005).
27. A. Hruby and L. Stourac, "Glass Forming Ability And Electrical Properties Of Semiconducting As_xTe_{1-x} Glasses," *Czech. J. Phys.*, **B 24** [10] 1132–8 (1974).
28. A. Hruby, "Evaluation of Glass-Forming Tendency by DTA," *Czech. J. Phys.*, **B22**, 1187–93 (1972).
29. V. D. Okunev, Y. I. Otman, and A. G. Yurov, "Properties of Amorphous CdGeAs₂ Films Obtained by Cathode Sputtering," *Sov. Phys. J.*, **22** [12] 1328–31 (1979).
30. V. D. Okunev and N. N. Pafomov, "Electrical Activity of Ni in Glassy CdGeAs₂," *Soviet Physics – Semiconductors*, **22** [3] 302–3 (1988).
31. I. Kaban, P. Jovari, and W. Hoyer, "Partial Pair Correlation Functions of Amorphous and Liquid Ge₁₅Te₈₅," *J. Optoelect. Adv. Mater.*, **7** [4] 1977–81 (2005).
32. A. Pasewicz, D. Idziak, J. Koloczek, P. Kus, R. Wrzalik, T. Fennell, V. Honkimäki, A. Ratuszna, and A. Burian, "Pari Correlatin Function Analysis of 5-(4-hexadecyloxyphenyl)-10,15,20-tri(4-pyridyl)porphyrin and 5-(4-methoxy-carbonylphenyl)-10,15,20-tri(4-pyridyl)porphyrin," *J. Mol. Struct.*, **875**, 167–72 (2008).
33. T. Proffen, S. J. L. Billinge, T. Egami, and D. Louca, "Structural Analysis of Complex Materials Using the Atomic Pair Distribution Function—A Practical Guide," *Z. Kristallogr.*, **218**, 132–43 (2003).
34. X. Qui, J. W. Thompson, and S. J. L. Billinge, "PDFgetX2: A GUI Driven Program to Obtain the Pair Distribution Function from X-Ray Powder Diffraction Data," *J. Appl. Cryst.*, **37**, 678–78 (2004).
35. F. Marenkin, V. M. Novotortsev, K. K. Palkina, S. G. Mikhailov, and V. T. Kalinnikov, "Preparation and Structure of CdGeAs₂ Crystals," *Inorg. Mater.*, **40** [2] 93 (2004).
36. L. Cervinka and A. Hruby, "The Crystal Structure of CdAs₂," *Acta Crystallogr. Sect. B*, **B26**, 457–8 (1970). □

DC Ionization Conductivity of Amorphous Semiconductors for Radiation Detection Applications

Bradley R. Johnson, *Member, IEEE*, Jarrod V. Crum, S. K. Sundaram, Renee M. Van Ginhoven, *Member, IEEE*, Carolyn E. Seifert, *Member, IEEE*, Brian J. Riley, and Joseph V. Ryan

Abstract—DC ionization conductivity measurements were used to characterize the electrical response of amorphous semiconductors to ionizing radiation. Two different glass systems were examined: a chalcopyrite glass (CdGe_xAs_2 ; for $x = 0.45 - 1.0$) with a tetrahedrally coordinated structure and a chalcogenide glass ($\text{As}_{40}\text{Se}_{(60-x)}\text{Te}_x$; where $x = 0-12$), with a layered or three dimensionally networked structure, depending on Te content. Changes in DC ionization current were measured as a function of the type of radiation (α or γ), dose rate, applied field, specimen thickness and temperature. The greatest DC ionization response was measured with $\text{CdGe}_{0.85}\text{As}_2$ at -40°C from an alpha source (which is the first reported result for radiation response from an amorphous chalcopyrite semiconductor). Avalanche gain was observed in $\text{As}_{40}\text{Se}_{60}$ with exposure to alpha radiation at fields $\geq 7 \times 10^3$ V/cm. These results demonstrate the potential of these materials for radiation detection applications.

Index Terms—Amorphous semiconductors, arsenic tri-selenide As_2Se_3 DC ionization, cadmium germanium di-arsenide, CdGeAs_2 .

I. INTRODUCTION

FOR room temperature radiation detection, a semiconductor detector material should have acceptable carrier mobilities and lifetimes, moderate band-gaps (e.g., > 1.1 eV), a large absorptive cross-section for interacting with the radiation, and ideally would be easily synthesizable in large shapes at low cost. Single element, single crystal semiconductors such as Si and Ge have excellent charge carrier mobilities and lifetimes; however, due to their small band gaps, cryogenic cooling is often necessary (depending on the type of detector) to reduce thermally generated leakage currents below the signal level induced by ionizing radiation. The other option to reduce the effects of thermally generated leakage currents is to use materials with larger band gaps. This necessitates the use of compound (binary, ternary, etc.) semiconductors such as CdZnTe (CZT), AlSb , HgI , etc. However, growing pure, defect-free single crystal compound semiconductors that meet the geometrical and performance requirements for radiation detector applications is a challenging processing problem with many obstacles

Manuscript received July 12, 2008; revised November 24, 2008. Current version published June 10, 2009. This work was supported in part by the Department of Energy, National Nuclear Security Administration, Office of Defense Nuclear Nonproliferation, Office of Nonproliferation Research and Development (NA-22). PNNL is operated for the U.S. Department of Energy by Battelle Memorial Institute under Contract DE-AC06-76RLO 1830.

The authors are with the Pacific Northwest National Laboratory, 790 6th Street, Richland, WA 99354 USA (e-mail: Bradley.Johnson@pnl.gov).

Digital Object Identifier 10.1109/TNS.2009.2013344

that have not yet been fully resolved. Consequently, a program of research was initiated to examine the feasibility of using amorphous semiconductors as the active sensing medium for radiation detection applications. Two different families of amorphous semiconductors were selected, a chalcopyrite glass family, CdGe_xAs_2 (CGA) and a chalcogenide glass family, $\text{As}_{40}\text{Se}_{(60-x)}\text{Te}_x$.

Amorphous materials provide several processing advantages compared to single crystal materials. These include faster synthesis routes (hours/days vs. weeks to grow an ingot), custom shape casting or molding, and the ability to deposit them in large areas as homogeneous thin films. Additionally, they have broader compositional flexibility, are less sensitive to trace impurities, and their properties can be tailored (within limits) to meet specific application needs by controlling processing, compositional, and doping variables. Their main liability, however, is that they typically have poorer charge carrier transport properties than single crystal semiconductors. This is due to a high density of localized electronic states near the band edges, which is a natural consequence of their disordered structure.

Conduction in amorphous and disordered semiconductors has been extensively studied [1]. Much of the early work in the area of semiconductor theory for amorphous materials was pioneered by Mott [2]–[5]. Although considerable emphasis had been placed on studying doped and hydrogenated amorphous silicon [6]–[8], the principles of semiconduction in amorphous materials have been applied to chalcogenide and chalcopyrite glasses as well [9], [10].

To summarize, the concepts of a conduction and a valence band with an energy (mobility) gap separating them are applicable to amorphous semiconductors just as they are for crystalline semiconductors. The main distinction is that their inherent long-range structural disorder results in a localization of the electronic states at the edges of the conduction and valence bands and in some instances within the mobility gap as well. The presence of these localized states necessitates that charge carriers hop from one state to an adjacent state as they move through the material. This tends to impede the transport kinetics across the mobility gap and at the edges until the carrier reaches the extended states [10]. The net result is that charge carrier transport is impeded.

Notwithstanding, these materials have been shown to have some unique electrical properties that occur at high fields such as non-destructive switching, reversible memory and avalanche gain as well as a variety of photo-induced phenomena [11]–[13]. In many chalcogenide glasses (e.g., Se , As_2Se_3 , GeSe_2 , and their sulfur analogs), these unique properties can be correlated

to the presence of non-bonded valence pair electrons [14]. Apparently, the application of high fields to these materials is able to create a large population of carriers above the Fermi level that can subsequently be promoted above their mobility edges by thermal excitation [15].

Gamma-radiation induced effects in chalcogenides have been studied since the 1980s [16]–[25]. One notable phenomenon is physical ageing [17] at high doses for As-Se chalcogenide glasses under ^{60}Co γ -irradiation, which was analyzed using a differential scanning calorimetry (DSC) instrument. An increase in glass transition temperature and the area of an endothermic peak near the glass transition region for Se-enriched glasses have been associated with additional γ -activated structural relaxation of the glass network towards thermodynamic equilibrium as a supercooled liquid [19]. Transient radiation effects have also been reported in amorphous chalcogenide semiconductors. For instance, gamma-ray induced conductivity had been demonstrated for some As-Se-Te glasses, and x-ray induced photoconductivity was shown for As-Se-Tl glass [26], [27].

Because of their unique properties, amorphous semiconductors have been successfully applied in a number of applications such as direct conversion digital x-ray image detectors [28], x-ray photoconductors [12], [29], dosimeters [30], photovoltaics [31], [32], phase change memory storage devices and photocopiers [33], [34]. However, they have not been widely developed for radiation detection applications. This study is an initial investigation to evaluate radiation response properties of selected amorphous semiconductors from two different glass structure systems.

Radiation detection depends not only on materials performance, but also on the electrical engineering and signal processing involved with extracting and processing the electrical response of the material. Since each material will have different charge carrier dynamics and transport properties, it is not necessarily possible to simply insert a new material into an existing detector assembly and evaluate its performance. Thus, ideally, there would be a technique that could be used to efficiently screen the performance of new materials. In light of this need, Derenzo and coworkers [35] developed an apparatus for confining powder samples under pressure in an electric field and measuring the DC current induced by a 450 Ci, 1.2 MeV ^{60}Co gamma (γ) source at a dose rate of 1,500 rad/min. This approach has been adapted to screen and evaluate bulk amorphous semiconductors for their potential application as radiation detection materials.

We have extended the argument originally developed by Derenzo and coworkers [35] for crystalline semiconductor powders to bulk amorphous semiconductors. Similar to polycrystalline semiconductor powders, trapping, detrapping and retrapping are expected to occur in amorphous semiconductors as the moving charge carriers interact with structural disorders, impurities, and defects. This will add to the effective carrier lifetime, τ . Nonetheless, many of the carriers will ultimately recombine in the material, and will not traverse the complete distance between the electrodes. Thus, the average drift distance between trapping and recombination (d') will be much less than the distance between electrodes (d). Potentially shorter

recombination distances raise concerns about charge collection in these compounds. The DC ionization experiment described below provides an initial view into the charge carrier transport mechanisms in amorphous semiconducting materials, and enables a straightforward means of comparing the performance of various compounds.

II. EXPERIMENTAL PROCEDURES

A. Specimen Synthesis

Bulk amorphous semiconductor specimens were synthesized from high-purity elements (99.999 + %; Alpha-Aesar) in the specified stoichiometric ratios. All elements were stored and batched in a nitrogen-purged, atmosphere controlled glove box (M.Braun Inc.) where water and oxygen levels were maintained at < 0.1 ppm. Reaction vessels (ampoules) were made from 1-mm thick fused quartz tubing with either 10 or 25 mm inside diameters (GE214, GM Associates, Inc.). They were prepared by sealing one end of a ~ 30 cm long tube with an oxygen-propane torch. Each tube was cleaned using a RCA1 etch where the tubes were filled with a solution of $\text{NH}_4\text{OH} : \text{H}_2\text{O}_2$:de-ionized water (DIW) at a 1:1:5 ratio by volume and set in a 70°C oven for 2 hours [36]. The tubes were rinsed with DIW and then etched in a 5% HF solution at room temperature for 2 hours [37]; the tubes were rinsed again with DIW and then were baked out and annealed at 1160°C inside of a box furnace located within the atmosphere controlled glovebox.

Stoichiometric quantities of the elemental constituents were weighed out to ± 0.1 mg accuracy and loaded into the ampoules. Each batch contained $\sim 12 - 15$ g of raw elements so as to yield an ingot with a 10 mm diameter that was 30–40 mm tall. Detailed information regarding synthesis and process steps to batch and seal the ampoules are provided elsewhere [38], [39].

Once constructed, the ampoules were attached to a holder and loaded into the containment assembly of a custom designed rocking furnace. Specimens were thermally processed by slowly heating them up in the rocking furnace up to 850°C and rocked for 24 h. After thermal processing, the rocking motion was turned off to allow the liquid to settle to the bottom of the ampoule. The furnace temperature was then reduced to in preparation for quenching (varied with composition). Then the ampoules were quickly extracted from the furnace and quenched in water so as to vitrify the liquid and prevent crystallization. After quenching, the ingots were annealed at $\sim 10 - 50^\circ\text{C}$ less than T_g for that composition (as determined by thermal analysis experiments and extrapolation from literature data) for ~ 8 hours to aid in reducing thermally-induced stress in the glasses. After cooling, the ingots were cast into an acrylic resin (Buehler VariKleer[®]), sectioned into 1–3 mm thick wafers, and polished.

B. DC Ionization Measurements

After polishing the specimens, electrodes were applied using a shadow mask and a vapor deposition process. A variety of different electrodes such as evaporated carbon, sputtered Pd, and sputtered Au/Pd were evaluated. Some experiments were done without electrodes, per se, and direct electrical contact was made to the specimen using either conductive rubber or

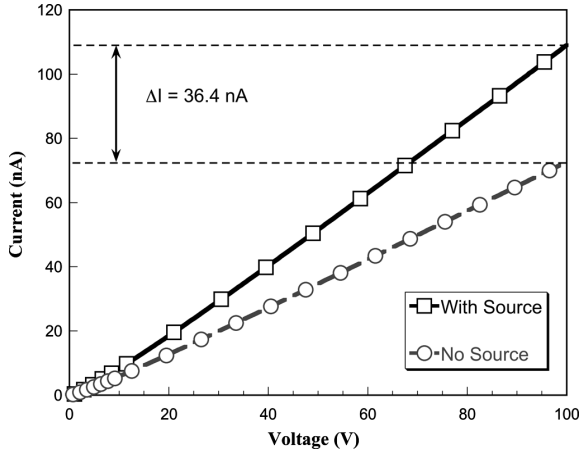


Fig. 1. Current-voltage curve for $\text{CdGe}_{0.85}\text{As}_2$ glass at -40°C , with and without exposure to a $3.9 \text{ mCi } ^{238}\text{Pu}$ α source.

conductive, adhesive carbon tape. The different types of electrodes were evaluated by measuring their current-voltage (I-V) response curves. All of the electrodes analyzed showed an ohmic response, with only nominal differences in performance between them. The specimens were then placed in a sample holder, and electrical contact was made to the electrodes using either conductive tape, silver epoxy or spring loaded metal pins.

Bias voltages were applied to the specimens using source measurement unit (SMU, e.g., either a Keithley 237, 6430, or 617, depending on the experiment). These devices were capable of simultaneously sourcing voltage, and measuring current. For a given bias voltage, the current flowing through the device was measured with and without exposure to a sealed radiation source. The difference between current readings was called the DC ionization current, ΔI . Alpha (α) radiation response measurements were made using a $3.9 \text{ mCi } ^{238}\text{Pu}$ source and γ radiation response measurements were made with a $20 \text{ Ci } ^{137}\text{Cs}$ sealed source. The dose rate from the γ source was varied by controlling the source-specimen separation distance. Due to equipment availability limitations, and specimen-specific testing requirements, a variety of different experimental configurations were used.

Detector gain was calculated according to (1) [33], [34].

$$\%DG = \frac{(V \bullet \Delta I)}{(A \bullet E)} \quad (1)$$

where $\%DG$ is the percentage of detector gain, V is the bias voltage, ΔI is the DC ionization current, A is the activity of the source in decays per second, and E is the average energy of the α particle at the face of the detector as compensated for attenuation through air and the foil seal. Note that this is a simple ratio of the electrical power readout ($V \bullet \Delta I$) from the source measuring unit as compared to the power (J/s) deposited onto the face of the detector element by the alpha source.

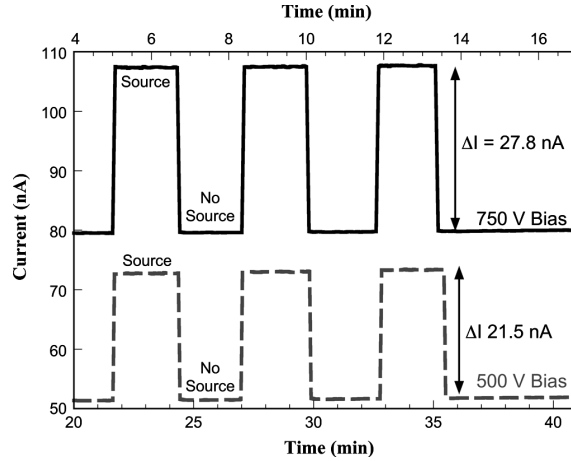


Fig. 2. DC ionization current response for $\text{As}_{40}\text{Se}_{48}\text{Te}_{12}$ from exposure to a $3.9 \text{ mCi } ^{238}\text{Pu}$ α -source.

III. RESULTS

A. $\text{CdGe}_{0.45}\text{As}_2$

Current-voltage curves up to a bias voltage of 100 V were collected from a 2.3 mm thick specimen of CGA glass with surface contacts at -40°C with and without exposure to the α source (Fig. 1). It was necessary to cool the detector due to high leakage currents at room temperature. Direct electrical contact (without electrodes) was made to the specimen using silver epoxy and conductive, adhesive carbon tape. Both contacts were applied to the front face of the specimen. A digital data acquisition system was used to control the voltage ramp rate and record the I-V data at each point. The same ramp rate profile was used for both measurements. A net DC ionization current of 36.4 nA was measured at 100 V. This represented approximately a 50% increase in conduction compared to the dark current.

B. $\text{As}_{40}\text{Se}_{48}\text{Te}_{12}$

Additional DC ionization experiments were done with a 3.44 mm thick vitreous specimen of As-Se-Te (Fig. 2). Direct electrical contact was made to the specimen using conductive, adhesive carbon tape. Experiments were done with both electrodes on the front face of the specimen, as well as with electrodes on opposing faces. Measurements were made at room temperature at two different bias voltages: 500 and 750 V. A movable shutter was placed between the specimen and the sealed α source and the specimen was biased up to the specified voltage. The IV data was logged using a computer controlled data acquisition system. While under bias, the shutter was manually moved to expose the specimen to the source, and the corresponding change in current was recorded. At 500 V, the DC ionization current was 21.5 nA, while at 750 V, the ionization current was 27.8 nA. This represented a current increase of 41.8% and 34.9%, respectively.

C. $\text{As}_{40}\text{Se}_{60}$

Results from DC ionization experiments on $\text{As}_{40}\text{Se}_{60}$ chalcogenide glass conducted with a sealed α source are shown in

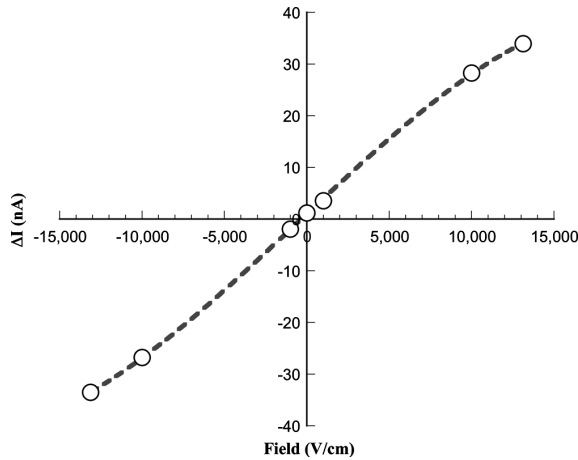


Fig. 3. Variation in DC ionization current with applied bias voltage for $\text{As}_{40}\text{Se}_{60}$ from exposure to a 3.9 mCi ^{238}Pu α -source.

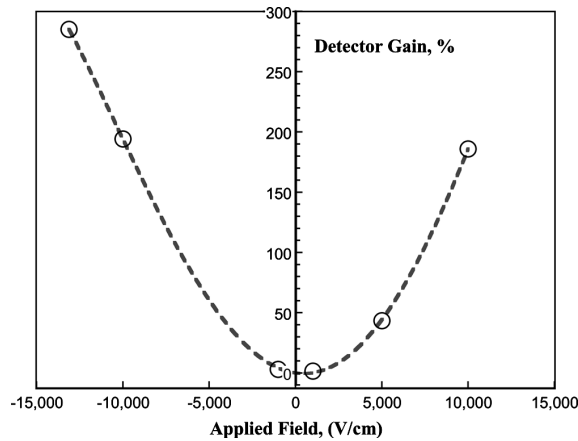


Fig. 4. Detector gain as a function of applied field for $\text{As}_{40}\text{Se}_{60}$ from exposure to 3.9 mCi ^{238}Pu α -source.

Figs. 3 and 4. The specimen was 838 μm thick. Measurements were made through the bulk of the specimen (contacts on opposite faces of the specimen) both with and without evaporated planar carbon electrodes (negligible difference was observed with and without electrodes). Electrical contact was made using conductive, adhesive carbon tape. Measurements were made at room temperature at a variety of different bias voltages using the same procedure as for the As-Se-Te specimen. The variation of the DC ionization current as a function of the applied field is shown in Fig. 3.

These data were used as per (1) to calculate the percentage of detector gain as a function of the applied field. The electric field was assumed to be uniform across the thickness of the sample. The results are shown in Fig. 4. There was a slight asymmetry in the data, with the negatively applied biases yielding a marginally greater response. At a field of -1.3×10^5 V/cm, the detector gain was approximately 280%. This means that the power output of the detector ($V \bullet \Delta I$) at this field was a factor of 2.8 greater than the power deposited into the specimen (activity \bullet

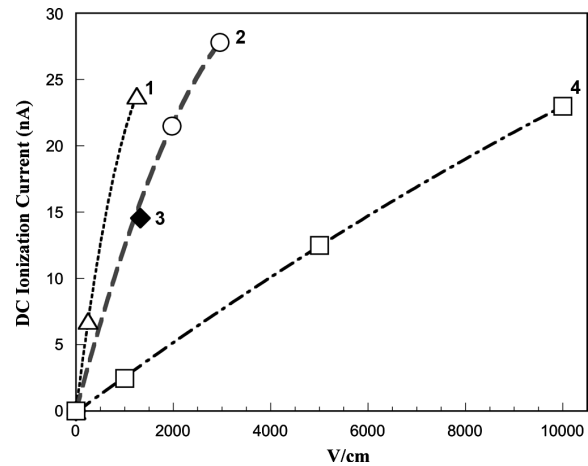


Fig. 5. Comparison of DC ionization response for various amorphous semiconductors from exposure to a 3.9 mCi ^{238}Pu α -source. (1 = $\text{CdGe}_{0.85}\text{As}_2$ front face contacts; 2 = $\text{As}_{40}\text{Se}_{48}\text{Te}_{12}$ front face contacts; 3 = $\text{As}_{40}\text{Se}_{48}\text{Te}_{12}$ opposite face contacts; 4 = $\text{As}_{40}\text{Se}_{60}$ opposite face contacts).

energy/decay) by the α source. The increase in detector gain as a function of applied field was an indication that the specimen was undergoing avalanche gain.

The relative performance of the three different specimens ($\text{CdGe}_{0.85}\text{As}_2$, $\text{As}_{40}\text{Se}_{48}\text{Te}_{12}$, and $\text{As}_{40}\text{Se}_{60}$) under exposure to the sealed alpha source is shown in Fig. 5. As determined by the different experimental apparatuses used, some measurements were done with both contacts applied to the front face of the specimen (1, 2), and for other measurements, the contacts were applied to opposing faces (3, 4).

DC ionization experiments were also conducted using a 20 Ci ^{137}Cs γ -source on $\text{As}_{40}\text{Se}_{60}$. The DC ionization current was measured through the bulk of the specimen as a function of the applied field, specimen thickness, and the dose rate. The data is plotted in Fig. 6. The DC ionization current was observed to increase with each of these variables: field strength, sample thickness, and dose rate.

IV. DISCUSSION

Three different amorphous semiconductors were evaluated from two different glass families, and each of them showed a measurable response to ionizing radiation from an α -source. The $\text{As}_{40}\text{Se}_{60}$ specimen showed a response to both α and γ radiation (the only one evaluated with a γ -source so far). The CGA glass specimen from the chalcopyrite family (which required modest cooling) was potentially the most sensitive material evaluated, showing a 50% increase in DC ionization current at only 100 V of bias (Fig. 1) and having the largest DC ionization response as a function of applied field (Fig. 5).

All of the specimens showed a prompt (e.g., < 1 s) response upon changing their exposure to the sealed source. This indicates that when the specimen was exposed to the source, the traps in the sample started to fill as the current increased sharply to a new equilibrium level. At this point, the rate of generation of electron-hole pairs was equal to the rate of trapping and recombination. When the shutter was placed between the α source

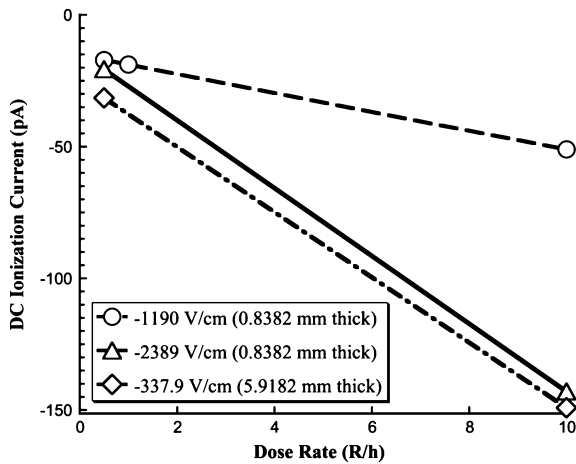


Fig. 6. Variation in DC ionization current with applied field, dose rate, and specimen thickness for $\text{As}_{40}\text{Se}_{60}$ from exposure to a 20 Ci ^{137}Cs γ source.

and the specimen, the current dropped sharply to the initial level as the charge carriers detrapped. Multiple cycles showed practically no drift in the baseline current level (Fig. 2).

Increasing the applied field resulted in an increase in the DC ionization current response. This was observed with exposure to both α and γ radiation (Fig. 3 through Fig. 6). The effect was such that trapped and lost charge carriers could not only be compensated for, but that additional charge carriers could also be generated. There are a couple of possible explanations for the observed behavior. With increasing field strength, the moving charge carriers might have sufficient momentum to escape low energy trap states that might otherwise capture them. It is also possible that with increasing field strength, once trapped charge carriers could be released from low energy trap states and participate in conduction process again. A third option is that at extreme fields, the moving charge carriers could be accelerated with sufficient momentum so as to be able to create additional electron-hole pairs through impact ionization as they encounter defects, trap sites, or stationary charge carriers. This appears to be the dominant mechanism at extreme fields as shown in the $\text{As}_{40}\text{Se}_{60}$ specimen exposed to the alpha source (Fig. 4). Impact ionization was able to create an avalanche of additional charge carriers that compensated for trapping losses at a field of 7.3×10^3 V/cm and subsequently created a detector gain of 280% at a field of 1.3×10^5 V/cm. Impact ionization induced avalanche has been reported in other amorphous semiconductors such as amorphous selenium [12], so this appears to be a reasonable explanation for the observed behavior. The transition between different charge carrier transport mechanisms may be difficult to determine experimentally, since the detector gain with applied field is a continuous, smooth curve. This is probably due to the fact that the density of defect states as a function of energy in these materials also tends to be fairly continuous.

The addition of Te to As-Se glass was shown to have a significant impact on its charge carrier transport properties. The DC ionization response for the $\text{As}_{40}\text{Se}_{48}\text{Te}_{12}$ glass was almost four times greater than that for $\text{As}_{40}\text{Se}_{60}$. This demonstrates the

significant role that chemistry plays in the performance of amorphous semiconductors, and indicates that potentially greater improvements are possible through optimized materials design.

Gamma radiation experiments on $\text{As}_{40}\text{Se}_{60}$ (Fig. 6) also showed that the DC ionization response varied with dose rate, which was anticipated with an increased flux of ionizing photons. The other important observation was that the DC ionization response also increased with specimen thickness. The same bias voltage was applied to two specimens with different thicknesses, thereby creating two different field densities. The thicker specimen with the lower electric field had the larger DC ionization response, thus illustrating the fact that detector efficiency increases with volume.

V. CONCLUSIONS

The experimental techniques explained in this paper for measuring the DC ionization currents proved to be a useful characterization tool for evaluating the radiation response of amorphous semiconductors. Both of the amorphous semiconductor families evaluated (chalcopyrite and chalcogenide) showed a measurable electrical response to ionizing radiation, thus demonstrating their potential use for radiation detector applications. The material with the strongest response to α -radiation was the $\text{CdGe}_{0.85}\text{As}_2$ glass specimen at -40°C . To the best of our knowledge, these are the first reported results of α -radiation induced conductivity in an amorphous chalcopyrite semiconductor. The $\text{As}_{40}\text{Se}_{48}\text{T}_{12}$ specimen had a slightly lower DC ionization response than the CGA glass, but it could be operated at room temperature, and the response increased with the applied field. Particularly noteworthy is the observation that the incorporation of Te in As-Se glass produced a four-fold increase in DC ionization response as compared to pure arsenic triselenide glass. The $\text{As}_{40}\text{Se}_{60}$ specimen could also be operated at room temperature, and showed a DC ionization response to both α - and γ -radiation. Additionally, due to its high resistivity, it could be operated at fields in excess of 10^4 V/cm without breaking down. At fields in excess of 7×10^3 V/cm, avalanche gain was observed, such that the power generated from the device exceeded the power deposited into it by the radiation source. Detector gain values as high as 280% were measured at field of 1.3×10^4 V/cm.

ACKNOWLEDGMENT

The authors would like to gratefully acknowledge the assistance of C. Chamberlain and Y. Zhang for their assistance on this project.

REFERENCES

- [1] B. Pistoulet, J. L. Robert, J. M. Dusseau, and L. Ensuque, "Conduction mechanisms in amorphous and disordered semiconductors explained by a model of medium-range disorder of composition," *J. Non-Cryst. Solids*, vol. 29, pp. 29–40, 1978.
- [2] N. F. Mott, "Introductory talk: Conduction in non-crystalline materials," *J. Non-Cryst. Solids*, vol. 8–10, pp. 1–18, 1972.
- [3] N. F. Mott, "The origin of some ideas on non-crystalline materials," *J. Non-Cryst. Solids*, vol. 28, pp. 147–158, 1978.
- [4] N. F. Mott, "Closing address," *J. Non-Cryst. Solids*, vol. 35–36, pp. 1321–1323, 1980.
- [5] N. F. Mott, "Pre-exponential factor in the conductivity of liquid and amorphous semiconductors," *J. Non-Cryst. Solids*, vol. 77–78, pp. 115–120, 1985.

- [6] N. F. Mott, "Conduction bands in a non-crystalline environment," *J. Non-Cryst. Solids*, vol. 90, pp. 1–8, 1987.
- [7] N. F. Mott, "Physical aspects of localization," *J. Non-Cryst. Solids*, vol. 97–98, pp. 213–215, 1987.
- [8] N. F. Mott, "Conduction at a mobility edge," *J. Non-Cryst. Solids*, vol. 97–98, pp. 531–538, 1987.
- [9] H. Fritzsche, "Electronic phenomena in amorphous semiconductors," *Annual Review of Materials Science*, vol. 2, pp. 697–744, 1972.
- [10] P. Nagels, "Electronic transport in amorphous semiconductors," in *Amorphous Semiconductors*, M. H. Brodsky, Ed., 2nd ed. New York: Springer-Verlag, 1979, vol. 36, pp. 113–158.
- [11] S. R. Ovshinsky and H. Fritzsche, "Amorphous semiconductors for switching, memory and imaging applications," *IEEE Trans. Elect. Dev.*, vol. ED-20, pp. 91–105, 1973.
- [12] S. Kasap, J. Rowlands, K. Tanioka, and A. Nathan, "Applications of disordered semiconductors in modern electronics: Selected examples," in *Charge Transport in Disordered Solids with Applications in Electronics*, B. Sergei, Ed., 2006, pp. 149–177.
- [13] A. V. Kolobov and K. Tanaka, "Photoinduced phenomena in amorphous chalcogenides: From phenomenology to nanoscale," in *Handbook of Advanced Electronic and Photonic Materials and Devices*, H. S. Nalwa, Ed. San Diego, CA: Academic, 2001, vol. 5, Chalcogenide Glasses and Sol-Gel Materials, pp. 47–90.
- [14] A. Kolobov, H. Oyanagi, A. Roy, and K. Tanaka, "Role of lone-pair electrons in reversible photostructural changes in amorphous chalcogenides," *J. Non-Cryst. Solids*, vol. 227–230, pp. 710–714, 1998.
- [15] H. Fritzsche and S. R. Ovshinsky, "Electronic conduction in amorphous semiconductors and the physics of the switching phenomena," *J. Non-Cryst. Solids*, vol. 2, pp. 393–405, 1970.
- [16] V. Balitska, O. Shpotyuk, and H. Altenburg, "Bimolecular relaxation kinetics observed in radiation-optical properties of Ge-As(Sb)-S glasses," *J. Non-Cryst. Solids*, vol. 352, pp. 4809–4813, 2006.
- [17] R. Y. Golovchak, A. Kozdras, C. Gorecki, and O. I. Shpotyuk, "Gamma-irradiation-induced physical ageing in As-Se glasses," *J. Non-Cryst. Solids*, vol. 352, pp. 4960–4963, 2006.
- [18] O. Shpotyuk, A. Kozdras, T. Kavetskiy, and J. Filipecki, "On the correlation between void-species structure of vitreous arsenic selenide studied with X-ray diffraction and positron annihilation techniques," *J. Non-Cryst. Solids*, vol. 352, pp. 700–703, 2006.
- [19] O. I. Shpotyuk and R. Y. Golovchak, "Physical aging effects in selenide glasses accelerated by highly energetic [gamma]-irradiation," *J. Non-Cryst. Solids*, vol. 352, pp. 704–708, 2006.
- [20] O. I. Shpotyuk, A. P. Kovalskiy, T. S. Kavetskiy, and R. Y. Golovchak, "Threshold restoration effects in [gamma]-irradiated chalcogenide glasses," *J. Non-Cryst. Solids*, vol. 351, pp. 993–997, 2005.
- [21] V. Balitska, R. Golovchak, A. Kovalskiy, E. Skordeva, and O. I. Shpotyuk, "Effect of Co60 [gamma]-irradiation on the optical properties of As-Ge-S glasses," *J. Non-Cryst. Solids*, vol. 326–327, pp. 130–134, 2003.
- [22] O. I. Shpotyuk, J. Filipecki, A. Kozdras, and T. S. Kavetskiy, "Radiation-induced defect formation in chalcogenide glasses," *J. Non-Cryst. Solids*, vol. 326–327, pp. 268–272, 2003.
- [23] V. O. Balitska and O. I. Shpotyuk, "Radiation-induced structural transformations in vitreous chalcogenide semiconductors," *J. Non-Cryst. Solids*, vol. 227–230, pp. 723–727, 1998.
- [24] O. I. Shpotyuk, V. O. Balitska, and M. M. Vakiv, "Effect of electron-induced dichroism in vitreous As₂S₃," *J. Non-Cryst. Solids*, vol. 227–230, pp. 837–841, 1998.
- [25] O. I. Shpotyuk and A. O. Matkovskii, "Radiation-stimulated processes in vitreous arsenic trisulphide," *J. Non-Cryst. Solids*, vol. 176, pp. 45–50, 1994.
- [26] B. T. Kolomiets and V. M. Lyubin, "Photoelectric phenomena in amorphous chalcogenide semiconductors," *Phys. Stat. Sol. (a)*, vol. 17, pp. 11–46, 1973.
- [27] T. Minami, A. Yoshida, and M. Tanaka, "Gamma-ray induced conductivity of vitreous semiconductors in the systems As-S-Te and As-Se-Te," *J. Non-Cryst. Solids*, vol. 7, pp. 328–36, 1972.
- [28] M. Hoheisel and L. Batz, "Requirements on amorphous semiconductors for medical X-ray detectors," *J. Non-Cryst. Solids*, vol. 266–269, pp. 1152–1157, 2000.
- [29] S. Ross, G. Zentai, K. S. Shah, R. W. Alkire, I. Naday, and E. M. Westbrook, "Amorphous silicon, semiconductor X-ray converter detectors for protein crystallography," *Nuclear Instrum. Meth. Phys. Res. A (Accelerators, Spectrometers, Detectors and Associated Equipment)*, vol. 399, pp. 38–50, 1997.
- [30] G. A. M. Amin and N. M. Spyrou, "Study of gamma-radiation-induced optical effects in Ge-Se-Cd for possible industrial dosimetric applications," *Rad. Phys. Chem.*, vol. 72, p. 419, Mar. 2005.
- [31] L. C. Burton, C. F. Smith, Jr, A. F. Carroll, and L. H. Slack, "Studies of CdSiAs₂ for photovoltaic applications," in *Proc. Southeastcon '79*, Roanoke, VA, 1979, pp. 25–28.
- [32] S. Kumar, B. R. Mehta, S. C. Kashyap, and K. L. Chopra, "Amorphous chalcogenide thin-film schottky barrier (Bi/As₂Se₃/ : Bi) solar cell," *Appl. Phys. Lett.*, vol. 52, pp. 24–26, 1988.
- [33] J. Schottmiller, M. Tabak, G. Lucovsky, and A. Ward, "The effects of valency on transport properties in vitreous binary alloys of selenium," *J. Non-Cryst. Solids*, vol. 4, pp. 80–96, 1970.
- [34] M. D. Tabak, "High field transport and impurity effects in amorphous Se and As-Se alloy system," in *Proc. 2nd Int. Conf. Conduction Low Mobility Materials*, Eliat, Israel, 1971, p. 276.
- [35] S. Dorenzo, E. Bourret-Courchesne, F. J. James, M. K. Klintonberg, Y. Porter-Chapman, J. Wang, and M. J. Weber, "Identifying semiconductors by D.C. ionization conductivity," in *2005 IEEE Nuclear Science Symposium Conference Record*, Puerto Rico, 2005, pp. 1132–1134.
- [36] Kern and Duotinen, *RCA Review*, vol. 31, p. 186, 1970.
- [37] B. J. Riley, B. R. Johnson, S. K. Sundaram, M. H. Engelhard, R. E. Williford, and J. D. Olmstead, "Pressure-temperature dependence of nanowire formation in the arsenic-sulfur system," *Phys. Chem. Glass*, vol. 47, pp. 675–80, 2006.
- [38] B. R. Johnson, M. J. Schweiger, and S. K. Sundaram, "Chalcogenide nanowires by evaporation-condensation," *J. Non-Cryst. Solids*, vol. 351, pp. 1410–1416, 2005.
- [39] B. R. Johnson, B. J. Riley, S. K. Sundaram, J. V. Crum, C. Henager, Y. Zhang, V. Shuthanandan, C. E. Seifert, R. M. V. Ginhoven, and C. Chamberlin, "Synthesis and characterization of bulk vitreous CdGe₂As₂," *J. Amer. Cer. Soc.*, 2009.

Tricadmium Digermanium Tetraarsenide: A New Crystalline Phase Made with a Double-Containment Ampoule Method

Brian J. Riley,^{†,*} Bradley R. Johnson,* Jarrod V. Crum,* and Michael R. Thompson

Pacific Northwest National Laboratory, Richland, WA 99352, USA

A new crystalline phase in the Cd-Ge-As family of materials has been recently discovered. This phase was made with a unique double-containment ampoule method that provided a specific cooling rate along with a thermal compression mechanism. The composition of this crystalline phase was determined to be $\text{Cd}_3\text{Ge}_2\text{As}_4$ with energy dispersive spectroscopy. The detailed methods used to fabricate these crystals are presented. The crystal structure is still under investigation, although preliminary results are given.

I. Introduction

TERNARY chalcopyrites are a family of materials with composition I-III-VI₂ ($\text{A}^{\text{III}}\text{B}^{\text{VI}}\text{C}_2^{\text{VI}}$) or II-IV-V₂ ($\text{A}^{\text{II}}\text{B}^{\text{IV}}\text{C}_2^{\text{V}}$) that can be formed as amorphous, polycrystalline, and/or single-crystal compounds that are often semiconductors. The II-IV-V₂ chalcopyrites are analogous to the widely studied III-V materials (i.e., GaP, GaAs), except that their crystal structure is tetragonally distorted from the cubic III-V zincblende structure.^{1,2} Numerous applications and important properties have been discovered for chalcopyrite compounds and nonchalcopyrite $\text{Cd}_x\text{Ge}_y\text{As}_z$ compounds including photovoltaics and photoconductivity,^{3–5} semiconductor radiation detection,^{5,6} spintronics,⁷ nonlinear optics,^{8–10} superconductivity,^{11,12} high refractive index (n) ($n \geq 3.5$),^{8,13} high room temperature electron mobility,^{14,15} and windows for infrared lasers.^{8,16,17}

Here, we report the discovery of a new, previously unreported Cd-Ge-As phase with the simplified composition of $\text{Cd}_3\text{Ge}_2\text{As}_4$ (hereafter referred to as 3-2-4) with a technique termed the *double-containment* (DC) ampoule method. In 2008,¹⁸ this 3-2-4 compound was first discovered while attempting to manufacture a variety of bulk, amorphous CdGe_yAs_z compounds (i.e., $y = 0.45, 0.65, 0.85, \text{ and } 1.00$).¹⁹ The 3-2-4 crystals have yet to be created as large, single crystals, but they have been repeatedly synthesized under different conditions.

Here, we present the chemical analysis of the 3-2-4 phase as well as the results from a series of experiments performed to better understand the formation of this phase. The Cd-Ge-As ternary diagram has been researched in the past, however, this particular phase has never been observed. Thus, we present a detailed description of the techniques used to fabricate these crystals so that these methods are well-documented.^{1,20–26} In addition, the DC processing method might be useful to create other $\text{A}^{\text{II}}\text{B}^{\text{IV}}\text{C}^{\text{V}}$ materials of interest to the scientific community, for example, Cd-Sn-As.

II. Background

One of the more widely studied $\text{Cd}_x\text{Ge}_y\text{As}_z$ compounds is the stoichiometric $\text{A}^{\text{II}}\text{B}^{\text{IV}}\text{C}_2^{\text{V}}$ chalcopyrite (hereafter referred to as 1-1-2). Historically, the 1-1-2 compound is most often preferred in single-crystal form, however, the growth of large single crystals has proven challenging.^{1,2} The consensus has been that the anisotropic thermo-physical properties of this material are the root cause for these problems. The large variations in the linear coefficients of thermal expansion between the a -axis ($\alpha_{L(a)}$) and the c -axis ($\alpha_{L(c)}$) tend to create strain gradients that lead to defects and cracking in large boules.^{9,17,27–29} Most of the early work with this material revealed issues with polycrystallinity, cracking, and poor optical properties, although recently, new processing techniques were developed to produce high purity single crystals using a horizontal gradient freeze growth method.^{11,22,26,30,31}

To determine the best processing route to create large single crystals, detailed phase diagrams and glass-formation studies were conducted by implementing melt-quench techniques where the processing temperatures (T_p), and quench temperatures (T_q) were similar to those in this current work.^{1,20–26} One of the more complete phase diagrams was published by Borshchevskii and Roenkov.²² They studied CdGe_3As_2 compounds with a melt-quench method and determined that the 1-1-2 compound coexisted with Ge, GeAs, CdAs_2 , and Cd_3As_2 . With a melt-quench approach, Pamplin and Feigelson determined that at 550°C, the 1-1-2 compound was in equilibrium with Ge, GeAs, CdAs_2 , Cd_2GeAs_4 , and Cd_3As_2 .²⁵ The coexistence of these additional species with similar thermodynamic stability increases the difficulty of growing single crystals of the 1-1-2 compound. However, despite all of this prior work with Cd-Ge-As compounds, these prior studies did not report the formation of the 3-2-4 phase as discussed here according to either their reported X-ray diffraction (XRD) patterns or their morphological descriptions. One of these studies even batched the $\text{Cd}_3\text{Ge}_2\text{As}_4$ composition directly, but did not report the phase we are presenting here.²⁵

Figure 1 summarizes the Cd-Ge-As phases present in the International Crystal Structure Database along with the diffraction pattern of the 3-2-4 phase and Fig. 2 shows where the 3-2-4 phase fits into the abridged Cd-Ge-As ternary diagram.^{22–25} Although the composition of the 3-2-4 phase is close to that of the $\text{Cd}_4\text{Ge}_3\text{As}_5$ (4-3-5) phase reported by Pamplin and Feigelson,²⁵ the diffraction pattern for the 3-2-4 phase did not match that of the 4-3-5 phase, or any other phase in the International Crystal Structure Database (Fig. 1). Thus, the 3-2-4 materials were deemed unique. A summary of the various Cd-Ge-As compounds that we found in the literature are presented in Table I.^{23–25,32,33}

Hong *et al.*²³ performed melt-quench experiments with CdGe_yAs_z compounds (where $y = 0.3$ and 0.6) and reported crystalline phases observed with XRD that they were unable to match to known compounds in the crystal structure database. The temperature range at which Hong *et al.* observed these phases was $T \sim 407^\circ\text{C}–413^\circ\text{C}$ and the diffraction

J. Heo—contributing editor

Manuscript No. 30484. Received October 12, 2011; approved February 20, 2012.

*Member, The American Ceramic Society

[†]Author to whom correspondence should be addressed. e-mail: brian.riley@pnl.gov

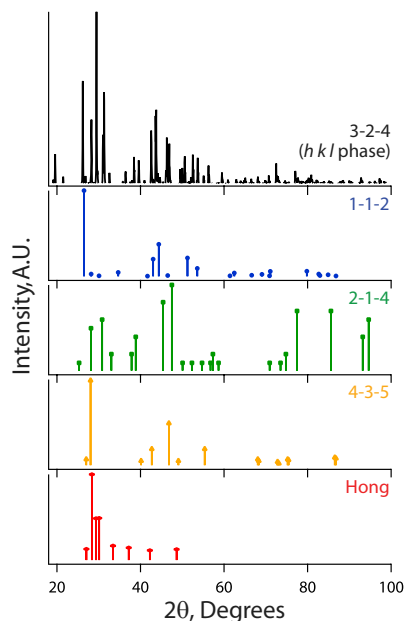


Fig. 1. Summary of diffraction patterns from the literature compared with the calculated pattern (*hkl* phase, see text) for the 3-2-4 phase. Literature data consists of the 1-1-2,⁴² 2-1-4,^{24,33} and 4-3-5²⁵ phases along with an extracted data set of unknown diffraction peaks from Hong *et al.*²³

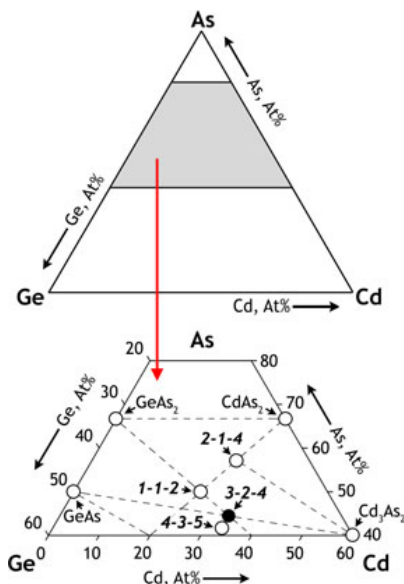


Fig. 2. Cd-Ge-As ternary diagram showing the placement of the 3-2-4 phase (●). This diagram was recreated from the diagram presented by Borschchevskii and Roenkov²² with added phases from Pamplin and Feigelson²⁵ as well as Mikkelsen and Hong²⁴ (○). The phases from Hong *et al.* are Ge-deficient ($\text{Ge} \leq 11 \text{ at.}\%$) and are not included here.²³ The top portion shows where the inset (bottom portion) is located on the full ternary diagram.

patterns are similar to those seen for the 3-2-4 phase observed in the current study (Fig. 1). However, Hong *et al.* showed these crystallites (of unknown composition) as being very small ($\sim 400 \text{ nm} \times 1 \text{ }\mu\text{m}$) and irregularly shaped, which does not coincide with the oriented morphology of the 3-2-4 crystallites observed in the current study.

Table I. Summary of Crystalline Cd-Ge-As (CGA) Phases Observed in the Literature (Data are Sorted by Cd at.% from Lowest to Highest)

Simplified (Cd-Ge-As)	Elemental %'s (Cd-Ge-As)	Reference(s)
3.5-45.5-1	7-91-2	Hong <i>et al.</i> ²³
4.3-27-2	13-81-6	Hong <i>et al.</i> ²³
1-1-2	25-25-50	Pfister ³²
4-1-9,3	28-7-65	Hong <i>et al.</i> ²³
2-1-4	29-14-57	Mikkelsen and Hong ²⁴ , Chernov <i>et al.</i> ³³
3-1-5.1	33-11-56	Hong <i>et al.</i> ²³
4-3-5	33-25-42	Pamplin and Feigelson ²⁵
3-2-4	33-22-45	Current work

In addition to crystalline ternary $\text{A}^{\text{II}}\text{B}^{\text{IV}}\text{C}_2^{\text{V}}$ chalcopyrites, many have worked on exploring the amorphous analogs. In contrast to most oxide glasses, the amorphous structure of chalcogenide- and chalcopyrite-compounds is thought to closely resemble that of the crystalline analogs.²³ The most stable ternary amorphous compounds were found to be CdGeAs_2 , CdSiAs_2 , ZnGeAs_2 , and ZnSiAs_2 listed in order of decreasing glass-forming tendency (K_{gl}) based on the Hruby criterion.³⁴ Sharma *et al.*¹ explains the Hruby criterion as

$$K_{\text{gl}} = (T_c - T_g)/(T_m - T_c) \quad (1)$$

where T_g , T_c , and T_m are the glass transition, crystallization, and solidus or melting temperatures, respectively. A higher K_{gl} means that a glass is easier to quench into the amorphous state than a glass with a lower K_{gl} . Glasses with low K_{gl} values (<1) are poor glass-formers and require fast quenching rates, r_c , in order to be supercooled into an amorphous state.^{35,36} Thus, Boltovets *et al.* investigated several different quenchants including: H_2O and $\text{NaCl}/\text{H}_2\text{O}$ ($r_c \sim 140$ – $150^\circ\text{C}/\text{s}$ at 35°C), liquid gallium ($r_c \sim 80^\circ\text{C}/\text{s}$ at 210°C and $r_c \sim 55^\circ\text{C}/\text{s}$ at 290°C), and liquid tin ($r_c \sim 40^\circ\text{C}/\text{s}$ at 370°C).³⁵ For the systems with poor glass formation, where $K_{\text{gl}} < 0.2$, the quench rate required for glass formation was rather high, that is, >50 – $200^\circ\text{C}/\text{s}$. This quenching rate falls between the amorphous chalcogenides that require low quench rates and amorphous metals that require extremely high quench rates, typically made only in thin film form.^{35,36} Some of these different quenchants were used in the work presented here.

III. Methods

(1) Materials Processing

The six samples discussed here were labeled with CGA-# where the # does not necessarily denote the sequential order in which the experiments were conducted. The full process by which the DC ampoules were prepared can be found in our previous work, but a condensed version will also be presented here.¹⁹ Two different sizes of GE214 fused quartz (GM Associates, Inc., Oakland, CA) reaction vessels were used for these experiments, $10 \text{ mm} \times 12 \text{ mm}$ tubes and $19 \text{ mm} \times 22 \text{ mm}$ tubes (inner \times outer diameter). Each vessel was prepared similarly where it was: (1) shaped with a torch, (2) cleaned with an RCA1 etch process at 70°C (2 h) and rinsed with deionized water (DIW),³⁷ (3) soaked in a solution of 5:5:90 HNO_3 :HF:DIW (by volume) for 2 h and rinsed in DIW,²⁹ (4) annealed at 1160°C for 1 h in a horizontal quartz tube furnace, and then (5) baked at 200°C in a furnace (Deltach, Inc. Denver, CO) within a nitrogen glove box, with $< 0.1 \text{ ppm}$ of $\text{O}_2/\text{H}_2\text{O}$ (M-Braun, Inc., Stratham, NH).

Next, ultra-high purity elemental constituents of Cd (6N), Ge (6N), and As ($>7\text{N}$) (Alfa Aesar, Ward Hill, MA) were added into the inner vessel ($10 \times 12 \text{ mm}$) while inside the glove box. The total mass of the charge, m_s , varied by experi-

Table II. Processing Data and Observations for Each Experiment

Sample ID	Comp.	Method	P_i (Pa)	T_p (°C)	T_q (°C)	T_{an} (°C)	m_s (g)	m_{Cu} (g)
CGA-1	1-1-2	SC-C	1.2×10^{-4}	870	W, 20 ± 2	N/A	10.8572	N/A
CGA-2	1-1-2	SC	3.4×10^{-5}	800	Ga, 150	340	13.3010	N/A
CGA-3	1-1-2	DC	1.0×10^{-5}	800	W, 20 ± 2	395	13.3143	24.0
CGA-4	1-1-2	DC	1.5×10^4	825	W, 20 ± 2	360	7.3684	12.5
CGA-5	1-1-2	DC	1.6×10^4	850	W, -2 ± 0.2	360	13.3853	17.8
CGA-6	3-2-4	DC	1.6×10^4	850	W, 20 ± 2	360	13.3426	17.7

All were heat-treated at the processing temperature, T_p , for 25 h and annealed at the annealing temperature, T_q , for 8 h. P_i dictates the initial pressure (in Pa) inside the ampoule containing the elemental constituents (Figure 3(a)). T_p denotes the processing temperature of the ampoule (in °C). Quenchants used were liquid gallium, or Ga, at $150 \pm 5^\circ\text{C}$, and water, or W, at the temperature listed, i.e., -2°C or $20 \pm 3^\circ\text{C}$. The sample mass, m_s , and mass of copper used, m_{Cu} , are listed (in g).

ment with a range of ~ 7 – 13 g (Table II). The vessel loaded with chemicals was transferred to a vacuum assembly where it was evacuated to 10^{-5} Pa ($\sim 10^{-7}$ Torr) with a turbomolecular pump backed by a scroll pump. The vessel was purged with semiconductor-grade (ULSI 6N purity) 2.6% H₂/Ar-balance (Matheson Tri-Gas, Newark, CA) and then sealed under vacuum with a torch. This concludes the preparation for the single-containment ampoule (SC) as seen in Fig. 3(a).

For one of the specimens discussed here, CGA-1, the interior of the SC vessel was coated with a pyrolytic graphite layer by covering the interior of the ampoule with acetone (99.9% purity, Fisher Scientific, Pittsburgh, PA), pouring it out, and then heating the vessel with a torch while it was inverted. This was done as an extra step prior to inserting the charge to help prevent chemical attack on the quartz by the charge; however it was later deemed unnecessary as the chemicals did not noticeably attack the quartz.¹⁹ The method of implementing carbon-coated SC ampoules was termed the “SC-C” method (Table II).

For the four DC experiments presented in Table II, once the ampoule with the elements was vacuum-sealed constituting the SC ampoule, this ampoule was then centered vertically inside of the 19×22 mm tube and -75 μm (-200 mesh) copper powder was loaded into the annulus between the vessels. The height of copper powder varied by experiment, but was poured to match the predicted height of the final melted charge. This height was calculated with the measured density of amorphous CdGeAs₂, ~ 5.74 g/cm³ presented in the literature, and the total mass of copper, m_{Cu} , used in each experiment is listed in Table II.^{19,38} The copper charge was added as a thermal conductor between the two quartz tubes and is explained in further detail in our previous work.¹⁹ It also acted as a constraining, compressive force during cooling due to the significantly larger (30 – $60 \times$) linear coefficient of

thermal expansion for copper ($\alpha_{L,Cu}$) over fused quartz ($\alpha_{L,FQ}$).^{39–41}

The outer ampoule was evacuated in the same fashion as the inner ampoule and then sealed with a torch. Then, the sealed ampoule (Fig. 3(b)) was instrumented with type-K thermocouples (OMEGA Engineering, Inc., Stamford, CT) that were connected to a data acquisition system (HYDRA 2620, Fluke Corporation, Everett, WA) for temperature monitoring during the heat-treatment process. The ampoule with thermocouples was connected to a stainless steel basket and inserted into an Inconel[®] secondary containment vessel spanning through the hot-zone region of a Deltech furnace on an adjustable, custom-built rocking platform. The furnace was set to rock with an 18.5-cm radius and pause at the extremes of a 30° throw (from horizontal) for 15 s dwell times at each extreme with a heating profile as follows:

$$20^\circ\text{C} \xrightarrow{3^\circ\text{C}/\text{min}} 400^\circ\text{C} \xrightarrow{2 \text{ h}} 400^\circ\text{C} \xrightarrow{3^\circ\text{C}/\text{min}} 625^\circ\text{C} \xrightarrow{2 \text{ h}} 625^\circ\text{C} \xrightarrow{3^\circ\text{C}/\text{min}} T_p \xrightarrow{25 \text{ h}} T_p \xrightarrow{\text{quench}(T_q)} \text{quench}(T_q) \quad (2)$$

Samples were held around the T_m of cadmium (321°C) and sublimation temperature of arsenic (616°C) to allow for slow mixing to control the vapor pressures inside the ampoule(s).

Following the heat-treatment, the sample holder and ampoule were quickly removed from the furnace and quenched immediately into either water ($T_q = -2 \pm 0.2^\circ\text{C}$ or $20 \pm 2^\circ\text{C}$) or liquid gallium ($T_q = 150 \pm 5^\circ\text{C}$), where the quench bath temperatures were monitored by a type-K thermocouple (Table II). After ~ 10 min of sitting in the quenchant to cool, the ampoule was removed from the stainless steel holder, dried, and moved to the glovebox. The ingot, still inside the ampoule (SC) or ampoules (DC, see Figure 3(e)), was then annealed at T_{an} (Table II) for 6.7 h at a heating rate of $2^\circ\text{C}/\text{min}$ and a cooling rate of $1.5^\circ\text{C}/\text{min}$ to help relieve the thermal stresses inherent in the glass after quenching.

Following annealing, the outer tubes of the DC specimens were removed (Figure 3(d)). For the SC ampoule, the ingot was removed from the quartz tube, but for the DC specimens the ingot remained inside the inner ampoule and copper sheath for subsequent processing. The SC ingot (CGA-1) was casted in resin and curing was assisted by a pressure chamber at $\sim 3 \times 10^5$ Pa. The DC specimens were not mounted in resin as the sintered copper sheath around the inner ampoule provided enough support for further processing of the specimens.

Specimens were cut with either a variable speed diamond saw (Buehler, Lake Bluff, IL) or a CT400 diamond wire saw (Diamond Wire Technology, LLC, Colorado Springs, CO) into ~ 1 – 1.5 -mm thick discs perpendicular to the longitudinal axis of the ingot. Specimens were polished with an LP-01 Syntro vibratory polisher (FMC Technologies, Saitlito, MS) to a < 1 μm finish and then characterized. The processing variables that were altered between experiments are presented in Table II.



Fig. 3. Progression of double-containment method (all images collected from CGA-3 with the “base” of the ampoule at the left and the “top” of the ampoule at the right. (A) Stoichiometric quantities of constituents batched into a 10×12 mm (ID \times OD) fused quartz ampoule, evacuated, and sealed. (B) Inner ampoule is loaded into a larger, $19 \text{ mm} \times 22 \text{ mm}$, ampoule and copper powder is added to the void between the two ampoules, the outer ampoule is evacuated and sealed (prior to heat treatment). (C) After heat treatment. (D) Inner ampoule with sintered copper jacket removed from outer ampoule. (E) Ingot removed from inner ampoule. The scale-bar is valid for all photographs.

(2) Microscopy

The various phases present in these specimens were so close in composition to the 1-1-2 crystalline material and residual amorphous matrix that they were not distinguishable with basic microscopy unless polarized light or a strong compositional contrasting method was implemented (such as scanning electron microscopy with backscattered electron contrast (SEM-BSE). Cross-sectioned specimens were observed under cross-polarized light at various magnifications (12.5–1000 ×) with a Leitz Orthoplan optical microscope (Leica Microsystems GmbH, Wetzlar, Germany). Cross-polarized light optical microscopy provided the ability to distinguish between amorphous, polycrystalline 1-1-2, and polycrystalline 3-2-4 phases. Laser confocal scanning microscopy was performed with a Keyence VK9710 microscope (Keyence Corporation of America, Elmwood Park, NJ) and a 50 × objective to look for differences in optical appearance between the phases as well as to measure the variation in height across the specimen.

Polished specimens were also examined with SEM-BSE. Two different SEMs were used during analysis and included a JSM-5900 (JEOL, Ltd., Tokyo, Japan) and an FEI Helios 600 Nanolab (FEI Company, Hillsboro, OR). Energy dispersive spectroscopy (EDS) spot, area, and dot-mapping analyses were performed on the unknown phase (3-2-4) with the JEOL 5900 SEM with an EDAX Si-drifted EDS detector (Apollo XL, 30 mm²) and EDAX Genesis 6.2 software (AMETEK, Berwyn, PA). Portions of the 3-2-4 crystals from CGA-4e were removed with a focused ion beam (FIB) attachment and an OmniProbe 250 lift-out accessory on the FEI SEM for transmission electron microscopy (TEM). TEM was performed with a JEOL 2010F equipped with a field emission gun and digital images were captured with a Gatan bottom-mounted charge-coupled device camera and DigitalMicrographTM software (Gatan Inc., Pleasanton, CA). Specimens were analyzed in bright field, selected area, and convergent beam electron diffraction modes. Chemical analysis of selected locations was performed with EDS analysis with an Oxford Inca system (Oxford Instruments PLC, Tubney Woods, Abingdon, U.K.).

(3) X-ray Diffraction

XRD was performed on powders of all the samples with a Bruker[®] D8 Advance (Bruker AXS Inc., Madison, WI), equipped with a CuK_α target at 40 kV and 40 mA. The instrument had a LynxEyeTM position-sensitive detector with an angle range 3° 2θ. Scan parameters used for sample analysis were 5–110° 2θ with a step of 0.015° 2θ and a 0.3-s dwell at each step. JADE 6[®] (Materials Data, Inc., Livermore, CA), Bruker AXS DIFFRAC^{plus} EVA, and Bruker AXS Topas 4.2 software were used to identify and quantitate phase assemblages. XRD analysis was performed on both polished discs and powdered specimens.

IV. Results

Figures 4(b)–(f) provides a summary of the cross-sectioned appearance of most of the samples discussed here and Table III provides a summary of the estimated phase concentrations from each experiment. Chronologically, CGA-1 was the first experiment we performed where the 3-2-4 phase was observed (Figs. 4(a) and (b)); however, the quantity of this phase was so small (Fig. 4(a)) that it was disregarded at first. We achieved a nearly amorphous sample with the SC experiment (CGA-2). The second time the 3-2-4 phase was synthesized, in CGA-3, it was observed in very large quantities at ~30%, by volume. The primary difference between these two experiments was the ampoule processing method. Thus, the increase in the 3-2-4 phase volume fraction was attributed to the DC ampoule processing method. Experiment CGA-2 was quenched in liquid gallium and was almost completely amorphous (see Table III). Experiments CGA-3, CGA-4, and CGA-5 all had similar appearances though slight differences in phase distribution. Experiment CGA-6 turned out very different where almost the entire ingot was the 3-2-4 phase.

Energy dispersive spectroscopy analysis was performed with SEM and TEM and revealed a higher at.% of Cd in the new, unknown phase than was present in the 1-1-2 phase or the glass (Fig. 5). The EDS compositional data is presented in Table IV and an average simplified composition of

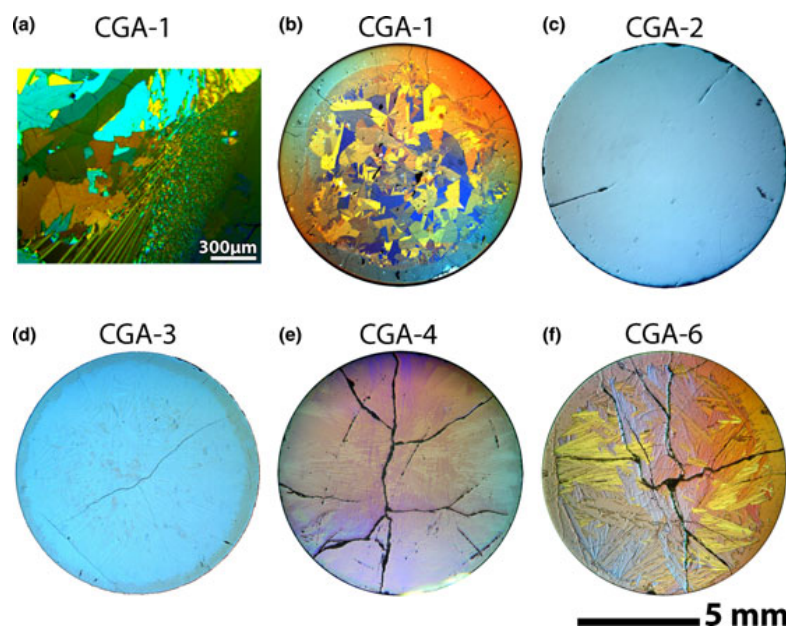


Fig. 4. Visual comparison of the CGA-# samples. Here, cross-polarized light optical micrographs (Leitz microscope, 12.5 ×) are presented for each sample except for CGA-5, which appeared very similar to CGA-4, for comparison purposes. The 3-2-4 crystallites in (d) and (e) are so small that they do not appear at these magnifications.

Table III. Summary of Phase Quantities Observed in the Various Experiments

Sample ID	%1-1-2	%3-2-4	%Am.	Other
CGA-1	89	1	10	N/A
CGA-2	5	0	95	N/A
CGA-3	30	30	40	N/A
CGA-4	10	40	50	N/A
CGA-5	5	50	45	N/A
CGA-6	<0.1	95	4	<1 [†]

Volume percentages are estimated from an average analysis of various specimens from each sample with CPLM where %1-1-2, %3-2-4 and %Am denote the percent of the 1-1-2, 3-2-4, and amorphous phases, respectively.

N/A, Not Applicable.

[†]This covers other phases present that include amorphous and crystalline phases of various compositions (see text).

the new phase is Cd₃Ge₂As₄. The increased Cd content in the new phase is evident from the BSE micrograph with atomic number contrast as well as in the elemental map that also shows Cd depletion adjacent to the crystal (Fig. 5). The dark streaks present in the core of the 3-2-4 crystals in Fig. 5 were found to be amorphous with TEM selected area diffraction and had a composition matching closely to the composition of the amorphous regions as observed with SEM (Table IV).

Initial queries about the 3-2-4 crystals included the mechanism of nucleation and crystallization as well as the crystallographic morphology. Initial observations with cross-polarized light microscopy led us to believe that these new crystals were rods protruding from the perimeter of the specimen and growing inward toward the longitudinal axis of the cylindrical

ingot. However, the corner of a specimen prepared with a polished examination of a longitudinal and transverse face revealed that the 3-2-4 phase grew as platelets.

Figure 6 shows an example of the 1-1-2 and 3-2-4 crystal growth patterns along the perimeter of polished discs cut perpendicular to the longitudinal axis from specimens of CGA-4. These projections were observed in several locations (i.e., 30–40) along the perimeters of these specimens and ~95% of the 1-1-2 crystals were observed within ~1 mm of the perimeter as evidenced by the 1-1-2 polycrystallites. As the crystals have plate-like morphology in the bulk of the ingot and originate out of single nucleation sites as viewed in perpendicular specimen orientations, we believe that they are triangular-shaped plates where the apex is on the outer perimeter surface of the cylindrical ingot.

Confocal laser scanning microscopy, which is inherently polarized, provided interesting contrast between the different phases present in the specimens (Fig. 6(b)), comparable to the cross-polarized light micrographs obtained (Fig. 6(a)). Confocal laser scanning microscopy did not provide resolution between different orientations of 1-1-2 crystallites as was obtained with cross-polarized light microscopy, evidenced by the color variations in the different grains. However, the confocal laser scanning microscope was able to observe the topology of polished specimens. The topology maps revealed that the 3-2-4 phase was lower than the surrounding amorphous phase, by an average of 120 ± 10 nm. Thus, we believe that the 3-2-4 phase is slightly softer than the residual bulk amorphous glass and 1-1-2 phase, and was preferentially removed during the polishing process.

When cross-sections were made of CGA-4 and CGA-5 perpendicular to the longitudinal axis of the ingot, the crystals were optically observed in the two distinct widths of narrow

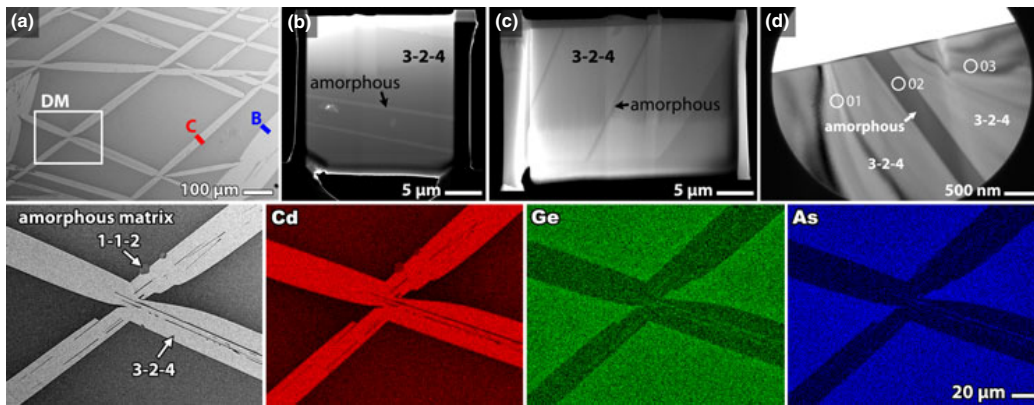


Fig. 5. (A) CGA-4e sample location where an SEM (JEOL 5900) dot map was performed (region denoted by “DM”) and the location where samples were removed with the FIB (labeled “B” and “C”) for TEM analysis that correspond to (B) and (C). (B) FIB section micrograph (region “B” from (A)) captured with high angle annular dark field (HAADF) in scanning transmission (STEM) mode where the 3-2-4 phase appears darker than the amorphous background. FIB section micrograph (region “C” from (A)) captured with an Everhardt-Thornley secondary electron detector where the 3-2-4 phase appears brighter than the amorphous background. (D) TEM micrograph showing regions of EDS analysis on (C) where the specimen is flipped 180°C from the micrograph (C). Along the bottom row is a Backscattered SEM dot map from in the region outlined by the “DM” box in (A) showing the elemental distribution of Cd, Ge, and As.

Table IV. Compositional Information (in at.%) via EDS for the Different Regions Observed in These Specimens: the CdGeAs₂ or 1-1-2 Phase, the Unknown Phase (~Cd₃Ge₂As₄), and the Amorphous Matrix

Collection Method: Element	SEM			TEM		
	Cd	Ge	As	Cd	Ge	As
Unknown phase (3-2-4)	32.75 (0.68)	21.65 (0.26)	45.60 (0.42)	33.89 (0.29)	22.35 (0.20)	43.76 (0.08)
1-1-2	25.05 (0.44)	24.38 (0.23)	50.57 (0.41)	N/A	N/A	N/A
Amorphous matrix	20.81 (2.87)	25.14 (0.51)	54.05 (2.42)	17.29	30.71	52.00

These values were quantified using the Cd-L α , Ge-K α , and As-K α lines with EDS from both SEM and TEM. SEM values were collected on CGA-3 and TEM values were collected on specimen CGA-4 (Figure 5). Calculated error based on standard deviation is listed in parenthesis.

N/A, Not Applicable.

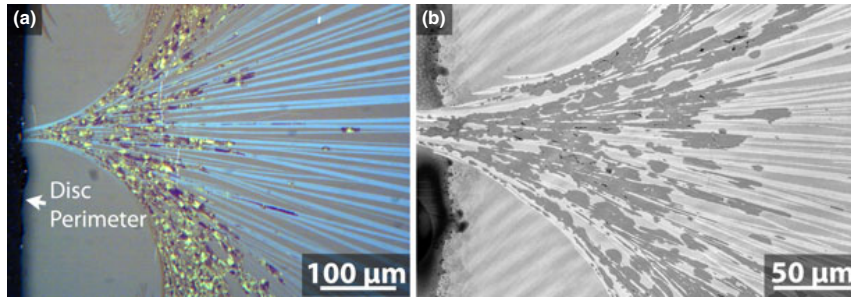


Fig. 6. Growth patterns of the 3-2-4 phase from nucleation sites along the perimeter of the ingot inward toward the longitudinal axis as observed on cross-sections prepared perpendicular to the longitudinal axis of the sample. Here, these patterns are observed with cross-polarized light on an optical microscope (a) and with a confocal laser scanning microscope (b) on polished samples. The 1-1-2 phase shows up as purple-red (a) or dark gray (b) clusters of polycrystallites and the amorphous regions make up the remainder of the micrograph.

(Fig. 5(a), “C”) and wide (Fig. 5(a), “B”). It appeared as though the crystals with different widths were captured at different growth directions or angles, approximately perpendicular to one another. In close observation of the sections removed with the FIB (Figs. 5(b) and (c)), we determined that the 3-2-4 crystals were thin sheets ($\sim 5\text{--}10\ \mu\text{m}$) laminated by amorphous Cd-Ge-As material (200–400 nm thick), as verified with TEM, with similar composition as the bulk (Table IV).

For CGA-4 and CGA-5, the widths of the 3-2-4 crystallites were measured in cross-polarized light micrographs captured in a few different regions on one of the specimens. The thickness of the 3-2-4 plates (in the narrow orientation) was $\sim 10 \pm 3\ \mu\text{m}$ near the perimeter of the specimen and $25 \pm 5\ \mu\text{m}$ near the center of the specimen. The width in the wide orientation was $40 \pm 5\ \mu\text{m}$ near perimeter and $\sim 100 \pm 10\ \mu\text{m}$ near center; thus, the 3-2-4 crystallites grew in width as they approach the center of the ingot. The plates protruded from the perimeter toward the center of the ingot at lengths of $\leq 5\ \text{mm}$ (Fig. 6). A lower density of 3-2-4 crystallites was found toward the center of the ingot than the perimeter. This is consistent with the fact that the 3-2-4 crystals require a large amount of Cd to satisfy the crystal structure and that the crystals increased in size toward the center of the ingots.

The purpose of CGA-6 was to better understand the chemistry limitations on 3-2-4 crystal formation because it was not batched Cd-deficient as opposed to all of the other experiments. For CGA-6, nearly the entire ingot was found to be crystalline (see Table III). Investigations with cross-polarized light microscopy (Fig. 4(f)) and XRD (Fig. 7) revealed that the vast majority of the crystalline phase was the 3-2-4 phase (see Table III).

For CGA-6, the crystallization process appeared similar to CGA-3, CGA-4, and CGA-5, with small crystallites on the perimeter and separate dendritic grains growing toward the core, but the phases observed were different from those observed in the previous samples. Instead of an amorphous rim as observed in CGA-3, CGA-4, and CGA-5, the rim of CGA-6 was composed of the following phases:

1. 3-2-4 phase at the perimeter of the specimen;
2. very small quantities of a Cd-As phase, with a small fraction of Ge as measured with SEM-EDS, another new Cd-Ge-As phase with crystalline-like morphology, growing in the interstitial regions of 3-2-4 grains ($\sim 5\text{--}10\ \mu\text{m}$ in size);
3. amorphous regions deficient in Cd from the as-batched 3-2-4 composition; and
4. a very small quantity of 1-1-2 material ($\leq 0.1\ \text{vol}\%$) observed with cross-polarized light microscopy.

Preliminary single-crystal diffraction analysis (not shown here) on the 3-2-4 crystals determined that the crystals had hexagonal lattice constants, a trigonal system, and a trigonal space group of $P\bar{3}$. The unit cell constants are thought to be

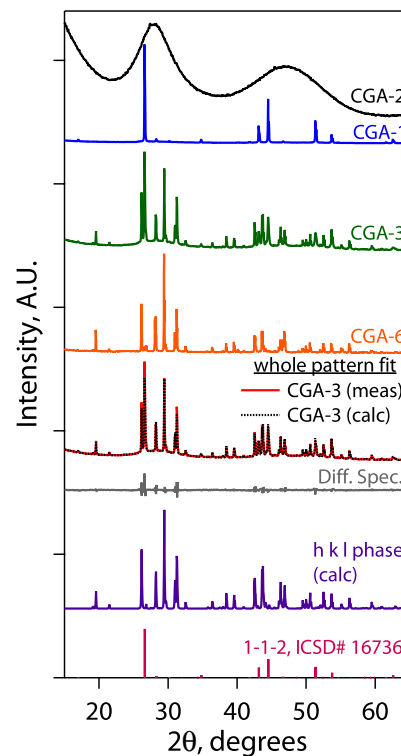


Fig. 7. Compilation of diffraction patterns from various samples showing the progression of amorphous (CGA-2) to 100% 1-1-2 (CGA-1), to mixed 1-1-2 and 3-2-4 (CGA-3), and then to nearly 100% 3-2-4 (CGA-6). Also included in the plot are a calculated hkl pattern for the 3-2-4 phase (hkl phase (calc)), a diffraction pattern for 1-1-2 phase from the ICSD database (16736),⁴² the calculated pattern for CGA-3 including the 1-1-2 phase and the hkl pattern for the 3-2-4 phase (calc) compared with the measured pattern for CGA-3 (meas), and the difference pattern (Diff. Spec.) for the calculated versus measured data.

$a = b = 7.735\ \text{\AA}$, $c = 27.40\ \text{\AA}$, $\alpha = \beta = 90^\circ$, and $\gamma = 120^\circ$. From this data, an hkl fit was performed on the powder diffraction pattern of CGA-3 with Topas 4.2 software. The calculated diffraction pattern was generated including the contribution from the known 1-1-2 phase.⁴²

The XRD results presented in Fig. 7 demonstrate that the calculated hkl pattern for the 3-2-4 phase fits well to the different specimens and the differences in the fit are minimal. Figure 7 shows a progression of crystallization from the amorphous sample (CGA-2), to the sample completely

crystallized with the 1-1-2 phase (CGA-1), to the sample almost completely crystallized with the 3-2-4 phase (CGA-6). The calculated *hkl* pattern shows a good fit to the measured pattern for CGA-3 with minor differences. The CdAs-rich regions observed in CGA-6 were so small that they were not observed in the diffraction pattern (Table III).

V. Discussion

The 3-2-4 phase was created with the DC ampoule technique several times in separate experiments under different conditions, and is therefore a reproducible phase. The 3-2-4 content in specimens batched with a 1-1-2 bulk composition was observed to increase as the T_p was increased and the T_{an} was decreased (Table II). The yield of the amorphous phase remained relatively consistent in CGA-3, CGA-4, and CGA-5.

We believe that the nucleation and growth of this new 3-2-4 phase was caused by one of the following: (1) the presence of a chemical impurity in these specific reactants, (2) the specific cleaning protocol used in these experiments (that might create special heterogeneous nucleation sites), (3) the DC processing method used in this work, and/or (4) something else not considered. The likelihood of a chemical impurity being the cause of the growth of 3-2-4 crystals, that is, a nucleating agent, is low due to the high purity of the reactants ($\geq 6N$'s). However, this possibility was not ruled out.

The ampoule cleaning technique could potentially aid in the nucleation of the 1-1-2 or 3-2-4 crystals on the inner surfaces of the fused quartz ampoule. The acid-etching step was shown to increase the surface area of the quartz where the roughness number, R_a , measured using atomic force microscopy was $3.9 \times$ higher in the acid etched fused quartz versus washing the quartz with DIW only.³⁵ However, considering that the 3-2-4 phase *was* present in CGA-1, where a carbon coating was applied to the inner surface of the ampoule, and the 3-2-4 phase *was not* present in CGA-2, where the ampoule was quenched in liquid gallium, the inner ampoule surface preparation is an unlikely cause of the 3-2-4 appearance. Nevertheless, the inner ampoule surface preparation likely helped nucleate crystallization in the experiments with a lower quenching rate (DC experiments).

For CGA-2, the liquid gallium quenchant effectively wetted the fused quartz ampoule, especially when compared with water at these quenching temperatures ($T \sim 300^\circ\text{C} - 800^\circ\text{C}$) where the water quenchant was above the boiling temperature ($T > 100^\circ\text{C}$). Therefore, a layer of steam formed between the outer ampoule wall and the quenchant at the moment of quenching. Also, the thermal conductivity (k in $\text{W} \cdot (\text{m} \cdot \text{K})^{-1}$) of gallium is rather high at $k_{\text{Ga}} \sim 28.65$ (77°C)– 38.27 (277°C), where the k for liquid water is low at $k_{\text{H}_2\text{O,liq}} \sim 0.56$ (1.9°C)– 0.67 (97°C) and the k for steam is even lower at $k_{\text{H}_2\text{O,gas}} \sim 0.026$ (127°C)– 0.041 (277°C).^{43–45} Thus, the gallium was expected to pull the heat out of the ampoule faster than the water quenchant, providing a higher cooling rate. The increased wettability on fused quartz combined with the higher thermal conductivity of gallium increased the quenching rate of CGA-2. This allowed for supercooling past T_c , allowing for an almost completely amorphous ingot, which was not the case in any of the other samples.

The largest quantities of 3-2-4 crystals were observed in specimens processed with the DC method, that is, the method with the slowest cooling rates of those tested. In our previous work,¹⁹ we discussed the benefits of the DC method and one of those benefits was that the thermal compression of the sintered copper jacketed compressed the inner quartz tube, thereby compressing the material inside of the inner ampoule. The density of amorphous Cd-Ge-As is higher than that of the crystalline analogs,^{19,38} thus this thermal compression might have forced the materials into the amorphous state through the quenching process between T_m and T_c .

The thermal compression of the sintered copper jacket was evidenced by the fact that the copper sheath pulled away from the outer ampoule and compressed very tightly on the inner ampoule – so tightly that it could not be removed unless it was cut off. It is worth noting that the porosity of the sintered copper sheath was rather high at $\sim 46 \pm 2.8$ vol %, as measured by optical microscopy. The increase in thermal mass of the DC method with the additional quartz tube and copper powder ($m_{\text{Cu}} > m_s$) is another key difference between the SC and DC processing methods. The additional mass resulted in a slower cooling rate, allowing more time for the nuclei present in the melt to undergo crystallization.

It remains uncertain which of the two crystalline phases (1-1-2 and 3-2-4) grew first; they grew in conjunction with one another along the perimeter, where the cooling rate of the sample and the population density for both phases were at their maxima. For CGA-3, CGA-4, and CGA-5, it appeared that the three phases present were formed in the following order based on the direction of crystal growth: (1) the very outer rim was quenched into the amorphous state (fastest cooling rate), (2) very small 1-1-2 crystallites formed (slower cooling rate), and (3) the 3-2-4 crystallites grew off of 1-1-2 crystals (slowest cooling rate). As supercooling is possible in Cd-Ge-As materials,²² the temperature of the sample is thought to have been below the T_c for the 1-1-2 phase at the point of sample crystallization ($438^\circ\text{C} - 450^\circ\text{C}$ for CdGeAs₂).^{19,23} In CGA-3, CGA-4, and CGA-5, the composition of the interstitial amorphous phase between the 3-2-4 grains did not noticeably change radially from the 3-2-4. If the 3-2-4 grains propagated within the sample toward the center of the ingot through solid-state diffusion, the composition of the interstitial amorphous phase would change with Cd-deficient regions near the 3-2-4 crystals and a higher Cd concentration further removed from the 3-2-4 crystals.

The T_g and T_m of the residual glass phase present in these specimens after crystallization are presumed to have changed as the composition changed from the as-batched composition of 1-1-2 where $T_m \sim 665^\circ\text{C} - 670^\circ\text{C}$ and $T_g \sim 390^\circ\text{C}$.^{23,32,46,47} Both values are expected to have increased as x decreased in Cd _{x} GeAs₂ considering that the compound GeAs₂ ($x = 0$, or 0-1-2) has $T_m = 732^\circ\text{C}$.²⁰ However, we are not aware of any glass-formation work done in II-IV-V₂ (A^{II}B^{IV}C^V) materials deficient in the Group II component. A Cd-deficient Cd-Ge-As glass was found in all of the crystallized specimens. Thus, Cd _{x} GeAs₂ glasses where $x < 1$ might prove to be good glass-forming compounds that warrant further investigation.

According to the observations that were made for CGA-3, CGA-4, and CGA-5, the composition of the amorphous phase is 18–20 at.% Cd with the balance being GeAs₂ (Table IV). For CGA-6, the phases were dissimilar to those in the other samples and this was due to the different starting composition of Cd_{33.3}Ge_{22.2}As_{44.4} (3-2-4) versus Cd₂₅Ge₂₅As₅₀ (1-1-2). As a Cd-rich CdGeAs₂ phase is not stable in the amorphous state, the residual phases present after the 3-2-4 crystalline material was removed from the matrix were (1) a slightly As-deficient, Cd-doped GeAs₂ amorphous phase, (2) an As-rich phase with composition close to Cd₂Ge₃As_{11.3} (Cd₁₃Ge₁₉As₆₈), and (3) the CdAs-rich phase. The CdAs-rich phase was observed along the grain boundaries of the 3-2-4 crystals along the perimeter and in the bulk of the specimen in polished cross-sections.

VI. Conclusions

A new Cd-Ge-As phase was made with a double-containment ampoule method and the measured composition was Cd₃Ge₂As₄ (3-2-4). These crystals were made in large quantities through several similar experiments. These 3-2-4 crystals grow with a plate-like morphology and are presumed to nucleate from 1-1-2 crystals that appear first on the perimeter of the cylindrical ingot during the cooling process.

More work is needed to fully understand why these crystals form the structures presented here. At the current time the growth of the 3-2-4 crystals is thought to be facilitated by the DC quenching method that provides a specific cooling rate and a compressive force during the cooling process, forcing the solidified Cd-Ge-As ingot into a higher density state.

These materials have several potential applications as those identified for similar Cd-Ge-As compounds although measurements to validate these possibilities have yet to be realized due to the small size of the 3-2-4 crystallites. These applications include photoconductivity, semiconductivity, and nonlinear optics.

Acknowledgments

Pacific Northwest National Laboratory (PNNL) is operated for the U.S. Department of Energy by Battelle under Contract DE-AC05-76RL01830. This work was performed under contract with the Department of Energy's Nonproliferation and Verification R&D (NA-22) Program. Authors thank Clyde Chamberlin for his extensive work with specimen cutting and polishing. Authors also thank Carolyn Burns for running particle size analysis on the copper powder used in the DC experiments and Angus A. Rockett and Damon N. Hebert at the Materials Research Laboratory, located at the University of Illinois at Urbana-Champaign for helpful discussions and assistance in characterization. A portion of this research was performed using the Environmental Molecular Sciences Laboratory, a national scientific user facility sponsored by the Department of Energy's Office of Biological and Environmental Research and located at Pacific Northwest National Laboratory.

References

- S. Sharma, K. S. Hong, and R. F. Speyer, "Glass Formation in Chalcopyrite Structured Semiconducting Compounds," *J. Mater. Sci. Lett.*, **8** [8] 950-4 (1989).
- K. T. Stevens, L. E. Halliburton, S. D. Setzler, P. G. Schunemann, and T. M. Pollak, "Electron Paramagnetic and Electron-Nuclear Double Resonance Study of the Neutral Copper Acceptor in ZnGeP₂ Crystals," *J. Phys. Condens. Matter*, **15** [10] 1625-33 (2003).
- U. N. Roy, M. Groza, Y. Cui, A. Burger, Z. W. Bell, and D. A. Carpenter, "Crystal Growth, Characterization and Fabrication of AgGaSe₂ Crystals as a Novel Material for Room-Temperature Radiation Detectors"; pp. 177-80 in *Proc. of the SPIE*, Vol. 5540. Edited by A. Burger, R. B. James, and L. A. Franks. The International Society for Optical Engineering, Bellingham, WA, 2004.
- S. Cho, S. Choi, G. Cha, S. C. Hong, Y. Kim, Y. Zhao, A. J. Freeman, J. B. Ketterson, B. J. Kim, Y. C. Kim, and B. Choi, "Room-Temperature Ferromagnetism in (Zn_{1-x}Mn_x)GeP₂ Semiconductors," *Phys. Rev. Lett.*, **88** [25] 257203, 4pp (2002).
- B. R. Johnson, J. V. Crum, S. K. Sundaram, R. M. Van Ginhoven, C. E. Seifert, B. J. Riley, and J. V. Ryan, "DC Ionization Conductivity of Amorphous Semiconductors for Radiation Detection Applications," *IEEE Trans. Nucl. Sci.*, **56** [3] 863-8 (2009).
- G. A. Medvedkin, K. Hirose, T. Ishibashi, T. Nishi, V. G. Voevodin, and K. Sato, "New Magnetic Materials in ZnGeP₂-Mn Chalcopyrite System," *J. Cryst. Growth*, **236** [4] 609-12 (2002).
- Y. Zhao, S. Picozzi, A. Continenza, W. T. Geng, and A. J. Freeman, "Possible Impurity-Induced Ferromagnetism in II-Ge-V₂ Chalcopyrite Semiconductors," *Phys. Rev. B Condens. Matter*, **65** [9] 094411, 6pp (2002).
- R. L. Byer, H. Kildal, and R. S. Feigelson, "CdGeAs₂ - A New Nonlinear Crystal Phasematchable at 10.6 μm," *Appl. Phys. Lett.*, **19** [7] 237-40 (1971).
- G. D. Boyd, E. Buehler, F. G. Storz, and J. H. Wernick, "Linear and Nonlinear Optical Properties of Ternary A^{III}B^{IV}C₂^V Chalcopyrite Semiconductors," *IEEE J. Quantum Electron.*, **QE-8** [4] 419-26 (1972).
- R. L. Byer, "Optical Parametric Oscillators"; pp. 587-702 in *Quantum Electronics: A Treatise*, Edited by H. Rabin and C. L. Tang. Academic Press, New York, 1977.
- P. G. Schunemann and T. M. Pollak, "Single Crystal Growth of Large, Crack-Free CdGeAs₂," *J. Cryst. Growth*, **174** [1-4] 272-7 (1997).
- H. Katzman, T. Donohue, W. F. Libby, H. L. Luo, and J. G. Huber, "A High-Pressure Superconducting Polymorph of Cadmium Tin Diarsenide," *J. Phys. Chem. Solids*, **30** [6] 1609-11 (1969).
- K. L. Vodopyanov and P. G. Schunemann, "Efficient Difference-Frequency Generation of 720-μm Radiation in CdGeAs₂," *Opt. Lett.*, **23** [14] 1096-8 (1998).
- V. Rud, Y. Rud, I. Polushina, T. Ushakova, and S. Iida, "Observation of Record Electron Hall Mobility in CdGeAs₂ Single Crystals," *Jpn. J. Appl. Phys.*, **39**, 266-7 (2000).
- T. S. Moss, "A Relationship Between the Refractive Index and the Infra-Red Threshold of Sensitivity for Photoconductors," *Proc. Phys. Soc. B*, **63** [3] 167-76 (1950).
- H. Katzman, T. Donohue, W. F. Libby, and H. L. Luo, "A High-Pressure Superconducting Polymorph of Cadmium Germanium Diarsenide," *J. Phys. Chem. Solids*, **30** [12] 2794-5 (1969).
- G. W. Iseler, H. Kildal, and N. Menyuk, "Optical and Electrical Properties of CdGeAs₂," *J. Electron. Mater.*, **7** [6] 737-55 (1978).
- B. R. Johnson, B. J. Riley, J. V. Crum, S. K. Sundaram, C. H. Henager Jr., D. L. Edwards, and A. L. Schemer-Kohrn, "Discovery of Metastable Crystalline Phases in Cd-Ge-As Glass," *J. Am. Ceram. Soc.*, **91** [2] Cover (2008).
- B. R. Johnson, B. J. Riley, S. K. Sundaram, J. V. Crum, C. H. Henager Jr., Y. Zhang, V. Shutthanandan, C. E. Seifert, R. M. Van Ginhoven, C. E. Chamberlin, A. A. Rockett, D. N. Hebert, and A. R. Aquino, "Synthesis and Characterization of Bulk, Vitreous Cadmium Germanium Arsenide," *J. Am. Ceram. Soc.*, **92** [6] 1236-43 (2009).
- M. Hansen and K. Anderko, *Constitution of Binary Alloys*. 2nd ed, pp. 1305. McGraw-Hill Book Company, Inc., New York, 1958.
- A. S. Borshchevskii, N. A. Goryunova, F. P. Kesamanly, and D. N. Nasledov, "Semiconducting A^{III}B^{IV}C₂^V Compounds," *Phys. Status Solidi B*, **21** [1] 9-55 (1967).
- A. S. Borshchevskii and N. D. Roenkov, "Phase Diagram of the Cadmium-Germanium-Arsenic System," *Russ. J. Inorg. Chem.*, **14** [8] 1183-6 (1969).
- K. S. Hong, Y. Berta, and R. F. Speyer, "Glass-Crystal Transition in II-IV-V₂ Semiconducting Compounds," *J. Am. Ceram. Soc.*, **73** [5] 1351-9 (1990).
- J. C. Mikkelsen Jr and H. Y.-P. Hong, "Cd₂GeAs₄: A New Ternary Phase in the Cd-Ge-As System," *Mat. Res. Bull.*, **9** [9] 1209-18 (1974).
- B. R. Pamplin and R. S. Feigelson, "New Phases in the Cd-Ge-As System," *Mat. Res. Bull.*, **14** [2] 263-6 (1979).
- K. T. Zawilski, P. G. Schunemann, and T. M. Pollak, "Glass Formation and Optical Properties of CdGeAs₂ Alloys," *J. Cryst. Growth*, **310** [7-9] 1897-903 (2008).
- P. G. Schunemann and T. M. Pollak, "Ultralow Gradient HGF-Grown ZnGeP₂ and CdGeAs₂ and Their Optical Properties," *Mater. Res. Bull.*, **23** [7] 23-7 (1998).
- J. L. Shay and J. H. Wernick, *Ternary Chalcopyrite Semiconductors: Growth, Electronic Properties, and Applications*. Pergamon Press, New York, 1975.
- H. Kildal, "CdGeAs₂ and CdGeP₂ Chalcopyrite Materials for Infrared Nonlinear Optics"; Ph.D. dissertation Thesis, Stanford University, Stanford, CA, 1972.
- K. Nagashio, A. Watcharapasorn, K. T. Zawilski, R. C. DeMattei, R. S. Feigelson, L. Bai, N. C. Giles, L. E. Halliburton, and P. G. Schunemann, "Correlation Between Dislocation Etch Pits and Optical Absorption in CdGeAs₂," *J. Cryst. Growth*, **269** [2-4] 195-206 (2004).
- S. M. Evans, N. Y. Garces, R. C. DeMattei, R. S. Feigelson, K. T. Zawilski, N. C. Giles, and L. E. Halliburton, "Electron Paramagnetic Resonance and Electron-Nuclear Double Resonance Study of Mn²⁺ Ions in CdGeAs₂ Crystals," *Phys. Status Solidi B*, **243** [15] 4070-9 (2006).
- P. Leroux-Hugon, "Properties of Some Ternary Semiconductor Compounds," *C.R. Hebd. Seances Acad. Sci. (France)*, **256** [1] 118-20 (1963).
- B. R. Pamplin, T. Kiyosawa, and K. Masumoto, "Ternary Chalcopyrite Compounds," *Prog. Crystal Growth Charact.*, **1** [4] 331-87 (1979).
- G. Lianxing, Z. Bing, and Z. Wenlan, "Chalcopyrite Intergrowths in Sphalerite in the Meixian Lead-Zinc Deposit, Fujian Province and Their Metallogenic Significance," *Chin. J. Geochem.*, **17** [4] 311-9 (1998).
- B. J. Riley, B. R. Johnson, S. K. Sundaram, M. H. Engelhard, R. E. Willford, and J. D. Olmstead, "Pressure-Temperature Dependence of Nano-wire Formation in the Arsenic-Sulfur System," *Phys. Chem. Glass*, **47** [6] 675-80 (2006).
- A. A. Vaipolin, F. M. Gashimzade, N. A. Goryunova, F. P. Kesamanly, D. N. Nasledov, E. O. Osmanov, and Y. V. Rud, "Investigation of the Physicochemical and Electric Properties of Crystals of Some Ternary Semiconductor Compounds of the A^{III}B^{IV}C₂^V Type," *Izv. Akad. Nauk SSSR Ser. Fiz. (USSR)*, **28** [6] 1085-9 (1964).
- N. A. Goryunova, F. P. Kesamanly, and E. O. Osmanov, "Preparation and Some Properties of CdGeAs₂ Single Crystals," *Fiz. Tverd. Tela (USSR)*, **5** [7] 2031-2 (1963).
- H. Hruby, "Evaluation of Glass-Forming Tendency by Means of DTA," *Czech J. Phys.*, **B22** [11] 1187-93 (1972).
- T. A. Hahn, "Standards, Copper, Methods, Thermal Expansion of Copper from 20 to 800 K—Standard Reference Material 736," *J. Appl. Phys.*, **41** [13] 5096-101 (1970).
- SRM-736, *Copper-Thermal Expansion*. National Institution of Standards and Technology, Gaithersburg, MD, 1990.
- SRM-739, *Fused-Silica Thermal Expansion*. National Institute of Standards and Technology, Gaithersburg, MD, 1991.
- H. Pfister, "Kristallstruktur von ternären Verbindungen der Art A^{III}B^{IV}C₂^V," *Acta Cryst.*, **11**, 221-4 (1958).
- M. J. Duggin, "The Thermal Conductivity of Liquid Gallium," *Phys. Lett.*, **29A** [8] 470-1 (1969).
- M. L. V. Ramires, C. A. Nieto de Castro, Y. Nagasaka, A. Nagashima, J. Assael, and W. A. Wakeham, "Standard Reference Data for the Thermal Conductivity of Water," *J. Phys. Chem. Ref. Data*, **24** [3] 1377-81 (1995).
- R. W. Powell, C. Y. Ho, and P. E. Liley, "Thermal Conductivity of Selected Materials"; 165 pp. in *National Standard Reference Data Series-National Bureau of Standards, Category 5-Thermodynamic and Transport Properties*, Vol. 8. U.S. Department of Commerce, Washington, D.C., 1966.
- M. J. Harrison, A. P. Graebner, W. J. McNeil, and D. S. McGregor, "Carbon Coating of Fused Silica Ampoules," *J. Cryst. Growth*, **290** [2] 597-601 (2006).
- S. H. Risbud, "Processing and Properties of Some II-IV-V₂ Amorphous and Crystalline Semiconductors," *Appl. Phys. A*, **62** [6] 519-23 (1996). □

Kelvin probe force microscopy of metal contacts on amorphous cadmium germanium arsenide

Damon N. Hebert, Allen J. Hall, Angel R. Aquino, Angus A. Rockett
University of Illinois, Materials Science & Engineering Department
Urbana, IL

Richard T. Haasch
University of Illinois, Frederick Seitz Materials Research Laboratory
Urbana, IL

Bradley R. Johnson, Brian J. Riley
Pacific Northwest National Laboratory, Glass Science & Processing
Richland, WA

8.1 ABSTRACT

Au and Al/Mg bilayers have been studied as possible contacts to amorphous CdGe_{0.65}As₂ (CGA) semiconductors. Kelvin probe force microscopy (KPFM) and ultraviolet photoelectron spectroscopy (UPS) were used to measure the contact potential difference between these metals and an amorphous bulk CGA sample. Au was found to have a contact potential difference of -500 meV relative to the CGA by KPFM and -780 meV by UPS. The bilayer contact with Al on Mg on CGA showed a 400 meV contact potential difference from the Al to the CGA based on KPFM. The contact of Mg to CGA should be about 500 meV higher due to the contact potential difference between Mg and Al. The contact potential difference for Mg/CGA estimated from UPS was 700 meV. Electrical measurements showed that the conductivity of our CGA exhibits a thermally-activated behavior with an activation energy of 520 meV. The bilayer contact should have yielded a Schottky type contact for both the measured and anticipated contact potential difference, although the temperature-dependent current/voltage curves showed the

behavior to be ohmic for all temperatures studied. Other contact metals were also tested and they did not produced effective Schottky contacts either, possibly due to interfacial reactions or second phases not detected in the CGA. However, the range of metals tested, the absence of second phases in the XRD, the low conductivity of the CGA and the consistent electric field observed from the contacts to the CGA with high resolution of the KPFM measurements tends to suggest that the contact was a Schottky barrier over most of its area but that some form of undetectable region caused a low-resistance contact.

8.2 1. Introduction

In crystalline form, the CdGe_xAs_2 (CGA) semiconducting chalcopyrite compound and related materials are of interest in energy conversion applications and as infrared nonlinear optical materials.^{1,2} Novel processing approaches provide the possibility of amorphous-crystalline p-n junctions.³ These compounds, as well as other similar II-IV-V₂ chalcopyrite materials, are known to exhibit behaviors useful for nonlinear optics, switching, radiation detection and photovoltaic device applications.⁴⁻⁶ For radiation detection purposes, a reproducible low-leakage Schottky barrier contact is desirable because under high bias fields, the device dark current can exceed the signal generated by low-levels of ionizing radiation. For example, it is often necessary to be able to detect nA-level signals at bias fields of ~ 1000 V/cm. Therefore, fabrication of reproducible Schottky contacts to amorphous CGA is required for the material to be employed as the active sensing material in a radiation detection device.

This work reports on the fabrication of two types of metal/CGA contacts and their analysis with contact potential differences as measured by Kelvin probe force microscopy (KPFM) and work functions as measured by ultraviolet photoelectron spectroscopy (UPS). KPFM is a non-contact atomic force microscopy (AFM) method that measures the contact potential difference (CPD) between the surface of the sample and the conductive AFM tip resulting from changes in the vacuum level. This is equivalent to the difference between the work function of the AFM tip (ϕ_{tip}) and the work function of the specimen surface (ϕ_{sc}), $CPD = (\phi_{tip} - \phi_{sc})/q$, where q is the elementary charge. KPFM has been used, for example, to study the surface potential of chalcopyrite thin films⁷ and lateral Ni/AlGaN Schottky junctions⁸ as well as to observe surface charging at the edge of metal/GaN Schottky contacts.⁹ In this study, contact behavior was also analyzed with temperature dependent current-voltage (I-V) measurements with three different contact configurations. I-V and capacitance-voltage (C-V) curves have previously been used to characterize Al-based Schottky contacts on chalcopyrite I-III-VI₂ semiconductors,¹⁰ but never before on amorphous CGA compounds.

For a semiconductor, the work function is just the sum of the electron affinity, χ_{sc} , and the separation between the Fermi energy level (E_F) and the conduction band (E_c), $E_a = E_c - E_F$. Therefore the work function of a semiconductor depends on its doping and the position of the Fermi level. This study reports work functions of electron-beam evaporated Au films and of the CGA sample itself characterized with UPS. Finally, X-ray photoelectron spectroscopy (XPS) was used to determine the position of the Fermi level.

In preliminary (unpublished) experiments, several metals were studied as possible CGA contacts with varying work functions (ϕ). Au ($\phi = 5.10$ - 5.47 eV), Pt ($\phi = 5.65$ - 5.70 eV), Ni ($\phi = 5.04$ - 5.35 eV), Ti ($\phi = 4.33$ eV), Ag ($\phi = 4.26$ - 4.74 eV), Mg ($\phi = 3.66$ eV), and Al ($\phi = 4.06$ -

4.41 eV)¹¹ were all used. Although diode-like behavior was observed in one particular case (Mg – CGA – Mg contact configuration), the lack of reproducibility called for a more organized study and was the motivation for the current work.

Au and Al/Mg were chosen as candidate contacts for KPFM analysis because Au has a high work function (5.10-5.47 eV) and Mg has a low work function (3.66 eV). Al was used as a capping metal on the Mg to prevent post-deposition oxidation and because Al also has a relatively low work function (4.06-4.41 eV).¹¹ Thus, based on the expected work function of CGA and its small mobility gap (0.65-1.1 eV),¹² one metal contact should have produced a Schottky barrier and the other an ohmic contact regardless of the (intrinsic) doping type of the CGA.

8.3 2. Experiment

2.1 Material and Contact Fabrication

CGA glass samples of the composition $\text{CdGe}_{0.65}\text{As}_2$ were synthesized by water quenching molten liquids enclosed in double containment ampoules to form bulk, vitreous, crack-free ingots. Details of the fabrication process and subsequent characterization are published elsewhere.¹² As explained in Reference 12, CGA is a fragile glass forming system. Consequently, candidate samples selected for KPFM analysis in this study were screened by cross-polarized reflected light microscopy and X-ray diffraction to ensure that they were uniformly amorphous. For the sample chosen for study by KPFM analysis, X-ray diffraction showed it to be amorphous, although pair correlation function analysis revealed a high degree of short range order out to the 4th nearest neighbor.¹² The specimen had a bulk composition of $\text{Cd}_{1.00}\text{Ge}_{0.65}\text{As}_{2.00}$. Compositional analysis performed on similar specimens with particle induced

X-ray emission (PIXE), Rutherford backscattering spectroscopy (RBS), and secondary ion mass spectroscopy (SIMS) confirmed that the actual stoichiometry was uniform on scales measured by SIMS and matched the intended “as-batched” stoichiometry.¹² The sample mounted for KPFM was polished in a vibratory polisher with 1- μm diamond polish and cleaned in an ultrasonic cleaner. It was polished a second time with colloidal silica polish solution. All specimens were cleaned with acetone, isopropanol and de-ionized water and dried with nitrogen gas immediately before contact deposition and before KPFM analysis.

The Au/CGA contacts and Al/Mg/CGA bilayer contacts were deposited with a Temescal electron-beam evaporation system on several CGA samples. Typical contact thicknesses were 60-80 nm, with the Al/Mg bilayer thicknesses approximately 25 ± 5 nm Al on top of 45 ± 5 nm of Mg, with deposition rates of 0.05-0.15 nm/s. Contacts were approximately 0.8 mm in diameter. For I-V curve measurements, contacts were spaced in a Van der Pauw geometry, 3-10 mm apart, around the periphery of ~ 10 mm diameter, disc-shaped bulk CGA substrates. However, for KPFM analysis, contact edges were required to be more abrupt than the 0.8 mm diameter contacts used for I-V curve analysis. Therefore, patterned Au/CGA and Al/Mg/CGA contacts were deposited with transmission electron microscopy grids (SPI 2030N; 3 mm, 300 mesh, Ni) as shadow masks on the chosen CGA specimen for KPFM analysis. The masking procedure led to high contrast regions of metal on the CGA spaced by 25 μm (Figure 1).

2.2 Ultraviolet photoelectron spectroscopy (UPS) and X-ray photoelectron spectroscopy (XPS)

Surface work functions were measured with *in situ* UPS and spectra were acquired by means of a Physical Electronics PHI 5400 photoelectron spectrometer utilizing He I (21.2 eV) ultraviolet radiation as the excitation source. The UPS source was incident at an angle of 50°

while the electron detector had an acceptance angle of 20° . The UPS data were collected at an emission angle of 0° relative to the surface normal. Prior to UPS measurements, the Au and CGA samples were sputtered for 30 seconds with 3 keV Ar^+ rastered over a $3 \times 3 \text{ mm}^2$ ($10 \mu\text{A}/\text{cm}^2$) area to remove surface contamination. Alignment of the Fermi level with the valence band edge (and thus doping type) of the CGA sample was examined with a Kratos Axis ULTRA high-performance X-ray photoelectron spectrometer with a monochromatic Al $K\alpha$ (1486.7 eV) excitation source. For these techniques, spectral information was collected from a depth of 2-20 atomic layers, depending on the photoelectron escape depth (material dependent).

2.3 Kelvin probe force microscopy

An Asylum Research MFP3D AFM was used to measure surface topography (AC mode) and contact potential difference (KPFM, Nap mode), simultaneously, with a BudgetSensors ElectriTap 300 Pt/Cr (25/5 nm) monolithic Si probe tip (BudgetSensors, Bulgaria). Samples were measured in ambient air conditions. Scan speeds of approximately $11 \mu\text{m}/\text{s}$ were used to ensure good tip-surface tracking and no bias voltage was applied to the tip during Nap-mode (KPFM) scans. Data were acquired and analyzed with Asylum MFP3D software in IGOR Pro (Asylum Research, Santa Barbara, CA, USA).

8.3.1 *2.4 Electrical Measurements*

Current-voltage curves were measured as a function of sample temperature with the same contact materials (Au and Al/Mg) as were measured in the KPFM scans. Four-point probe measurements on the CGA samples were performed with linearly-aligned contacts spaced 2 mm apart. Samples were housed in a sealed, evacuated sample chamber and mounted with Apiezon L grease (M&I Materials Ltd., Manchester, UK) to a cold stage. The cold stage was cooled

using a CTI Cryogenics 8200 compressor with a temperature range of 40 to 300 K. A Lakeshore 330 autotuning temperature controller (Lakeshore Cryotronics, Inc., Westerville, OH, USA) with a TG-120-PL GaAlAs temperature sensor and a resistive heating element in the cold stage were used to maintain the specified sample temperature. An MMR H-50 Hall/Van der Pauw controller (MMR Technologies, Mountain View, CA, USA) was used to apply and measure currents and voltages through the sample. Electrical contact from the Hall/Van der Pauw controller to the specimen was accomplished by cold-soldering indium-coated platinum wires to the electron beam evaporated contacts. Data was acquired with a custom LabView program.

8.3.2 3. Results and Discussion

8.3.3 3.1 Ultraviolet photoelectron spectroscopy (UPS) and X-ray photoelectron spectroscopy (XPS)

Ultraviolet photoelectron spectroscopy was used to measure the work functions of the surfaces of the CGA sample and the Au contact and these results are plotted in Figure 2. An accelerating potential was used to separate the secondary edges of the sample and analyzer, which allows for an accurate determination of the position of the secondary edge of the sample, and hence the work function. In the UPS spectrum, the work function is the difference between the energy of the ultraviolet photons ($h\nu = 21.2$ eV for He I radiation) and E_b , the binding energy of the secondary edge. The secondary edge is the maximum binding energy found for photons in the spectrum and represents the minimum kinetic energy for photoelectron escape from the surface. The location of the secondary edge is fit experimentally in various ways in practice;^{13,14} we chose to fit the edge with a Gaussian-Lorentzian peak and record the location of the secondary edge to be one half-width at half maximum toward the higher binding energy side of

the edge. This gave values of $\phi_{\text{Au}} = 5.15$ eV and $\phi_{\text{CGA}} = 4.37$ eV, a difference of 780 meV. The measured work function value we obtained for Au is in excellent agreement with a value obtained by KPFM on a similar Au sample of $\phi_{\text{Au}} = 5.2$ eV measured relative to SrTiO₃ and Cu₂O.¹⁵

With XPS, we determined that the valence band edge in the CGA was offset by +0.53 eV with respect to the Fermi level of the Au. Based on the measured work functions from UPS, we can calculate that the Fermi level of the CGA sits 0.25 eV above its valence band edge. This indicated that the CGA sample was p-type, in agreement with hot point probe measurements.

The mobility gap in CGA was characterized previously by optical absorption spectroscopy and ellipsometry.¹² The onset of the mobility edge above the background subgap absorption (for samples with the same composition used in this experiment) began at 0.65 eV and appeared to converge to a band-like behavior at approximately 1.1 eV.¹² With information from UPS, XPS and the mobility gap, the electron affinity of the CGA was calculated to be 3.52 eV.

The Mg and Al contacts were not tested in the UPS or XPS because their work functions vary with surface conditions much less than for Au, and so the literature values for work function, 3.66 eV and 4.06-4.41 eV, respectively, were used. Based on the electron affinity of CGA, calculated above, we conclude that we should have obtained an ohmic contact between Au and CGA and a Schottky contact with a contact barrier height of ~700 meV between the CGA and the Mg. A summary of measured and calculated values is shown in Figure 3.

8.3.4 3.2 Kelvin probe force microscopy

The sample and associated contact metals were measured by KPFM. Many factors can influence the KPFM-measured contact potential difference (CPD) and lead to a change in work function at a surface, including adsorption of gas atoms, relaxation or reconstruction of surfaces, differences in crystallographic faces, built up charge on the surface, surface photovoltage, induced surface-dipoles, and tip conditions.¹⁶ As a result, comparisons within individual KPFM measurements are more reliable than comparisons between two different sample measurements. Thus the current study examined metal layers directly on a CGA sample, with measurements across the metal-CGA junction.

Areas that included relatively abrupt edges of both contact materials were analyzed with AFM and KPFM. Figures 4(a) and (b) present surface topography (greyscale) and contact potential difference (CPD) (color overlay) for the two contacts studied. Au/CGA edges were typically much sharper than Al/Mg/CGA edges in both topography and contact potential difference. Away from the contact edge, the roughness of the bare CGA and metal contact are significant with respect to the contact edge thickness itself; however, the CPD signal did not vary significantly with topography away from the contact edge. The minimum CPD on these 3D images is set to zero by the MFP3D software, so the CPD is a relative value for each scan. Figures 4(c) and (d) give corresponding linescans across metal/CGA edges based on the data in Figures 4(a) and (b). The linescans are averages of approximately 30 neighboring traces spaced 0.1 μm apart.

Table I gives the relevant CPD values and contact edge height differences, Δz , along with measured values from UPS and XPS. Each CPD is an areal root-mean squared average over a 3-6 μm^2 portion of a 15 \times 15 μm KPFM scan. We found that the CPD of the CGA substrate varied

with location. It depended on proximity to a metal contact and on the type of metal contact that was neighboring the CGA during the CPD measurement. Specifically, the CPD for CGA varied from as low as 404 ± 17 mV near Au contacts to as high as 818 ± 11 mV near Al/Mg contacts. CPD values for bare CGA, not near any contact metal (at least $1000 \mu\text{m}$ from any contact) were in the range of 571 ± 12 mV. Therefore, two ΔCPD values are reported, one for the change in CPD across the edge in the immediate vicinity of the contact ($\Delta\text{CPD}_{\text{edge}}$) and one for the difference between the metal CPD and the bare, isolated CGA CPD ($\Delta\text{CPD}_{\text{long range}}$). We suggest that $\Delta\text{CPD}_{\text{long range}}$ represents the real work function differences between the metal contacts and the CGA, as opposed to $\Delta\text{CPD}_{\text{edge}}$ which includes the local influence of the metal.

For the Au contact, the CPD decreased by an average of $\Delta\text{CPD}_{\text{long range}} = 500$ mV as the tip went from bare CGA to Au. This measurement is considerably lower than the work function difference of 780 meV measured by UPS but is within experimental error, due in part to air exposure of the surfaces studied by KPFM and due to sputter cleaning of the surfaces studied by UPS/XPS. Despite these uncertainties, we can conclude that work function of the CGA is in the range of $\sim 450\text{-}800$ meV less than that of Au, and given this we should expect an ohmic contact. The corresponding contact band edge diagram is shown schematically in Figure 3.

For the Al/Mg contact, the CPD *increased* by an average of $\Delta\text{CPD}_{\text{long range}} = 410$ mV as the tip went from bare CGA to Al. We have two ways to calculate ϕ_{Al} . Using the UPS-measured $\phi_{\text{CGA}} = 4.37$ eV, we calculate that $\phi_{\text{Al}} = 4.37 - 0.41 = 3.96$ eV. The KPFM measurements for $\Delta\phi$ between Au and Al was 910 meV, yielding $\phi_{\text{Al}} = 4.24$ eV. The average of the two values for ϕ_{Al} from the KPFM here are in good agreement with the literature range of 4.06-4.41 eV for Al. The CGA is in contact with Mg ($\phi = 3.66$ eV) and not the exposed Al capping layer, measured in KPFM. Therefore we expect that the Mg/CGA would have a ΔCPD

0.3 to 0.6 eV greater than does the Al/CGA interface (see schematic band edge diagrams in Figure 3). Therefore we expect ϕ_{Mg} to be ~ 0.7 eV below ϕ_{CGA} . In any case, we expect both Al and Mg to produce Schottky barrier contacts, although the Mg/CGA barrier height should have been much higher.

The morphological widths of the interfaces were $0.32 \pm 0.15 \mu\text{m}$ for the Au contact and $2.60 \pm 0.15 \mu\text{m}$ for the Al/Mg contact as judged from the point where the metal/CGA edge began to decrease down to the point where the topography flattened out on the CGA side. This longer interfacial width for the Al/Mg contact was most likely due to lateral surface self-diffusion of the metal layers under the TEM grid mask during electron beam evaporation. Atoms arriving from the vapor phase provide thermal energy to the metal surface ($50\text{-}60^\circ\text{C}$) during the deposition, allowing for modest surface self-diffusion. In general, the surface diffusion coefficient of metals increases with increasing homologous temperature (T_H), the ratio of the temperature of a metal surface to its melting point.¹⁷ Therefore, surface self-diffusion is expected to be lower for Au ($T_H = 0.24$) than for Mg ($T_H = 0.36$) or Al ($T_H = 0.35$).

The width of the interface in terms of the potential was found in a similar way by plotting the derivative of the potential with respect to distance (not shown). The CPD interface width was $1.96 \pm 0.2 \mu\text{m}$ for the Au contact and $5.4 \pm 1.0 \mu\text{m}$ for the Al/Mg contact. The inflection points for CPD and topography in the derivative plots occur at the same position for both contact types, indicating that the CPD change is directly related to the contact edge location.

It is possible that the width, w , of carrier depletion around a metal/CGA interface extended laterally into the volume of CGA material and was responsible for the more gradual change in CPD as compared to the change in topography across the contact edge. The expected depletion width in a metal/semiconductor junction can be estimated by using a p^+-n

approximation; that is, by assuming the charge in the metal is sufficient to produce essentially no depletion in the metal and that the carrier concentration in the metal is much greater than that in the CGA, which we have measured to be very small as discussed above.¹⁸ In this case the depletion width extends only into the semiconductor side of the junction and is described by

$$w = \sqrt{\frac{2\varepsilon V_0}{qN_a}},$$

where ε is the permittivity of the CGA, V_0 is the contact potential, and N_a is the acceptor concentration in the p-type CGA. V_0 is directly measured in the KPFM; it is the difference in work functions between the metal and CGA. N_a is estimated to be $6 \times 10^{13} \text{ cm}^{-3}$ from room temperature resistivity data of the CGA ($\sim 10^5 \text{ } \Omega\text{-cm}$) and an estimate of its hole mobility ($\mu_p \sim 1 \text{ cm}^2/\text{Vs}$) taking that of *a*-Si as roughly comparable. The permittivity, ε , is projected to be $15\varepsilon_0$.¹⁹ This estimation led to values of $w = 3.6 \text{ } \mu\text{m}$ for Au contacts and $w = 4.9 \text{ } \mu\text{m}$ for Al/Mg contacts. This calculation predicts that, regardless of the particular values of semiconductor parameters chosen, the Al/Mg contact produces a wider depletion width than the Au contact by the factor

$$\frac{w_{Mg/Al}}{w_{Au}} \propto \sqrt{\frac{V_{0,Mg/Al}}{V_{0,Au}}}.$$

The modeled ratio is 1.4 using V_0 as measured by KPFM. The measured ratio from analysis of linescans was $5.4/1.96 = 2.76$ (but within error can range as low as 2.04). Although rudimentary, this approximation shows that the measured CPD interface width in KPFM agrees at least qualitatively with what would be expected for a metal/CGA depletion width extending laterally into the CGA material. Note that if the shape of the CPD change across the metal/CGA edge were due entirely to a $p^+ \text{-n}$ depletion width as described above, we would expect to observe completely asymmetric potential spreading, only on the CGA side. However, the KPFM data show some degree of symmetry, although the CPD change is less sharp on the CGA side for both

contact types. This is likely because the CPD is a superposition of the effect of topography (giving rise to symmetry) and the depletion into the CGA side (giving rise to asymmetry).

3.3 Electrical Measurements

Electrical measurements were performed on a number of metal/CGA combinations including CGA samples with a wide range of Ge contents (CuGe_xAs_2 with $x=0.45, 0.65, 0.85,$ and 1.00). Here, we describe in detail those measurements for the KPFM-analyzed specimen. The other metal/CGA combinations behaved similarly.

Four-point probe measurements on the CGA samples were used to characterize the conductivity as a function of temperature, as shown in Figure 5. The data fit well with a Boltzmann distribution resulting in an activation energy for conduction in the sample of 0.52 eV, consistent with activation of carriers from midgap states into the corresponding bands.

Temperature dependent current-voltage (I-V) curves were measured for three specific contact configurations: between two Au contacts, between two Al/Mg contacts, and from one type of contact to the other. Representative log-I-V curves at various temperatures are shown in Figure 6 for the Al/Mg-CGA-Au contact configuration. As the sample temperature dropped below 220 K, resistivities became so large that our system was not able to drive measurable current through the samples. For the three contact configurations, I-V curves were linear in both directions of current flow, showing no rectifying behavior throughout the temperature range measured. Arrhenius plots were made of conductivity vs. inverse temperature for each contact configuration, and were fitted with an exponential function to calculate the activation energy for electrical conduction (Table II). These values were in reasonable agreement with the activation energy determined from the four-point probe measurement. This indicates that the resistance of

the conduction path for all contact combinations was mostly due to the CGA itself and not due to either of the contact types.

Based on the sample geometry, the expected series resistance of a given current path can be calculated. Furthermore the contact resistances based on the standard Schottky diode thermionic emission model can be estimated to determine if the resistance should be dominated by the expected Schottky barriers.²⁰ For a Schottky diode the current I at bias voltage V is given by

$$I = I_0 \left(e^{qV/nkT} - 1 \right)$$

where

$$I_0 = A^* AT^2 \exp(-q\Phi / k_B T),$$

and A^* is the effective Richardson constant, A is the diode area, $k_B T/q$ is the thermal voltage, n is the diode ideality factor and Φ is the Schottky barrier height. Ay et al.²¹ report experimental Richardson constants in a wide range of 0.341-438 A/m²K² for *a*-Si:H/Au Schottky barriers. Hull et al.²² report $A^* = 782$ A/m²K² for *c*-Ge and *a*-Ge Schottky barriers. Here we chose values of $A^* = 100$ and 500 A/m²K² as representative values. The resulting estimates of contact properties for the KPFM-measured Schottky barrier heights are given in Table III, for given T , Φ and A^* . Table 3 gives the reverse voltage (V_t) at which the series resistance of the CGA material matches that of an ideal Schottky barrier in reverse bias. Since every value of V_t is less than 1 V, we conclude that the voltage range used in this experiment (± 2 V) is adequate to measure the possible effect of a Schottky barrier between CGA and Mg (or Au). Variation of A^* within the range reported for other amorphous semiconductor-metal pairs does not change this conclusion. A non-ideal diode ($n=2$) would require more voltage to drive a given current through the Schottky diode so non-ideal behavior does not account for the difference. Although a Schottky contact would be expected for the Mg contacts on p-type CGA, the contacts made in this

experiment were not Schottky-like or were highly imperfect and did not contribute significantly to impeding the current when compared with the resistance of the CGA material itself. Other contact metals were also tested, including Ni, Al, and Pt, for each of the CuGe_xAs_2 alloy compositions $x=0.45, 0.65, 0.85$ and $x=1$, yet nothing was found that yielded a Schottky contact on amorphous CGA at temperatures from 300 K to as low as 220 K. The exception was one set of contacts measured between two sets of Mg/Al contacts, which should have appeared resistive. Therefore we conclude that measurement was affected by local non-uniformities in the CGA in that sample that were undetectable by the methods used here.

4. Conclusions

Kelvin probe force microscopy measurements of Au and Al/Mg contacts to a bulk amorphous CGA sample show contact potential differences consistent with the work function difference of the metals. UPS was used to measure the work functions of Au $\phi_{\text{Au}} = 5.15$ eV and of the CGA $\phi_{\text{CGA}} = 4.37$ eV. XPS was used to measure the valence band offset of the CGA with respect to the Fermi level of Au. These measurements led to a schematic band diagram of the CGA in contact with the metals chosen. We conclude that work function of the CGA is in the range of $\sim 450\text{-}800$ meV less than that of Au, and given this we should expect an ohmic contact.

The electron affinity of the CGA was calculated to be 3.52 eV. A work function difference of 0.70 eV for CGA/Mg contacts was measured, which we expected to result in a Schottky contact. The behavior of the CPD around the edges of the contacts was interpreted in terms of the formation of a depletion region around the contact and diffusion of Al and Mg atoms during deposition, but the region affected by the metal appears to extend far beyond the range of normal depletion. The CPD from the CGA to the metals puts the work function of this CGA sample roughly midway between the two metals. Given the work function difference and

the mobility gap in the CGA, the Mg/Al contacts should have yielded a relatively high Schottky barrier and a highly resistive contact for one bias direction. The Au contact should have yielded an ohmic contact. However, electrical measurements show no diode-like behavior for any combination of contacts measured. The resistance of the circuit from any contact to any other was consistent with the resistance of the CGA material itself at the measurement temperature. The temperature dependencies of CGA with different electrode contact metals also followed the same behavior as CGA without an electrode. We conclude that these materials did not produce a Schottky contact on the CGA sample studied despite contact potential differences that should have yielded a good Schottky contact. This result is not specific to the sample or metals measured and we have not obtained a reproducible Schottky contact on any CGA sample using any metal.

Although we could not measure any local variations in conduction in the CGA as a function of position we propose that local inhomogeneities on a scale less than what could be measured with the KPFM or XPS/UPS led to local ohmic contacts to the metals in all cases. This could be the case based on local short-range order suggested by the XRD. Any larger patch of material with high conductivity could have yielded an ohmic contact behavior if the area of those patches were sufficient to carry the currents used here. However, we note that if these areas were common enough to cause all contacts to appear ohmic we would have expected to observe them with the KPFM. If they are common but too small to be distinguished with the KPFM we should have observed variations in potential across the surface or very little depletion region. If there were an interfacial reaction under the contact that was unobservable with the techniques used here we would have expected one of the various metals on one of the various

compound compositions to yield a diode-like behavior. Therefore we are unable to explain the lack of diode-like current voltage curves in our measurements.

8.4 Acknowledgements

This work was supported by the U.S. Department of Energy, Office of Nonproliferation Research and Development (NA-22). Pacific Northwest National Laboratory is operated for the U.S. Department of Energy by Battelle Memorial Institute under Contract No. DE-AC05-76RLO1830. Materials analysis was carried out in the Frederick Seitz Materials Research Laboratory Central Facilities at the University of Illinois which are partially supported by the College of Engineering. The authors thank Scott MacLaren for his work in scanning probe microscopy, the group of Dr. Jim Eckstein for lending cryogenic wiring and varnish, Dr. Julio Soares for helping with the setup of the I-V curve station and LabView programming, and Laura Burka and Clyde Chamberlin for their help in preparing the samples.

Table I. KPFM and UPS/XPS data summary

Contact edge	KPFM					UPS	XPS
	Δz (nm)	area	CPD (meV)	$\Delta\text{CPD}_{\text{edge}}$ (meV)	$\Delta\text{CPD}_{\text{long range}}$ (meV)	$\Delta\phi$ barrier height (meV)	ΔVBE (meV)
Au	72.0±1.1	CGA	404±17	-333±24	-500	780	530
		Au	71±24				
Al/Mg	75±12	CGA	818±11	166±17	413	700*	--
		Al	984±17				
		bare CGA	571±12				

Table II. Activation energies for three conduction paths (contact configurations)

Contacts	E_a (eV)
Au – Au	0.517
Al/Mg – Al/Mg	0.461
Au – Al/Mg	0.510

Table III. Estimates of contact properties for KPFM-measured Schottky barrier heights

T (K)	R_s (Ω)	Φ (eV)	$A^* = 100$ A/m ² K ²	$A^* = 500$ A/m ² K ²
			V_t (V)	V_t (V)
300	1.E+06	0.1	-0.650	-0.688
		0.6	-0.150	-0.188
250	1.E+08	0.1	-0.620	-0.652
		0.6	-0.120	-0.152
220	2.E+09	0.1	-0.588	-0.616
		0.6	-0.088	-0.116

Figure/Table Captions

Figure 1. Squares of Al/Mg contact metal ($58\ \mu\text{m} \times 58\ \mu\text{m}$, bar width $25\ \mu\text{m}$, thickness $\sim 70\ \text{nm}$) electron-beam deposited through a TEM grid on a bulk amorphous CGA substrate.

Figure 2. UPS data for Au and CGA material. The secondary edge fit is illustrated.

Figure 3. Band diagrams of metal/CGA (*a*) before and (*b*) after contact, based on UPS, XPS, KPFM, optical absorption spectroscopy data. Values are in eV.

Figure 4. (color online) Kelvin Probe Force Microscopy maps of contact potential difference (CPD) on the surface of (*a*) Au contact/CGA edge and (*b*) Al/Mg contact/CGA edge. The height data represent the topography of the surface while the color represents the CPD value. For the Au contact, the right-hand side has large CPD; for the Al/Mg contact, the left-hand side has large CPD. The white lines on the KPFM maps indicate the regions used for corresponding linescans across metal/CGA edge, shown in (*c*) and (*d*). Profiles shown are averages of approximately 30 neighboring linescans spaced at $0.1\ \mu\text{m}$. Linescans were measured perpendicular to the contact/CGA edge.

Figure 5. Conductivity vs. temperature plot for CGA sample in four point probe configuration. Activation energy E_a is calculated by fitting the curve to an exponential function.

Figure 6. Temperature dependent I-V curves for contact configuration Al/Mg-CGA-Au. I-V curves are linear and symmetrical. Curves were taken every 2 K; curves shown here are for every 10 K.

Table I. *Indirectly calculated value.

Table II.

Table III. Comparison of the reverse voltage (V_r) at which a Schottky barrier with the given parameters (A^* , barrier height Φ , T) provides the same resistance as the series resistance R_s for the CGA material itself.

References

- 1 L. Bai, N. Y. Garces, C. Xu, L. E. Halliburton, N. C. Giles, P. G. Schunemann, K. Nagashio, C. Yang, and R. S. Feigelson, in *Effect of donors and acceptors on the optical properties of CdGeAs₂*, San Jose, CA, USA, 2004 (SPIE), p. 22.
- 2 V. Rud, Y. Rud, I. Polushina, T. Ushakova, and S. Iida, "Observation of Record Hall Mobility in CdGeAs₂ Single Crystals," *Japanese Journal of Applied Physics* **39**, 266 (2000).
- 3 S. H. Risbud, "Processing and properties of some II-IV-V-2 amorphous and crystalline semiconductors," *Applied Physics A-Materials Science & Processing* **62**, 519 (1996).
- 4 U. Rau and H. W. Schock, "Electronic properties of Cu(In,Ga)Se₂ heterojunction solar cells - recent achievements, current understanding, and future challenges," *Applied Physics A-Materials Science & Processing* **69**, 131 (1999).
- 5 N. Dietz and F. L. Madarasz, "Chemical and biological sensors based on optically confined birefringent chalcopyrite heterostructures," *Materials Science and Engineering B-Solid State Materials for Advanced Technology* **97**, 182 (2003).
- 6 M. D. Pelusi, V. G. Ta'eed, L. B. Fu, E. Magi, M. R. E. Lamont, S. Madden, D. Y. Choi, D. A. P. Bulla, B. Luther-Davies, and B. J. Eggleton, "Applications of highly-nonlinear chalcogenide glass devices tailored for high-speed all-optical signal processing," *IEEE Journal of Selected Topics in Quantum Electronics* **14**, 529 (2008).
- 7 S. Sadewasser, "Surface potential of chalcopyrite films measured by KPFM," *Physica Status Solidi A-Applications and Materials Science* **203**, 2571 (2006).
- 8 C. Lian and H. L. Xing, "Surface potential measurements on Ni-(Al)GaN lateral Schottky junction using scanning Kelvin probe microscopy," *Applied Physics Letters* **88** (2006).
- 9 S. Sabuktagin, Y. T. Moon, S. Dogan, A. A. Baski, and H. Morkoc, "Observation of surface charging at the edge of a Schottky contact," *IEEE Electron Device Letters* **27**, 211 (2006).
- 10 E. Schlenker, V. Mertens, J. Parisi, R. Reineke-Koch, and M. Kontges, "Schottky contact analysis of photovoltaic chalcopyrite thin film absorbers," *Physics Letters A* **362**, 229 (2007).
- 11 H. B. Michaelson, "Work function of elements and its periodicity," *Journal of Applied Physics* **48**, 4729 (1977).
- 12 B. R. Johnson, B. J. Riley, S. K. Sundaram, J. V. Crum, C. H. Henager Jr., Y. Zhang, V. Shutthanandan, C. E. Seifert, R. M. Van Ginhoven, C. E. Chamberlin, A. A. Rockett, D. N. Hebert, and A. R. Aquino, "Synthesis and Characterization of Bulk, Vitreous Cadmium Germanium Arsenide," *Journal of the American Ceramic Society* **92**, 1236 (2009).
- 13 D. Briggs and J. C. Riviere, *Practical Surface Analysis*, Vol. 1, 2nd ed. (John Wiley and Sons, Chichester, England, 1983).
- 14 S. Hufner, *Photoelectron Spectroscopy Principles and Applications* (Springer, Heidelberg, 1995).
- 15 S. Lee, C. W. Liang, and L. W. Martin, "Synthesis, Control, and Characterization of Surface Properties of Cu₂O Nanostructures," *ACS Nano* **5**, 3736 (2011).
- 16 E. H. Rhoderick and R. H. Williams, *Metal-semiconductor contacts*, 2nd ed. (Clarendon Press; Oxford University Press, New York, 1988).
- 17 G. Neumann and G. M. Neumann, *Surface self-diffusion of metals* (Diffusion Information Center, Bay Village, Ohio, 1972).
- 18 B. G. Streetman, *Solid state electronic devices*, 4th ed. (Prentice Hall, Englewood Cliffs, N.J., 1995).
- 19 C. Xu, Thesis, West Virginia University, 2007.

- ²⁰ L. Kronik and Y. Shapira, "Surface photovoltage phenomena: theory, experiment, and applications," *Surface Science Reports* **37**, 1 (1999).
- ²¹ I. Ay and H. Tolunay, "The influence of ohmic back contacts on the properties of a-Si:H Schottky diodes," *Solid-State Electronics* **51**, 381 (2007).
- ²² E. L. Hull and R. H. Pehl, "Amorphous germanium contacts on germanium detectors," *Nuclear Instruments & Methods in Physics Research Section A - Accelerators Spectrometers Detectors and Associated Equipment* **538**, 651 (2005).